FELIPE RUGGERI

A TIME DOMAIN RANKINE PANEL METHOD FOR 2D SEAKEEPING ANALYSIS

Dissertação apresentada à Escola Politécnica da Universidade de São Paulo para obtenção do título de Mestre em Engenharia

São Paulo

2012

FELIPE RUGGERI

A TIME DOMAIN RANKINE PANEL METHOD FOR 2D SEAKEEPING

ANALYSIS

Dissertação apresentada à Escola Politécnica da Universidade de São Paulo para obtenção do título de Mestre em Engenharia

Área de Concentração:
Engenharia Naval e Oceânica

Orientador:
Prof. Dr. Alexandre Nicolaos Simos

São Paulo

2012

FICHA CATALOGRÁFICA

Resumo

A capacidade de prever os movimentos de uma plataforma de petróleo sujeita a ondas é bastante importante no contexto da engenharia naval e oceânica, já que esses movimentos terão diversas implicações no projeto deste sistema, com impactos diretos nos custos de produção e tempo de retorno do investimento. Esse trabalho apresenta os fundamentos teóricos sobre o problema de comportamento no mar de corpos flutuantes sujeitos a ondas de gravidades e um método numérico para solução do problema 2D no domínio do tempo. A hipótese básica adotada é a de escoamento potencial, que permitiu a utilização do método de elementos de contorno para descrever a região fluida. Optou-se pela utilização de fontes de Rankine como função de Green no desenvolvimento do método, o qual será abordado somente no contexto linear do problema matemático, delimitado através de um procedimento combinado entre expansão de Stokes e série de Taylor. As simulações são realizadas no domínio do tempo sendo, portanto, resolvido o problema de valor inicial com relação às equações do movimento e equações que descrevem a superfície-livre combinadas com dois problemas de valor de contorno, um para o potencial de velocidades e outro para o potencial de aceleração do escoamento. As equações integrais de contorno permitem transformar o sistema de equações diferenciais parciais da superfície livre num sistema de equações diferenciais ordinárias, a quais são resolvidas através do método de Runge-Kutta de $4^{\underline{a}}$ ordem. As equações integrais são tratadas de forma singularizada e o método utilizado para discretizar as mesmas é de ordem baixa tanto para a função potencial quanto para a aproximação geométrica, sendo as integrações necessárias realizadas numericamente através de quadratura Gauss-Legendre. O algoritmo numérico é testado e validado através de comparações com soluções analíticas, numéricas e experimentais presentes na literatura, considerando os problemas de geração de ondas, cálculo de massa adicional e amortecimento potencial através de ensaios de oscilação forçada, testes de decaimento e, por último, resposta em ondas. Os resultados obtiveram boa concordância com aqueles adotados como paradigma.

Palavras chave: Método de Rankine, Método de elementos de contorno, Comportamento em ondas.

Abstract

The ability to predict the seakeeping characteristics of an offshore structure (such as an oil platform) is very important in offshore engineering since these motions have important consequences regarding its design and therefore its cost and payback period. This work presents the theoretical and numerical aspects concerning the evaluation of the 2D seakeeping problem under the potential flow hypothesis, which allows the use a Boundary Elements Method to describe the fluid region with Rankine sources as Green function. The linearized version of the mathematical problem is built by a combined Stokes expansion and Taylor series procedure and solved in time domain.

The initial value problem concerning the motion and free surface equations are solved combined to the boundary value problems considering the velocity and acceleration flow potentials, which transform the partial differential equations of the free surface into ordinary differential equations, that are solved using the 4th order Runge-Kutta method. The integral equations are solved in it's singularized version using a low order method both for the potential function and the geometrical approximation, with the terms of the linear system evaluated using Gauss Legendre quadrature.

The numerical scheme is tested and validated considering analytical, numerical and experimental results obtained in the literature, concerning wave generation, added mass and potential damping evaluation, decay tests and response to waves. The results achieved good agreement with respect to those used as paradigm.

Keywords: Rankine panel method, Boundary Elements Method, Seakeeping.

List of Figures

List of Tables

Symbols

ρ - specific mass

$\vec{v}$ - flow velocity

φ - velocity potential

T - stress tensor

$\vec{b}$ - body forces

p - flow pressure

g - gravity acceleration intensity

S_{fixed} - surfaces concerning fixed (stationary) boundaries

$S_{pm}(t)$ - surfaces concerning prescribed motion boundaries

$S_{fb}(t)$ - surfaces concerning floating bodies boundaries

$S_{fs}(t)$ - free surface boundaries

$\vec{n}_Q(t)$ - normal vector at a point Q of the boundary

$\vec{v}_Q(t)$ - velocity vector at a point Q of the boundary

$\vec{v}_G(t)$ - translational velocity of the center of gravity of the body

$\vec{\omega}(t)$ - rotational velocity of the body

$G(t)$ - body center of mass point

$\eta(x, y, t)$ - free surface elevation for low steepness waves

$\vec{v}_s$ - velocity vector of the point s in the surface

$\vec{v}_p$ - velocity vector of a fluid particle p

m - body mass

$\vec{F}^{ext}$ - external forces vector applied to the body

$\vec{L}_O$ - angular moment vector of the body

$\vec{M}_O^{ext}$ - external moments concerning the pole O of the body

$\bar{\varphi}$ - zero order (time independent) velocity potential

$\varphi^{(i)}(t)$ - i^{th} order velocity potential

ϵ - perturbation factor (wave steepness)

$\eta^{(i)}(t)$ - i^{th} order elevation

$\bar{\bar{n}}$ - zero order (time independent) normal vector

$\vec{n}^{(i)}(t)$ - i^{th} order normal vector

$\vec{X}$ - linear body displacement

$\bar{\vec{X}}$ - zero order (time independent) linear body displacement

$\vec{X}^{(i)}(t)$ - i^{th} order linear body displacement

$\vec{\alpha}$ - angular body displacement

$\bar{\vec{\alpha}}$ - zero order (time independent) angular body displacement

$\vec{\alpha}^{(i)}(t)$ - i^{th} order angular body displacement

M - big positive real constant

$\Re^+$ - the positive real numbers

$\vec{V}^{(i)}(t)$ - i^{th} order linear body velocity vector

$\vec{\omega}^{(i)}(t)$ - i^{th} order angular body velocity vector

$S_{pm}(0)$ - mean prescribed motion body wetted surface

KC - Keulegan-Carpenter number

$p_D^{(i)}$ - i^{th} order dynamic pressure

$\bar{S}_{fb}$ - mean floating body wetted surface

ω - wave frequency

k - wavenumber

Φ - total velocity potential

φ - disturbed velocity potential

ϕ_I - incident wave velocity potential

$Re\{X\}$ - real part of X

ϕ_D - diffraction potential

ϕ_{Ri} - i^{th} degree of freedom radiation potential

$\vec{a}$ - flow acceleration

Ψ - acceleration potential

$\Psi^{(1)}$ - first order acceleration potential

$\vec{a}_Q$ - acceleration vector at a point Q of the boundary

$\vec{\theta}$ - rotation angle of the body

$\dot{\vec{\theta}}$ - rotational velocity of the body

$\ddot{\vec{\theta}}$ - rotational acceleration of the body

I_0 - body moment of inertia related to pole O

∇ (not the mathematical operator) - body displacement in volume

GM - metacentric height

G or $G(P, Q)$ - Green function

$\partial\Omega$ - fluid region boundaries

$\partial\Omega_\epsilon$ - boundary of a singular point of radius ϵ

Ω - fluid region

r_{PQ} - distance between points P and Q

r'_{PQ} - distance between points P and the image of Q about z=0 plane

(x_P, y_P, z_P) - field points coordinates

(x_Q, y_Q, z_Q) - source points coordinates

J_0 - Bessel function

$K(\vec{x}, \vec{s})$ - kernel function of Fredholm equation

s - parametric coordinate of the transformation

T_r - ramp period

Contents

Chapter 1

Introduction

1.1 Relevance and Motivation

In the context of offshore and naval design the correct seakeeping prediction is very important in all design phases, since response to waves (motions, velocities and accelerations) will define the environmental conditions in which the structure will operate safely. The latest discoveries of petroleum reservoir in the brazilian coast, in ultra-deep waters, mean that a greater demand for ships and platforms will appear in the next years, increasing the need for refined seakeeping studies. In facts better designs should help reducing the production downtime, specially under harsh conditions, improving production efficiency and reducing costs.

The technological development continuously improves the computational capability, allowing the use of sophisticated numerical methods for this problem. The problem to be studied consists of determining forces and motions on floating bodies under waves, current and wind with arbitrary incidences upon a floating structure that may or may not have forward speed. For platforms there are also interactions with the risers, mooring lines and tendons, most of them usually not considered in a first analysis.

An alternative approach is experimental, which is based on small-scale models that are tested on offshore basins, being able to reproduce some phenomena which are hard to evaluate numerically. The constrains involved in the experimental approach are related to the lack of similarity, specially Reynolds number and the accuracy on small parts and measurements (like the risers of an oil platform in deep waters). However, the experimental approach usually provides essential contributions on the validation/extension of numerical models.

A mixed approach based on numerical models combined with experimental data has been

developed at the Numerical Offshore Tank (TPN-USP) since 2000. One of the goals has been to provide a simulator that could handle a fully coupled solution of hydrodynamics, mooring lines, environmental conditions and body motions. Since the hydrodynamic solution is obtained in frequency domain using WAMIT (see Lee and Newman [2005] that summarize some of the developments performed), the time domain solution is evaluated following the theory developed by Cummins [1962], that basically transform the frequency domain solution into a time domain one using a convolution integral to take into account the flow memory effects. However, this procedure leads to some limitations, specially because the hydrodynamic problem in frequency domain can only be solved considering the first order and higher order solutions using Stokes series (see Stoker [1957]), which is only valid for weakly non-linear problems, as will be discussed later.

Following this approach the mesh is fixed during the whole simulation period, which leads to some limitations concerning some practical problems, like multi body simulation with large relative displacements. This problem, for example, motivated alternative strategies trying to overcome this limitation, like re-run the frequency domain code if the displacements exceeds a specified value, as presented by Tannuri et al. [2004] and Queiroz Filho and Tannuri [2009].

The only way to consider all the non-linearities concerning the problem is by solving the fully non-linear fluid-structure problem considering the time dependent boundaries and interactions, which is a long term goal for the simulator, specially for dealing with engineering applications where the "strong"[1] non-linear effects are important, such as multi body simulations with large relative displacements, extreme roll motions of FPSOs, structures with very low draft (such as monobuoys) and bodies in resonant motions. Shao [2010] states that strong non-linear effects are also important in the study of slamming, green water, capsizing of ships and violent sloshing.

Following this fully non-linear approach, almost all methods assumes a mixed Eulerian-Lagrangean (MEL) approach for the free surface evolution in time, which is not performed in the weakly non-linear formulation because the free surface remains in the undisturbed position. van Daalen [1993] formulated a fully non-linear time domain BEM for the evaluation of 2D wave-maker problem, forced oscillation test and decay tests. Greco [2001] followed a similar approach for the investigation of green water phenomenon, but added some additional effects like hydroelasticity. Tanizawa et al. [1999, 2000], Koo [2003], Koo and Kim [2004] and Kim and Koo [2005] applied the bidimensional fully non-linear approach for the evaluation of response to

---

[1]For strong non-linear effects we understand the ones that are beyond what the multi-scales approach can evaluate properly

waves of floating bodies in a numerical wave tank simulation (NWT). Tanizawa and Naito [1997] used the NWT for the study of parametric roll of a "bell" shaped body still in a 2D approach. Contento [2000] also studied the fully non-linear problem validating the results initially with Vugts [1968] experiments for forced oscillation and then performed decay tests and response to waves. The simulations concerning large initial displacements (40% of the draft) for heave free decay tests showed significant non-linear influence, which was not verified by van Daalen [1993] concerning a circular and rectangular sections, as will be presented latter. Tanizawa and Naito [1998] tried to reproduce chaos in roll motions still in a bidimensional approach.

Some other important problems concerning "weak" non-linearities are the slow motions (well discussed by Pinkster [1980]) and mean drift (introduced initially with a simple formula by Maruo [1960]) of offshore structures, that are already evaluated in the simulator using the first and second order solutions, both engineering problems discussed by Faltinsen [1990]. Those effects are taken into account although the slow motions evaluation require a long time to run when multi body and shallow water effects need to be considered for the QTF^2 evaluation. This long time computation is partially because the second order problem requires the free surface discretization, since the Green function adopted does not respect the second order inhomogeneous free surface condition. An alternative procedure would be the evaluation of a group of waves together in time domain, obtaining all the forces and motions during one single computation, following an approach similar to the proposed by Kim et al. [1997].

The weakly non linear approach was also adopted for the study of third order problems, concerning the presence and absence of current as presented in Shao [2010] (who also studied second order problems), that used a time domain higher order BEM for solving the mathematical problem, achieving good agreement for the results. Zhu [1997] formulated the third order diffraction problem, comparing a BEM solution to the long-wave approximation theory for the ringing^3 phenomenon. Stassen et al. [1998] described a BEM applied to the problem concerning the third-order free surface waves discussing that an additional condition must be imposed in order to correct the secular terms (see Nayfeh [1973]), that produced instabilities, as introduced by Benjamin and Feir [1967] for waves propagating without any kind of dissipation (or at least negligible in this order of approximation).

Although the main goal of the simulator is to evaluate the practical engineering problems discussed before, in the present work only basic steps involved in building an offshore seakeeping

---

^{2}Quadratic Transfer Function
^{3}High frequency transient type response

analysis code will be presented, in order to achieve a better comprehension of the physical phenomenon, mathematical modelling (and hypothesis), numerical issues and implementation procedure. In order to evaluate the method proposed a 2D code was implemented in Matlab® programming language. The output of the code is compared with some results presented in the literature to confirm the correctness of the mathematical model and numerical scheme presented, that latter will be extended to the desired practical problems. Furthermore, the main goal of this text is to present the basic aspects (which are not trivial) concerning the seakeeping problem for further extensions to the three dimensional problem.

The physical problem can be converted into a mathematical problem using appropriate hypothesis, simple conservation laws and boundary conditions concerning the nature of the fluid-structure interaction. The structures studied are fixed and floating bodies without forward speed susceptible only to gravity wave loads. Despite the formulation adopted provides an extension to multi-bodies interaction almost directly, this work is focused on a single floating body problem. The code was developed to allow simulations either in ocean conditions or in wave basins (modeling the wave-maker and the walls of a wave basin).

The conservation laws adopted for solving the flow are the mass and linear momentum conservation. The bodies are assumed as rigid and their motions can be described by Newton's law.

Regardless the body is free to move, the partial differential equation system describing the flow dynamics consists of four equations (three for momentum and one for mass), meaning that the velocity components in all directions and the pressure can be evaluated. The pressures are integrated over the wetted body surface, providing the hydrodynamic forces used for motion evaluation.

The ideal fluid model is usually adopted in the context of seakeeping analysis, which means that the fluid is homogeneous, has no viscosity and the flow is assumed as incompressible and potential, so the velocity field is irrotational, allowing the complete velocity field to be described by the value of a scalar function at the boundaries, being this function known as the velocity potential.

The assumption of potential flow is appropriate when the viscous effects can be neglected, which may occurs as the Reynolds number increases, since the inertial forces becomes large compared to viscous ones. For streamlined bodies this means that the flow separation will be small. For oscillating bodies, such as floating bodies on ocean waves, the relation of inertial

forces and viscous forces is given by the KC[4] number, which is usually small for oil platforms, specially in the linear problem context, when the problem is linear with the wave amplitude and the wave steepness is small.

The completely non-linear boundary value problem (BVP) for a floating body is very difficult to be solved, since the boundary conditions are mostly non-linear and applied to unknown time variant boundaries. In order to simplify the BVP, a Stokes expansion procedure is usually adopted, together with Taylor expansions, leading to a linear problem solved at the mean boundaries.

The BVP can be solved either in time domain or in frequency domain. The solution in frequency domain is based on separation of variables considering the motions as periodic, not allowing the analysis of transient effects, which can be done in time domain. Besides that, in frequency domain one usually does not solve the fluid/structure interaction directly, since the body motion equation is not solved coupled to the hydrodynamic BVP. Therefore, the body dynamic does not affect the hydrodynamic solution. In frequency domain usually the hydrodynamic solution is obtained considering 6 individual problems (one for each degree on freedom, the so called radiation problems) and the diffraction problem, the latter considering only the body presence, but not the body motion. On the other hand, the time domain approach requires the body dynamics to be solved coupled with the fluid BVP, solving the fluid/structure interaction directly, facilitating the inclusion of non-linearities, either in the hydrodynamic problem or in the body motion. However, it should be noticed that the time domain approach usually requires much more computational effort than the frequency domain, which was one of the reasons for the first numerical methods developed to be based in frequency domain solutions.

In this work, the numerical technique chosen to solve the BVP is the Boundary Elements Method (BEM), since the velocities can be defined in terms of the values at the boundaries, not being necessary to discretize the whole fluid domain, as would be the case in a Finite Elements Method (FEM), Finite Volumes Method (FVM) or Finite Differences Method (FDM). The computational effort required for solving a boundary elements method is usually much smaller than those required by these other methods, since only the boundaries are discretized, reducing the number of elements (and the size of the linear system).

In this work, only the linear problem will be considered in order to get the knowledge concerning the fundamental approach. Furthermore, the bidimensional linear approach presents

---

[4]Keulegan Carpenter

several relevant problems that can be solved analytically, which is very useful for validation purposes. So, this first work concerning a linear time domain boundary elements method should be understood as only the first step for further extensions, that in the future could consider the mooring dynamics and the completely non-linear problem.

The BEM requires the choice of a Green function and there are several ones, such as Kelvin sources and transient Green function. These functions satisfy the linearized free surface conditions automatically, reducing the computational effort, since the free surface does not need to be discretized. They could also be extended to satisfy the no flux condition at the flat bottom, if required, but then they have the inconvenient of containing an improper integral of difficult convergence. Besides that, these functions usually satisfy only the linearized free surface conditions and therefore they cannot be applied for non-linear problems, which is one of the long term goals. In the present work, the Rankine sources are chosen, which do not satisfy any boundary condition immediately, but their evaluation does not require much computational effort, rendering future extensions to non-linear problems easier.

The three major subdivisions in boundary elements method applied for naval and ocean applications are: advancing ships (problem with forward speed), platforms (floating stationary structures) and numerical wave tanks (NWT), the last one focusing on two main themes, non-linear free surface phenomena and fluid-structure interaction. Among the numerical codes based on Boundary Elements Methods available nowadays for seakeeping analysis, the main commercial softwares are WAMIT®, AQWA® and WADAM®, all adopting a frequency domain solution. Among the time domain softwares, which were mostly applied and developed for academic purposes, one may find TIMIT® and SWAN®.

The order of approximation of the geometry and the potential function leads to two kinds of numerical methods: the low order, that retains only the first term in the approximations, methods with plane panels and constant potential inside each panel, as introduced by Hess and Smith [1964] and the higher order method, that uses other representations containing more terms, that keep the continuity of the potential function and normal vector between the panels, and that can also be extended to guarantee the continuity of the derivatives of the potential function. One example of low order method is the singularized one developed by Yee-Tak Ng [1993] to study second order effects on floating structures. However, the use of higher order numerical methods are justified due to the reduction of computational effort, specially for solving the higher orders problems concerning seakeeping of stationary structures or problems concerning

forward speed, which require the evaluation of the panels tangential derivatives accurately. Some of the higher order codes developed are, for example, Maniar [1995] that extended the WAMIT code to a higher order panel method based on spline approximations for the potential function but the geometry could be arbitrary described. He also adopted a Galerkin procedure to obtain a determined linear system. Qiu [2001] and Qiu et al. [2006] presented the so-called panel free method (desingularized) for wave body interaction, with and without current, where the geometry is generically described by the coefficients of a NURBS, as largely available in CAD packages. Gao and Zou [2008], presented a desingularized higher order method based on NURBS for the geometry description and B-spline for the potential function to study problems concerning forward speed. Shao [2010] presented a higher method based in quadratic elements defined each 3 nodes, for both the potential function and geometry.

The following Table (1.1), taken from Bertram [1996] summarizes some of the numerical methods available for solving the forward speed problem. Here the "indirect method" stands for methods that evaluate the source strength, while the "direct method" indicate the ones that evaluate the velocity potential.

Table 1.1: Numerical methods for forward speed

No.	Place	Country	Code	Author	Method	Domain
1	MIT	USA	SWAN	Nakos, Sclavounous	Direct	Frequency
2	KRI/SNU	Korea	HOBEM	Hong, Choi	Direct	Frequency
3	Hiroshima	Japan	CBIEM	Iwashita et al.	Direct	Frequency
4	Osaka	Japan	-	Takagi	Indirect	Frequency
5	MHI	Japan	-	Yasukawa	Indirect	Frequency
6	Nantes	France	AQUAREVA	Maissonneuve et al	Indirect	Frequency
7	NTH	Norway	-	Zhao, Faltinsen	Indirect	Frequency
8	IfS	Germany	NEPTUN	Bertram	Indirect	Frequency
9	IfS	Germany	FREDDY	Bertram, Hughes	Indirect	Frequency
10	Michigan	USA	-	Cao et al.	Direct	Time
11	MIT	USA	SWAN	Kring, Sclavounos	Direct	Time
12	AMI	USA	USAERO/FSP	Maskew	Indirect	Time
13	Delft	Holland	-	Prins	Direct	Time

The numerical wave tank approach has also been researched by several groups, almost exclusively for academic purposes, creating even benchmark cases, whose contributors, taken from Tanizawa [2000] are shown in Table (1.2).

Table 1.2: List of contributors for NWT benchmark (Tanizawa [2000])

Contributor	Simulation Method
K. Tanizawa	BEM Fully Nonlinear
M. Kashiwagi	BEM Fully Nonlinear
H. Kihara	BEM Fully Nonlinear
A. H. Clement	BEM Fully Nonlinear
C. Maisondieu	BEM 2nd order
R. Otto & J. H. Westhuis	FEM Fully Nonlinear
N. Hirata	FVM Fully Nonlinear

It can be seen that most of the developments have been performed at the academic context. A better comprehension concerning the mathematical formulation and numerical methods in time domain for seakeeping analysis, which to the author's knowledge, was not complete developed in Brazil yet, is therefore one of the goals of the present study.

With this in mind, Chapter 2 states the complete mathematical problem stating the potential flow hypothesis and the free surface condition as described by a mathematical function, which does not allow overturning waves. A brief discussion about the complete non-linear problem is done, followed by a linearization procedure based on Stokes expansion.

Chapter 3 describes the mathematical procedure that allows the BVP concerning the flow problem to be described by means of an integral equation. A boundary elements method (BEM) for solving this problem is also defined, followed by a low order approximation description.

Chapter 4 describes the numerical method implemented, consisting on solving the Boundary Value Problem using a lower order panel method and the Initial Value Problem using a 4th order Runge-Kutta method (RK-4).

Chapter 5 shows the numerical results obtained for wave-generation at a numerical offshore tank, the added mass and wave damping coefficients estimated for simple geometric cylinders, the analysis of decay tests of the cylinders and the response amplitude operator for a bidimensional box. A small discussion concerning the comparison of the results with available data at the literature is also performed, showing that good agreement is achieved.

Finally, Chapter 6 brings the main conclusions about the linear method capability and the next steps required in order to extend the method for 3D cases. A discussion about possible improvements of the code and extensions for multi-bodies and non-linearities is also performed.

1.2 Bibliography review

The description of the fluid dynamics can be defined by a system of equations containing a scalar equation of mass conservation (continuity) and a vectorial equation concerning the linear momentum conservation (Navier-Stokes), that allow the evaluation of pressure and velocity field. These equations are largely available and discussed in Batchelor [2009], Milne-Thomson [1968] and Fox and Donald [1973]. The dynamic of a rigid body can be studied through the motion equations derived from Newton's laws.

The problem concerning floating bodies under gravity waves has been largely studied considering the potential flow description (Lamb [1945], Newman [1977] , Mei et al. [2005]), when the velocity field is assumed as irrotational, simplifying, for incompressible flows, the continuity equation into Laplace's equation. The ocean waves was largely studied for several authors, for example, by Stoker [1957] and Hermans [2011], that describe a multi-scale procedure for the decomposition of the non-linear free surface conditions into a sequence of several linear conditions, where the lower solutions are imposed into the higher order problems, as proposed by Stokes [1847].

The mathematical problem is quite difficult to be solved generically since it has non-linear conditions applied to time-varying boundaries (the free surface and the body wetted surface), as discussed, for example, by John [1949, 1950] and Kuznetsov et al. [2004]. In order to overcome this inconvenient several authors proposed simplified procedures, basically known as the linear approach, where the time varying boundaries are replaced by static ones and the boundary conditions are linearized during the calculations, achieving good experimental agreement for free surface flow without a floating body, as described by Barber and Ursell [1948] and Dean et al. [1959].

Hess and Smith [1964] introduced the use of a panel method for solving Laplace's equation using a singularized and indirect equation with a low order approximation either by the source strength distribution or geometrical approximation, obtaining good results considering bodies fully submerged. Dawson [1977] was one of the first to use Rankine sources as Green function for a panel method to evaluated three dimensional ship-resistance. Yang [2004] implemented a similar method for linear wave resistance calculation and formulated the fully non-linear approach concerning the wave resistance problem citing Tanizawa [1995] work, extending the formulation to consider forward speed effect. A discussion about the simulation stability in time is performed

by both and Tanizawa [2000] summarizes the four consistent methods available for the evaluation of the time derivative of the potential function, which is very important for time domain simulation stability, as will be presented latter: (1) Iterative method, as performed, for example, by Cao et al. [1994]; (2) Modal decomposition; (3) Indirect Method; (4) Implicit boundary condition method. Kacham [2004] evaluated this derivative by using a finite difference scheme. van Daalen [1993] followed the implicit boundary condition method, obtaining good agreement in the results.

The use of a numerical beach in order to avoid wave reflection was introduced by Israeli and Orszag [1981], which was followed by several authors concerning different numerical methods and problems. This idea was extended to the Rankine panel method considering damping term(s) in the free surface condition(s), for example, by Nakos et al. [1993], Kring [1994], Prins [1995], Cao et al. [1994], Huang [1997], Kim [2003], Koo and Kim [2004] and Zhen et al. [2010], although there are some variations.

Chapter 2

Mathematical problem

In this chapter the mathematical problem is formulated for the generic case of arbitrarily floating body motions on gravity waves. The difficulties involved for solving the complete problem are discussed and using a Stokes series approach the problem is simplified (linearized). After properly boundary conditions are defined, the Boundary Value Problem (BVP) is complete and linearized, the Initial Value Problem (IVP) is treated by defining the correct initial conditions.

2.1   Governing equations

As already mentioned, the basic hypothesis adopted are the incompressible and potential flow. The mass conservation is given by (2.1), where ρ is the specific mass and $\vec{v}$ is the velocity field. By definition, an incompressible flow has the material derivative of the specific mass as zero at all times, simplifying the mass conservation to equation (2.2).

$$\frac{D\rho}{Dt} + \rho \nabla \cdot \vec{v} = 0 \tag{2.1}$$

$$\rho \nabla \cdot \vec{v} = 0 \Rightarrow \nabla \cdot \vec{v} = 0 \tag{2.2}$$

Since the flow is assumed as potential the velocity field is written as (2.3), where φ denotes the velocity potential function, which is position and time dependent, converting the continuity equation to Laplace's equation (2.4), valid at the fluid region Ω.

$$\vec{v} = \nabla \varphi \tag{2.3}$$

$$\nabla \cdot \nabla \varphi = \nabla^2 \varphi = 0 \tag{2.4}$$

The conservation of linear momentum is expressed by equation (2.5) and represents Newton's second law applied to fluid particle. The acceleration is on the left side of the equation and all forces on the right side, where the contact forces are evaluated in terms of the stress tensor (T) and the field forces, such as gravity, by the body forces vector $\vec{b}$.

$$\frac{D\vec{v}}{Dt} = \frac{\partial \vec{v}}{\partial t} + \nabla \vec{v} \cdot \vec{v} = \frac{1}{\rho} \nabla \cdot T + \vec{b} \tag{2.5}$$

Looking more carefully into this equation we can se that it's only a statement of the balance between the acceleration of the fluid and the forces acting on it, which are segregated in two groups, one that acts directly on the fluid particle by contact and other that acts by distance.

Since the fluid is assumed ideal, the system is conservative because the unique external load considered is the gravity, which is also a conservative field. The stress tensor is given by (2.6), which allows the linear momentum conservation law to be written as (2.7), which is exactly Bernoulli's equation for an irrotational, non-permanent flow, where p is the pressure and g the gravity acceleration.

$$T_{ij} = -p\delta_{ij} \tag{2.6}$$

$$\frac{\partial \varphi}{\partial t} + \frac{1}{2} \|\nabla \varphi\|^2 + \frac{p}{\rho} + gz = C(t) \tag{2.7}$$

The initial 4 variables/4 equations problem is then reduced to the solution of 2 equations concerning 2 scalar functions (variables), the velocity potential function φ and the pressure p.

However, in order to particularize the solution, boundary conditions need to be provided. Those conditions guarantee the BVP an unique solution and the boundaries can be grouped in S_{fixed}, S_{pm}, S_{fb} and S_{fs}, denoting the fixed (stationary), prescribed motions, floating body and free surface boundaries, respectively.

The fixed boundaries are usually the sea bottom or the walls at a wave basin. The prescribed motion boundaries are the wetted surface of bodies with imposed motion, such as wave-makers or, as another example, bodies at oscillation test.

The conditions at all boundaries but the free surface are simply the no-flux condition, given by (2.8), (2.9) and (2.10). One should notice that velocity at the boundary can be described in terms of the velocities at the center of gravity of the body using Poisson formula, since the body is supposed rigid. These Neumann conditions are non-linear but at S_{fixed}, and are

quite complicated since the region of evaluation are time dependent, leading to a very complex condition. The non-linearities are due to the fluid-structure interaction nature, since different flows lead to different pressures and forces, changing body motions, wetted surface and the normal vector.

$$\frac{\partial \varphi_Q}{\partial n_Q} = 0, \quad for \quad Q \in S_{fixed} \tag{2.8}$$

$$\frac{\partial \varphi_Q}{\partial n_Q} = \vec{v}_Q(t) \cdot \vec{n}_Q(t), \quad for \quad Q \in S_{pm}(t) \tag{2.9}$$

$$\frac{\partial \varphi_Q}{\partial n_Q} = \vec{v}_Q(t) \cdot \vec{n}_Q(t) = \vec{n}_Q(t) \cdot [\vec{v}_G(t) + \vec{\omega}(t) \wedge (Q(t) - G(t))], \quad for \quad Q \in S_{fb}(t) \tag{2.10}$$

In the context of seakeeping analysis concerning potential flow, the free surface is usually understood as a membrane that segregates water from air at all time. This kind of construction denies the possibility of breaking waves, since the membrane is assumed as simply connected.

This approach simplifies the mathematical problem since the free surface can be described by a geometrical surface, where the boundary condition can be applied. The free surface elevation is measured from the undisturbed surface using a variable η and represents the z coordinate of the air-water interface, as can be seen on Figure (2.1). The basic idea is to find out a mathematical surface that can correctly capture the water-air interface, such as a membrane that always segregates the two phases, it is, no fluid particles can cross the membrane. Besides that, any motion of the particles in the surface normal direction deforms it, in order to keep the membrane always segregating the two phases.
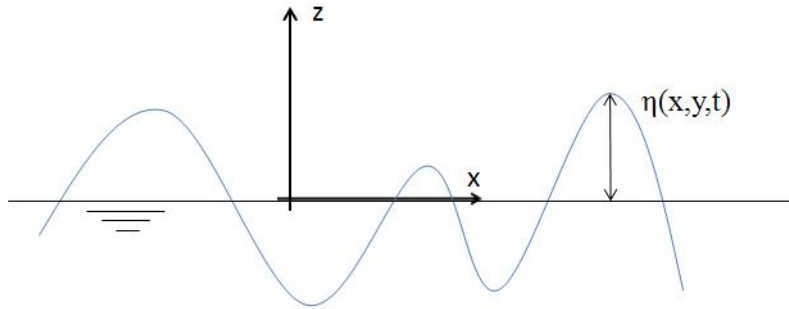
Figure 2.1: Free surface

Suppose a generic surface given by (2.11). It can be expanded using Taylor series as shown

29

in (2.12), where $\vec{v}_s$ is the surface velocity with components (v_x, v_y, v_z).

$$S(x, y, z, t) = 0, \forall t \tag{2.11}$$

$$S(\vec{x}+v_x\Delta t, y+v_y\Delta t, z+v_z\Delta t, t) = S(x, y, z, t)+\Big(\frac{\partial S}{\partial t}+\vec{v}_s\cdot\nabla S\Big)\Delta t+O(\Delta t^2)+O(\Delta t^3)+... \tag{2.12}$$

If we divide the expansion by Δt and take the limit case when Δt goes to zero, assuming all surface derivatives as finite, the equation (2.14) is obtained, since (2.11) is true at all times.

$$\lim_{\Delta t\to 0}\frac{S(x+v_x\Delta t, y+v_y\Delta t, z+v_z\Delta t, t)}{\Delta t} = \lim_{\Delta t\to 0}\left[\frac{S(x, y, z, t)}{\Delta t}+\frac{\Big(\frac{\partial S}{\partial t}+\vec{v}_s\cdot\nabla S\Big)}{\Delta t}\Delta t+O(\Delta t^2)+...\right] \tag{2.13}$$

$$\frac{\partial S}{\partial t}+\vec{v}_s\cdot\nabla S = 0 \tag{2.14}$$

Since the fluid has no viscosity, the basic relation of a generic fluid particle at the boundary is that the particle velocity vector projection on the free surface normal direction should be the same as the projection of the surface velocity vector at the surface normal direction, as given by (2.15), where $\vec{v}_p$ is the flow velocity at a point P adjacent to the surface S and $\vec{n}_s$ is the surface normal vector, which is equal to the surface gradient.

$$\vec{v}_p\cdot\vec{n}_s = \vec{v}_s\cdot\vec{n}_s \Rightarrow \vec{v}_p\cdot\nabla S = \vec{v}_s\cdot\nabla S, \quad P \in S \tag{2.15}$$

Applying (2.14) at the right side of (2.15) and changing the flow velocity by the gradient of the velocity potential function leads to (2.16).

$$\nabla\varphi_p\cdot\nabla S_p = -\frac{\partial S}{\partial t}\Big|_p, \quad \forall t, \quad P \in S \tag{2.16}$$

The free surface can be written as (2.17) and replacing it in equation (2.16) leads to condition (2.18).

$$S = z - \eta(x, y, t) = 0 \tag{2.17}$$

$$\frac{\partial \eta_p}{\partial t} = \nabla \varphi_p \cdot \nabla S_p, P \in S \Rightarrow \frac{\partial \eta}{\partial t} + \frac{\partial \varphi}{\partial x} \frac{\partial \eta}{\partial x} + \frac{\partial \varphi}{\partial y} \frac{\partial \eta}{\partial y} - \frac{\partial \varphi}{\partial z} = 0, \quad z = \eta(x, y, t) \qquad (2.18)$$

This condition is known as kinematic condition and states that particles at the free surface will be always at the free surface, because the velocity of the fluid particles adjacent to the membrane on the surface normal direction should be the same of the surface normal velocity of the membrane itself, which is assumed by construction, it is, the particles cannot "drop" from the surface.

The description of the free surface as (2.17) denies the possibility of overturning waves (waves that are almost breaking, see Figure (2.2)) because an elevation function η is assumed and it is single valued of the coordinates x and y.
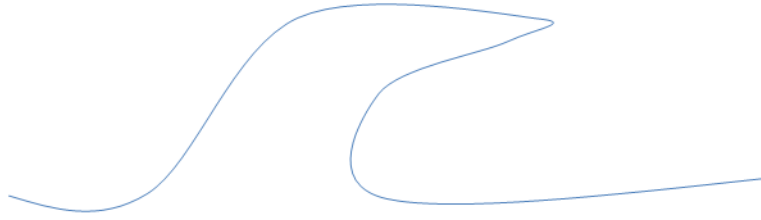
Figure 2.2: Example of overturning wave

The first expression in (2.18) states the Neumann condition for the free surface, but since η_t is unknown, the kinematic condition is not enough for determining the membrane behavior, specially because nothing was said about it's dynamics. Another condition needs to be specified then in order to evaluate the elevation itself, which is achieved by applying Bernoulli's equation (2.7).

Imposing that the pressure at the free surface should be atmospheric and choosing the constant $C(t)$ as zero, equation (2.19) is obtained. This statement is known as dynamic free surface condition and describes the equilibrium of forces at the air-water interface.

$$\frac{\partial \varphi}{\partial t} + \frac{1}{2}(\nabla \varphi \cdot \nabla \varphi) + g\eta = 0 \quad at \quad z = \eta(x, y, t) \qquad (2.19)$$

In the same way as already discussed for the prescribed motion and floating body boundaries, the free surface conditions are non-linear, being difficult to find an easy solution procedure. In the case of the free surface and the floating body, there is an additional problem because the

boundary conditions should be applied at an unknown time dependent surface. The floating body wetted surface, at all times, can only be defined by solving Newton's second law (2.20) and (2.21), assuming the body mass as constant and the only external loads as the gravity and flow pressure, where $\vec{L}_0$ is the angular moment considering a pole O and $\vec{M}_0^{ext}$ is the external torque considering the same pole.

$$\frac{d(m\vec{v}_G)}{dt} = \sum \vec{F}^{ext} \tag{2.20}$$

$$\frac{d\vec{L}_0}{dt} = \sum \vec{M}_O^{ext} \tag{2.21}$$

Therefore the boundary value problem (BVP) can be summarized in solving Laplace's equation (2.4) under the boundary conditions given by (2.18), (2.8), (2.9) and (2.10). The dynamic free surface condition (2.19) and body motions equations (2.20)/(2.21) would be used for the definition of the time dependent surface boundaries.

Since the problem containing non-linear boundary conditions applied at unknown boundaries are hard to solve directly, an initial simplified problem is solved, which is the linear problem, usually achieved by using expansions in Stokes series, as presented next.

2.2   Stokes expansion

The velocity potential, free surface elevation, normal vectors and moving bodies position vectors can be expanded using an unidimensional Stokes series, that is basically a multi-scales expansion using a perturbation factor ϵ, where the potential of order zero equals to zero because the problem has no forward speed and the position and normal vectors of order zero represent their mean values, it is, the vectors when the bodies are at rest. The $\vec{X}$ function in equation (2.25) and $\vec{\alpha}$ function in equation (2.26) denote the body linear and angular displacements. The method proposes the problem to be solved by splitting the original problem into a collection of linear problems (one for each order), solving them successively by imposing the solutions of the lower orders problem into the higher order ones.

$$\varphi = \bar{\varphi} + \sum_{i=1}^{\infty} \varphi^{(i)}(t).\epsilon^i \tag{2.22}$$

$$\eta = \sum_{i=0}^{\infty} \eta^{(i)}(t).\epsilon^i \tag{2.23}$$

$$\vec{n} = \bar{\bar{n}} + \sum_{i=1}^{\infty} \vec{n}^{(i)}(t).\epsilon^i \tag{2.24}$$

$$\vec{X} = \bar{\bar{X}} + \sum_{i=1}^{\infty} \vec{X}^{(i)}(t).\epsilon^i \tag{2.25}$$

$$\vec{\alpha} = \bar{\bar{\alpha}} + \sum_{i=1}^{\infty} \vec{\alpha}^{(i)}(t).\epsilon^i \tag{2.26}$$

The first condition for the series convergence is that all individual potentials φ_i to be finite, it is, they are bounded by a positive real M ($|\varphi_i| \leqslant M, M \in \mathcal{R}^+, i = 1, 2, 3, ..., \infty$) and the perturbation factor modulus to be less than 1 since this series is bounded by a geometrical series. This convergence condition is obviously extended to the remaining expansions.

$$\sum_{i=0}^{\infty} \varphi_i \epsilon^i \leqslant \sum_{i=0}^{\infty} M\epsilon^i = M \sum_{i=0}^{\infty} \epsilon^i \overset{|\epsilon|<1}{=} \frac{M}{1-\epsilon} \tag{2.27}$$

The velocity vector can be written by time derivation of (2.25) and (2.26), providing (2.28) and (2.29). As expected the mean velocities are zero, there is no zero order term.

$$\vec{V} = \sum_{i=1}^{\infty} \vec{V}^{(i)}(t).\epsilon^i \tag{2.28}$$

$$\vec{\omega} = \sum_{i=1}^{\infty} \vec{\omega}^{(i)}(t).\epsilon^i \tag{2.29}$$

The boundary condition at the floating bodies and prescribed motion surfaces can be written as (2.30).

$$\sum_{i=1}^{\infty} \epsilon^i \Big[\sum_{j=0}^{i} \nabla\varphi_Q^{(i-j)} \cdot \vec{n}_Q^{(j)} \Big] = \sum_{i=1}^{\infty} \epsilon^i \Big[\sum_{j=0}^{i} \vec{V}_Q^{(i-j)} \cdot \vec{n}_Q^{(j)} \Big], \quad at \quad Q \in S_{pm,fb}(t) \tag{2.30}$$

The standard procedure would be to multiply this expression by the powers of $(1/\epsilon)$ taking the limits when $\epsilon \to 0$ successively, which would lead to several boundary conditions, one for each order. However, it would not solve the inconvenient of having a time dependent boundary.

In order to overcome this inconvenient, the velocity vectors and the normal vectors are

expanded in Taylor series around the surface $S_{pm}(t=0) = \bar{S}_{pm}$. Supposing an arbitrary point (x_0, y_0, z_0) that belongs to the $S_{pm}(t=0)$, the expansion (2.31) can be performed.

$$V_x^{(i)}(x_0 + \Delta x, y_0 + \Delta y, z_0 + \Delta z, t) = V_x^{(i)}(x_0, y_0, z_0, t) + \left.\frac{\partial V_x^i}{\partial x}\right|_{(x_0,y_0,z_0)} \Delta x + \left.\frac{\partial V_x^i}{\partial y}\right|_{(x_0,y_0,z_0)} \Delta y +$$

$$\left.\frac{\partial V_x^i}{\partial z}\right|_{(x_0,y_0,z_0)} \Delta z + ... = \sum_{j=0}^{\infty} \sum_{k=0}^{\infty} \sum_{u=0}^{\infty} \frac{\Delta x^j \Delta y^k \Delta z^u}{j!k!u!} \left.\frac{\partial^{j+k+u} V_x^{(i)}}{\partial x^j \partial y^k \partial z^u}\right|_{(x_0,y_0,z_0)} \quad (2.31)$$

The values of $\Delta x, \Delta y$ and Δz are the (2.25) terms without the zero order value. Therefore all powers of the delta terms on Taylor expansion have at least order ϵ, but the zero power, which is exactly the value at rest. The other velocity and normal vector components could be expanded by an analogous process.

Replacing those expansions into (2.30), dividing by ϵ and now taking the limit for $\epsilon \to 0$ leads to (2.32), which is the first order condition.

$$\nabla \varphi_Q^{(1)} \cdot \vec{\bar{n}}_Q = \vec{V}_Q^{(1)} \cdot \vec{\bar{n}}_Q, \quad at \quad Q \in S_{pm}(0) \quad (2.32)$$

The procedure for the floating body boundary is exactly the same. For the deduction of a second order condition, the expression (2.30) should now divided by ϵ^2 (the terms of $(1/\epsilon)$ order would cancel each other since they respect the first order condition) followed by taking the limit for $\epsilon \to 0$. However, in this work the results are developed considering only the first order problem.

The next step is the linerization of the free surface boundary condition, which is done by replacing the velocity potential and free surface elevation series into the kinematic and dynamic conditions. The expressions (2.33) and (2.34) are then derived.

$$\frac{\partial}{\partial z}(\sum_{u=0}^{\infty} \varphi^{(u)} \epsilon^u) - \frac{\partial}{\partial t}(\sum_{u=0}^{\infty} \eta^{(u)} \epsilon^u) + \frac{\partial}{\partial x}(\sum_{u=0}^{\infty} \varphi^{(u)} \epsilon^u) \frac{\partial}{\partial x}(\sum_{u=0}^{\infty} \eta^{(u)} \epsilon^u) + \frac{\partial}{\partial y}(\sum_{u=0}^{\infty} \varphi^{(u)} \epsilon^u) \frac{\partial}{\partial y}(\sum_{u=0}^{\infty} \eta^{(u)} \epsilon^u) = 0$$

$$in \quad z = \sum_{u=0}^{\infty} \eta^{(u)} \epsilon^u \quad (2.33)$$

$$\rho \frac{\partial}{\partial t}(\sum_{u=0}^{\infty} \varphi^{(u)} \epsilon^u) + \frac{1}{2}\rho \nabla(\sum_{u=0}^{\infty} \varphi_u \epsilon^u) \cdot \nabla(\sum_{u=0}^{\infty} \varphi^{(u)} \epsilon^u) + \rho g(\sum_{u=0}^{\infty} \eta^{(u)} \epsilon^u) = 0 \quad in \quad z = \sum_{u=0}^{\infty} \eta^{(u)} \epsilon^u \quad (2.34)$$

After some algebra the expressions for an arbitrary order can be achieved and grouped as

can be seen in (2.35) and (2.36).

$$\sum_{i=0}^{\infty}\left\{\epsilon^i\Big[\frac{\partial\eta^{(i)}}{\partial t}-\frac{\partial\varphi^{(i)}}{\partial z}+\sum_{j=0}^{i}\Big(\frac{\partial\varphi^{(j)}}{\partial x}\frac{\partial\eta^{(i-j)}}{\partial x}+\frac{\partial\varphi^{(j)}}{\partial y}\frac{\partial\eta^{(i-j)}}{\partial y}\Big)\Big]\right\}=0\quad in\quad z=\sum_{u=0}^{\infty}\eta^{(u)}\epsilon^u\quad(2.35)$$

$$\sum_{i=0}^{\infty}\left\{\epsilon^i\Big[\frac{\partial\varphi^{(i)}}{\partial t}+\frac{1}{2}\sum_{j=0}^{i}(\nabla\varphi^{(j)}\cdot\nabla\varphi^{(i-j)})+g\eta^{(i)}\Big]\right\}=0\quad in\quad z=\sum_{u=0}^{\infty}\eta^{(u)}\epsilon^u\qquad(2.36)$$

Following the same procedure adopted before, all functions can be locally expanded by a Taylor series around the undisturbed free surface (z=0). Replacing the free surface by the stokes series (2.23) the expression (2.37) for the time derivative of the free surface elevation can be derived.

$$\frac{\partial\eta^{(i)}}{\partial t}\Big|_{z=\eta}=\frac{\partial\eta^{(i)}}{\partial t}\Big|_{z=0}+\sum_{j=1}^{\infty}\frac{\partial^{j+1}\eta^{(i)}}{\partial z^j\partial t}\Big|_{z=0}\frac{\eta^j}{j!}=\frac{\partial\eta^{(i)}}{\partial t}\Big|_{z=0}+\sum_{j=1}^{\infty}\frac{\partial^{j+1}\eta^{(i)}}{\partial z^j\partial t}\Big|_{z=0}\frac{(\sum_{i=0}^{\infty}\eta^{(i)}.\epsilon^i)^j}{j!}\quad(2.37)$$

Changing all terms in equations (2.35) and (2.36) by their respective Taylor series leads to the equations (2.39) and (2.38). Taking the limit $\epsilon\to0$ in expression (2.39) leads to the zero order elevation to be zero, as can be seen on (2.40).

$$\sum_{i=0}^{\infty}\Big[\epsilon^i\Big[\sum_{k=0}^{\infty}\Big(\frac{\partial^{k+1}\eta^{(i)}}{\partial z^k\partial t}\Big|_{z=0}\frac{(\sum_{v=0}^{\infty}\epsilon^v\eta^{(v)})^k}{k!}\Big)-\sum_{k=0}^{\infty}\Big(\frac{\partial^{k+1}\varphi^{(i)}}{\partial z^{k+1}}\Big|_{z=0}\frac{(\sum_{v=0}^{\infty}\epsilon^v\eta^{(v)})^k}{k!}\Big)$$
$$+\sum_{j=0}^{i}\Big(\sum_{k=0}^{\infty}\Big(\frac{\partial^{k+1}\varphi^{(j)}}{\partial z^k\partial x}\Big|_{z=0}\frac{(\sum_{v=0}^{\infty}\epsilon^v\eta^{(v)})^k}{k!}\Big)\sum_{k=0}^{\infty}\Big(\frac{\partial^{k+1}\eta^{(i-j)}}{\partial z^k\partial x}\Big|_{z=0}\frac{(\sum_{v=0}^{\infty}\epsilon^v\eta^{(v)})^k}{k!}\Big)+$$
$$\sum_{k=0}^{\infty}\Big(\frac{\partial^{k+1}\varphi^{(j)}}{\partial z^k\partial y}\Big|_{z=0}\frac{(\sum_{v=0}^{\infty}\epsilon^v\eta^{(v)})^k}{k!}\Big)\sum_{k=0}^{\infty}\Big(\frac{\partial^{k+1}\eta^{(i-j)}}{\partial z^k\partial y}\Big|_{z=0}\frac{(\sum_{v=0}^{\infty}\epsilon^v\eta^{(v)})^k}{k!}\Big)\Big)\Big]\Big]=0,\;in\;z=0$$

$$(2.38)$$

$$\sum_{i=0}^{\infty}\Big[\epsilon^i\Big[\sum_{k=0}^{\infty}\Big(\frac{\partial^{k+1}\varphi^{(i)}}{\partial z^k\partial t}\Big|_{z=0}\frac{(\sum_{v=0}^{\infty}\epsilon^v\eta^{(v)})^k}{k!}\Big)+$$
$$\frac{1}{2}\sum_{j=0}^{i}\Big[\sum_{k=0}^{\infty}\nabla\Big(\frac{\partial^k\varphi^{(j)}}{\partial z^k}\Big|_{z=0}\frac{(\sum_{v=0}^{\infty}\epsilon^v\eta^{(v)})^k}{k!}\Big)\cdot\sum_{k=0}^{\infty}\nabla\Big(\frac{\partial^k\varphi^{(i-j)}}{\partial z^z}\Big|_{z=0}\frac{(\sum_{v=0}^{\infty}\epsilon^v\eta^{(v)})^k}{k!}\Big)\Big]+$$
$$g\sum_{k=0}^{\infty}\frac{\partial^k\eta^{(i)}}{\partial z^k}\Big|_{z=0}\frac{(\sum_{v=0}^{\infty}\epsilon^v\eta^{(v)})^k}{k!}\Big]\Big]=0,\;in\;z=0\quad(2.39)$$

$$\lim_{\epsilon \to 0} \sum_{i=0}^{\infty} \Big[\epsilon^i \Big[\sum_{k=0}^{\infty} \Big(\frac{\partial^{k+1}\varphi^{(i)}}{\partial z^k \partial t}\Big|_{z=0} \frac{(\sum_{v=0}^{\infty} \epsilon^v \eta^{(v)})^k}{k!} \Big) +$$

$$\frac{1}{2} \sum_{j=0}^{i} \Big[\sum_{k=0}^{\infty} \nabla\Big(\frac{\partial^k \varphi^{(j)}}{\partial z^k}\Big|_{z=0} \frac{(\sum_{v=0}^{\infty} \epsilon^v \eta^{(v)})^k}{k!} \Big) \cdot \sum_{k=0}^{\infty} \nabla\Big(\frac{\partial^k \varphi^{(i-j)}}{\partial z^z}\Big|_{z=0} \frac{(\sum_{v=0}^{\infty} \epsilon^v \eta^{(v)})^k}{k!} \Big) \Big] +$$

$$g \sum_{k=0}^{\infty} \frac{\partial^k \eta^{(i)}}{\partial z^k}\Big|_{z=0} \frac{(\sum_{v=0}^{\infty} \epsilon^v \eta^{(v)})^k}{k!} \Big]\Big] = \sum_{k=0}^{\infty} \frac{\partial^k \eta^{(i)}}{\partial z^k}\Big|_{z=0} \frac{\eta^{(0)k}}{k!} = 0 \Rightarrow \eta^{(0)} = 0 \quad (2.40)$$

The next step is the division of expressions (2.39) and (2.38) by the perturbation factor ϵ and the evaluation of the limit when $\epsilon \to 0$, already considering the zero order elevation and potential as zero. Only the first term on Taylor series should be taken, since it is powered at zero while the other terms will contain powers equal or greater than 1 for the perturbation factor. Following this process the expressions (2.41) and (2.42) are obtained, which is the first order problem and supposing that it was solved, the first order elevation and potential at the free surface would be determined.

$$\lim_{\epsilon \to 0} \sum_{i=0}^{\infty} \Big[\epsilon^{i-1} \Big[\sum_{k=0}^{\infty} \Big(\frac{\partial^{k+1}\eta^{(i)}}{\partial z^k \partial t}\Big|_{z=0} \frac{(\sum_{v=0}^{\infty} \epsilon^v \eta^{(v)})^k}{k!} \Big) - \sum_{k=0}^{\infty} \Big(\frac{\partial^{k+1}\varphi^{(i)}}{\partial z^{k+1}}\Big|_{z=0} \frac{(\sum_{v=0}^{\infty} \epsilon^v \eta^{(v)})^k}{k!} \Big)$$

$$+ \sum_{j=0}^{i} \Big(\sum_{k=0}^{\infty} \Big(\frac{\partial^{k+1}\varphi^{(j)}}{\partial z^k \partial x}\Big|_{z=0} \frac{(\sum_{v=0}^{\infty} \epsilon^v \eta^{(v)})^k}{k!} \Big) \sum_{k=0}^{\infty} \Big(\frac{\partial^{k+1}\eta^{(i-j)}}{\partial z^k \partial x}\Big|_{z=0} \frac{(\sum_{v=0}^{\infty} \epsilon^v \eta^{(v)})^k}{k!} \Big) +$$

$$\sum_{k=0}^{\infty} \Big(\frac{\partial^{k+1}\varphi_j}{\partial z^k \partial y}\Big|_{z=0} \frac{(\sum_{v=0}^{\infty} \epsilon^v \eta^{(v)})^k}{k!} \Big) \sum_{k=0}^{\infty} \Big(\frac{\partial^{k+1}\eta^{(i-j)}}{\partial z^k \partial y}\Big|_{z=0} \frac{(\sum_{v=0}^{\infty} \epsilon^v \eta^{(v)})^k}{k!} \Big) \Big)\Big]\Big] =$$

$$\lim_{\epsilon \to 0} \frac{\partial \eta^{(1)}}{\partial t} - \frac{\partial \varphi^{(1)}}{\partial z} = 0$$

$$\frac{\partial \eta^{(1)}}{\partial t} = \frac{\partial \varphi^{(1)}}{\partial z}, \quad in \quad z = 0 \quad (2.41)$$

$$\lim_{\epsilon \to 0} \sum_{i=0}^{\infty} \Big[\epsilon^{i-1} \Big[\sum_{k=0}^{\infty} \Big(\frac{\partial^{k+1}\varphi^{(i)}}{\partial z^k \partial t}\Big|_{z=0} \frac{(\sum_{v=0}^{\infty} \epsilon^v \eta^{(v)})^k}{k!} \Big) +$$

$$\frac{1}{2} \sum_{j=0}^{i} \Big[\sum_{k=0}^{\infty} \nabla\Big(\frac{\partial^k \varphi^{(j)}}{\partial z^k}\Big|_{z=0} \frac{(\sum_{v=0}^{\infty} \epsilon^v \eta^{(v)})^k}{k!} \Big) \cdot \sum_{k=0}^{\infty} \nabla\Big(\frac{\partial^k \varphi^{(i-j)}}{\partial z^z}\Big|_{z=0} \frac{(\sum_{v=0}^{\infty} \epsilon^v \eta^{(v)})^k}{k!} \Big) \Big] +$$

$$g \sum_{k=0}^{\infty} \frac{\partial^k \eta^{(i)}}{\partial z^k}\Big|_{z=0} \frac{(\sum_{v=0}^{\infty} \epsilon^v \eta^{(v)})^k}{k!} \Big]\Big] = \lim_{\epsilon \to 0} g\eta^{(1)} + \frac{\partial \varphi^{(1)}}{\partial t} = 0$$

$$\eta^{(1)} = -\frac{1}{g} \frac{\partial \varphi^{(1)}}{\partial t}, \quad in \quad z = 0 \quad (2.42)$$

Taking the expression (2.39) and (2.38), dividing by ϵ^2 and evaluating again the limit when $\epsilon \to 0$ leads to the so-called second order condition as can be seen in (2.43) and (2.44), getting new inhomogeneous linear equations where the second order elevation and potential are evaluated imposing the first order solutions.

$$\lim_{\epsilon \to 0} \sum_{i=0}^{\infty} \Big[\epsilon^{i-2} \Big[\sum_{k=0}^{\infty} \Big(\frac{\partial^{k+1}\eta^{(i)}}{\partial z^k \partial t}\Big|_{z=0} \frac{(\sum_{v=0}^{\infty} \epsilon^v \eta^{(v)})^k}{k!} \Big) - \sum_{k=0}^{\infty} \Big(\frac{\partial^{k+1}\varphi^{(i)}}{\partial z^{k+1}}\Big|_{z=0} \frac{(\sum_{v=0}^{\infty} \epsilon^v \eta^{(v)})^k}{k!} \Big)$$

$$+ \sum_{j=0}^{i} \Big(\sum_{k=0}^{\infty} \Big(\frac{\partial^{k+1}\varphi^{(j)}}{\partial z^k \partial x}\Big|_{z=0} \frac{(\sum_{v=0}^{\infty} \epsilon^v \eta^{(v)})^k}{k!} \Big) \sum_{k=0}^{\infty} \Big(\frac{\partial^{k+1}\eta^{(i-j)}}{\partial z^k \partial x}\Big|_{z=0} \frac{(\sum_{v=0}^{\infty} \epsilon^v \eta^{(v)})^k}{k!} \Big) +$$

$$\sum_{k=0}^{\infty} \Big(\frac{\partial^{k+1}\varphi^{(j)}}{\partial z^k \partial y}\Big|_{z=0} \frac{(\sum_{v=0}^{\infty} \epsilon^v \eta^{(v)})^k}{k!} \Big) \sum_{k=0}^{\infty} \Big(\frac{\partial^{k+1}\eta^{(i-j)}}{\partial z^k \partial y}\Big|_{z=0} \frac{(\sum_{v=0}^{\infty} \epsilon^v \eta^{(v)})^k}{k!} \Big) \Big) \Big] \Big] =$$

$$\lim_{\epsilon \to 0} \Big[\frac{1}{\epsilon} \Big(\frac{\partial \eta^{(1)}}{\partial t} - \frac{\partial \varphi^{(1)}}{\partial z} \Big) + \frac{\partial \eta^{(2)}}{\partial t} - \frac{\partial \varphi^{(2)}}{\partial z} + \frac{\partial \varphi^{(1)}}{\partial x}\frac{\partial \eta^{(1)}}{\partial x} + \frac{\partial \varphi^{(1)}}{\partial y}\frac{\partial \eta^{(1)}}{\partial y} - \frac{\partial^2 \varphi^{(1)}}{\partial z^2}\eta^{(1)} \Big] = 0$$

$$\frac{\partial \eta^{(2)}}{\partial t} - \frac{\partial \varphi^{(2)}}{\partial z} + \frac{\partial \varphi^{(1)}}{\partial x}\frac{\partial \eta^{(1)}}{\partial x} + \frac{\partial \varphi^{(1)}}{\partial y}\frac{\partial \eta^{(1)}}{\partial y} - \frac{\partial^2 \varphi^{(1)}}{\partial z^2}\eta^{(1)} = 0, \quad in \quad z = 0 \quad (2.43)$$

$$\lim_{\epsilon \to 0} \sum_{i=0}^{\infty} \Big[\epsilon^{i-2} \Big[\sum_{k=0}^{\infty} \Big(\frac{\partial^{k+1}\varphi^{(i)}}{\partial z^k \partial t}\Big|_{z=0} \frac{(\sum_{v=0}^{\infty} \epsilon^v \eta^{(v)})^k}{k!} \Big) +$$

$$\frac{1}{2} \sum_{j=0}^{i} \Big[\sum_{k=0}^{\infty} \nabla\Big(\frac{\partial^k \varphi^{(j)}}{\partial z^k}\Big|_{z=0} \frac{(\sum_{v=0}^{\infty} \epsilon^v \eta^{(v)})^k}{k!} \Big) \cdot \sum_{k=0}^{\infty} \nabla\Big(\frac{\partial^k \varphi^{(i-j)}}{\partial z^z}\Big|_{z=0} \frac{(\sum_{v=0}^{\infty} \epsilon^v \eta^{(v)})^k}{k!} \Big) \Big] +$$

$$g \sum_{k=0}^{\infty} \frac{\partial^k \eta^{(i)}}{\partial z^k}\Big|_{z=0} \frac{(\sum_{v=0}^{\infty} \epsilon^v \eta^{(v)})^k}{k!} \Big] \Big] = \lim_{\epsilon \to 0} \Big[\frac{1}{\epsilon}\Big(g\eta^{(1)} + \frac{\partial \varphi^{(1)}}{\partial t} \Big) +$$

$$\frac{\partial \varphi^{(2)}}{\partial t} + g\eta^{(2)} + \frac{1}{2}\nabla\varphi^{(1)} \cdot \nabla\varphi^{(1)} + \frac{\partial^2 \varphi^{(1)}}{\partial z \partial t}\eta^{(1)} \Big] =$$

$$\frac{\partial \varphi^{(2)}}{\partial t} + g\eta^{(2)} + \frac{1}{2}\nabla\varphi^{(1)} \cdot \nabla\varphi^{(1)} + \frac{\partial^2 \varphi^{(1)}}{\partial z \partial t}\eta^{(1)} = 0, \quad in \quad z = 0 \quad (2.44)$$

As discussed before this procedure can continue for higher orders and the important result is the decomposition of the non-linear condition into several linear problems, recovering the original non-linear equation if there is a small perturbation factor that goes to zero and a solvability condition. However, it should be noticed that the higher orders problems (more than the three) are hard to be verified experimentally and the effects concerning those problems could be as small as the viscous effects, which were neglected since the beginning of the formulation.

In the linear problem the free-surface boundary conditions are given by (2.46) and (2.47), where η and φ are the first order potentials, being the subscripts neglected in order to simplify

the notation.

This perturbation factor ϵ is actually kA, the wave steepness where k is the wave number, and in order to guarantee the wave stability this factor should be small. The Keulegan-Carpenter number (KC) (2.45) measures the inertial forces over drag forces for bluff objects at oscillatory motions, where V is the velocity amplitude, T is the period of oscillation and L is a characteristic length, which can be simplified at gravity waves situation to the wave amplitude over a characteristic length. If this value is small, it is, the wave amplitude is small compared to the body characteristic length, the inertial forces dominate. In the seakeeping context of oil platforms (focus of this work), this condition is usually satisfied, which means that most of the acting forces are inertial. The approximation assuming potential flow for the hydrodynamic forces is also as good as the flow near the body can be assumed as potential. Near the body it is well known that there is a boundary layer, where the viscous and turbulent effects are significantly appreciable. If this layer is thin and there is not much separation, the pressure at the body surface can be approximated by the potential pressure near the surface and outside the boundary layer. This condition is satisfied if the body has an hydrodynamic shape, it is, the surface curvature radius is large, which is clearly not the case at edges and corners. For oil platforms motion prediction this local effect can under some circumstances be neglected, it is, if the wave steepness and body motions are small, since this local contributions on forces are small compared to the flow global effects. This condition is usually not completely satisfied near the resonance frequency, since even small waves lead to big displacements. Besides that, in order to guarantee accurate results, the ratio wave amplitude per body draft should be reasonable, since the problem is solved considering the wetted mean surface (wetted surface at rest), not taking into account the instantaneous wetted surface.

$$KC = \frac{VT}{L} = \frac{A\omega\frac{2\pi}{\omega}}{L} = \frac{2\pi A}{L} \tag{2.45}$$

$$\frac{\partial \eta}{\partial t} = \frac{\partial \varphi}{\partial z} \quad in \quad z = 0 \tag{2.46}$$

$$\eta = -\frac{1}{g}\frac{\partial \varphi}{\partial t} \quad in \quad z = 0 \tag{2.47}$$

The linear free-surface equations can be combined into a single condition (2.48), which is

known as the Cauchy-Poisson condition.

$$\frac{\partial^2 \varphi}{\partial t^2} + g\frac{\partial \varphi}{\partial z} = 0 \quad in \quad z = 0 \tag{2.48}$$

The motions equation are also solved, so the pressure at the body (2.49) and (2.50) needs to be linearized. The pressure evaluation is transferred from the instantaneous wetted surface to the mean wetted surface using again Taylor expansion.

$$p = \sum_{i=0}^{\infty} p^{(i)} \epsilon^i \tag{2.49}$$

$$p = -\rho\frac{\partial}{\partial t}\Big(\sum_{i=1}^{\infty} \varphi^{(i)}\epsilon^i\Big) - \frac{1}{2}\rho\nabla\Big(\sum_{i=1}^{\infty} \varphi^{(i)}\epsilon^i\Big) \cdot \nabla\Big(\sum_{i=1}^{\infty} \varphi^{(i)}\epsilon^i\Big) - \rho g z, at S_{fb}(t) \tag{2.50}$$

$$p = -\rho\sum_{i=1}^{\infty} \epsilon^i\Big(\frac{\partial\varphi^{(i)}}{\partial t} + \frac{1}{2}\sum_{j=0}^{i} \nabla\varphi^{(i-j)} \cdot \nabla\varphi^{(j)}\Big) + \rho g z, at \quad S_{fb}(t) \tag{2.51}$$

The linearized flow pressure is given by (2.52), with the hydrostatic term neglected because the forces are evaluated at the mean wetted surface, which is the body position at rest, assuming buoyancy equilibrium (which is a zero order quantity), it is balanced by the body weight. The body weight and buoyancy equilibrium can be changed in motion equations by considering constant hydrostatic restoration terms involving, in first order, the mean water plane area and static moments.

$$p_D^{(1)} = -\rho\frac{\partial\varphi^{(1)}}{\partial t}, \quad at \quad S_{fb}(0) = \bar{S}_{fb} \tag{2.52}$$

The body motion equations are presented on (2.53), (2.54) and (2.55) for the bidimensional case, the case of interest in this work, where L_{WL} is the area of water plane (actually it is a length in the bidimensional case), m is the body mass, I_0 is the moment of inertia concerning the center of flotation (actually a moment of inertia per length) with the normal vector assumed as pointing inward the body. The normal vector mean value (time independent) is denoted by the index 0 in order to better comprehend the order of the forces evaluated.

$$m\ddot{z}_G^{(1)} + \rho g L_{WL} z_G^{(1)} = \int_{\bar{S}_{fb}} p_D^{(1)} n_z^{(0)} dl \tag{2.53}$$

$$m\ddot{x}_G^{(1)} = \int_{\bar{S}_{fb}} p_D^{(1)} n_x^{(0)} dl \tag{2.54}$$

$$I_0\ddot{\theta}^{(1)} + \rho g \nabla GM\theta^{(1)} = \int_{\bar{S}_{fb}} p_D^{(1)} [n_{zQ}^{(0)}(x_Q^{(0)} - x_G^{(0)}) - n_{xQ}^{(0)} z_Q^{(0)}] dl \tag{2.55}$$

For the evaluation of the Neumann conditions at the floating bodies boundary, the velocities can be described in terms of the center of gravity, as shown in (2.56).

$$\frac{\partial \varphi^{(1)}}{\partial n^{(0)}}\Big|_Q = \vec{V}_Q^{(1)}(t) \cdot \vec{n}_Q^{(0)} = n_{zQ}^{(0)}[\dot{z}_G^{(1)}(t) + \dot{\theta}^{(1)}(t).(x_Q^{(0)} - x_G^{(0)})] + n_{xQ}^{(0)}[\dot{x}_G^{(1)}(t) - \dot{\theta}^{(1)}(t).(z_Q^{(0)} - z_G^{(0)})] \tag{2.56}$$

The equations and conditions presented so far are enough to guarantee an unique solution to the boundary value problem. The initial conditions for the initial value problem closure are discussed ahead, in section 2.4. From now on the development will be performed only for the interest case, which is the bidimensional one.

The theory developed above can be applied for numerical wave tanks, but for oceanic conditions, an incident wave potential must be included. Supposing the incident wave potential given by (2.57) the boundary conditions at S_{fixed}, $\bar{S}_{pm}$ and $\bar{S}_{fb}$ change to (2.59) imposing the impermeability under the assumption of the superposition effects, as shown on (2.58). Here φ will denote the perturbation caused by the body on the undisturbed flow field represented by ϕ_I. The incident wave potential already respects the linearized free surface conditions.

$$\phi_I = \frac{Ag}{\omega} e^{kz} \cos(kx - \omega t), \quad |x| < \infty, \quad z \leqslant 0 \tag{2.57}$$

$$\Phi = \varphi + \phi_I \tag{2.58}$$

$$\frac{\partial \Phi^{(1)}}{\partial n^{(0)}}\Big|_Q = 0 \Rightarrow \frac{\partial \varphi^{(1)}}{\partial n^{(0)}}\Big|_Q = \vec{V}_Q^{(1)}(t) \cdot \vec{n}_Q^{(0)} - \frac{\partial \phi_I}{\partial n^{(0)}} \tag{2.59}$$

Some differences between the time domain and frequency domain approaches should be discussed before the mathematical problem development continues.

2.3 A discussion between time domain and frequency domain approaches

In frequency domain the separation of variables technique (2.60) and the superposition principle are used (2.61), decomposing the total potential into a diffraction potential ϕ_D, 3 radiation potentials ϕ_{Ri} (2D case, one for each degree of freedom) and an incident wave potential ϕ_I.

$$\Phi(x, z, t) = Re\{\hat{\Phi}(x, z)e^{i\omega t}\} \tag{2.60}$$

$$\Phi = \phi_D + \sum_{i=1}^{3} \phi_{Ri} + \phi_I \tag{2.61}$$

The boundary condition at the floating body is given by (2.62) that may be decomposed into the conditions (2.63) and (2.64), which combined to Laplace's equation, the other boundary conditions and an appropriate radiation condition at infinity lead to the so called diffraction and radiation problems, which may be solved individually. The radiation condition appears from the separation of variables, that leads to a non-unique solution, requesting an additional condition defining the correct direction of energy propagation for diffracted and radiated waves.

$$\frac{\partial \Phi}{\partial n} = \vec{V}_Q \cdot \vec{n}_Q \Rightarrow \frac{\partial \phi_D}{\partial n}\Big|_Q + \frac{\partial \phi_I}{\partial n}\Big|_Q + \sum_{i=1}^{3} \frac{\partial \phi_{Ri}}{\partial n}\Big|_Q = V_{xG}n_{xQ} + V_{zG}n_{zQ} + \dot{\theta}[n_{zQ}(x_Q - x_G) - n_{xQ}(z_Q - z_G)] \tag{2.62}$$

$$\frac{\partial \phi_D}{\partial n}\Big|_Q = -\frac{\partial \phi_I}{\partial n}\Big|_Q \tag{2.63}$$

$$\frac{\partial \phi_{R1}}{\partial n}\Big|_Q = V_{xG}n_{xQ}; \quad \frac{\partial \phi_{R2}}{\partial n}\Big|_Q = V_{zG}n_{zQ}; \quad \frac{\partial \phi_{R3}}{\partial n}\Big|_Q = \dot{\theta}[n_{zQ}(x_Q - x_G) - n_{xQ}(z_Q - z_G)]; \tag{2.64}$$

More importantly, one should observe that in frequency domain the original boundary value problem is decomposed into several independent problems, the transient effects cannot be evaluated directly due to the previous assumption of harmonic variation in time (2.60) and in the linear approach the body dynamics does not need to be solved coupled to the hydrodynamics, so the body motions are only post-processed results. Despite being much faster in terms of calculation effort, since there is only 4 integral equations to be solved (one for the diffraction problem

and three for the radiation problems), this approach turns difficult to add non-linearities to the BVP or considering multi-bodies problems, when the relative position change significantly during the timespan of the analysis.

On the other hand, time domain approach naturally deals with transient effects and must solve the coupled fluid-body problem. It makes the inclusion of geometrical and hydrodynamic non-linearities easier, but requires much more computational capability, since there will be two BVP (one for the velocity potential and another for the acceleration one, the last presented next) and five ordinary differential equations for IVP (two for the free surface equations and three for body motions). An important aspect that should be remarked is that due to the coupled body dynamics and hydrodynamics, the numerical scheme needs to be robust, in order to avoid numerical instabilities. The main issue during the time evolution is the evaluation of the time derivative of the velocity potential function, used for the body forces evaluation, since it is difficult to provide an accurate and stable numerical scheme because the velocity potential is evaluated explicitly. In order to overcome this inconvenient, the acceleration potential is introduced into the numerical scheme, leading to a new BVP, that solved provides the time derivative directly, as presented next.

2.3.1 Acceleration potential

The essence of the fluid-structure interaction for a free floating body is quite different from the one when the motion is prescribed, because in the latter the position does not depend on the hydrodynamic pressure, which is proportional to the time derivative of the potential function. For a free floating body this dependence exists and any inaccurate evaluation may turn the solution unstable and, after some time, the simulation diverges.

In the context of potential flow the velocity field is assumed irrotational, which allows the determination of a potential function for the flow velocity, representing a conservative field, being the velocity completely defined by the values of this function at the boundaries. The same procedure may be proposed for the flow acceleration:

$$\vec{a} = \nabla \Psi \tag{2.65}$$

It is possible to establish an equation between the acceleration potential and the velocity potential, as shown in (2.66). This equation is non-linear with a difficult convective term, but

using Stokes expansion, it can be demonstrated that this term can be neglected in the first order problem, since the zero order velocity potential is null, leading to (2.68).

$$\vec{a} = \frac{\partial \vec{v}}{\partial t} + \nabla \vec{v} \cdot \vec{v} = \frac{\partial (\nabla \varphi)}{\partial t} + \nabla (\nabla \varphi) \cdot \nabla \varphi = \nabla \left(\frac{\partial \varphi}{\partial t} + \frac{1}{2} \nabla \varphi \cdot \nabla \varphi \right) = \nabla \Psi \tag{2.66}$$

$$\Psi = \frac{\partial \varphi}{\partial t} + \frac{1}{2} \nabla \varphi \cdot \nabla \varphi \tag{2.67}$$

$$\Psi^{(1)} = \frac{\partial \varphi^{(1)}}{\partial t} \tag{2.68}$$

The linearized acceleration potential also satisfies Laplace's equation (2.69) (one should notice that the complete acceleration potential (2.67) does not satisfies Laplace's equation due to the non-linear term). The boundary conditions can be defined by derivation of the first order velocity potential BVP boundary conditions, as can be seen in (2.70). The acceleration potential conditions are given by (2.71) and (2.72) for fixed and prescribed motion boundaries, where the subscripts are neglected in order to simplify the notation. It should be noted the time derivative of the normal vector in (2.70) is zero because in the linear approach only the normal vector zero order term (time independent) is considered.

$$\nabla^2 \left(\frac{\partial \varphi}{\partial t} \right) = 0, \quad in \quad \Omega \tag{2.69}$$

$$\frac{\partial}{\partial t} \left(\frac{\partial \varphi}{\partial n} \right) = \frac{\partial}{\partial t} (\nabla \varphi) \cdot \vec{n} + \nabla \varphi \cdot \frac{\partial \vec{n}}{\partial t} = \frac{\partial \vec{v}}{\partial t} \cdot \vec{n} = \vec{a}(t) \cdot \vec{n} \tag{2.70}$$

$$\frac{\partial}{\partial t} \left(\frac{\partial \varphi}{\partial n} \right) \Big|_Q = - \frac{\partial}{\partial t} \left(\frac{\partial \phi_I}{\partial n} \right) \Big|_Q, \quad Q \in S_{fixed} \tag{2.71}$$

$$\frac{\partial}{\partial t} \left(\frac{\partial \varphi}{\partial n} \right) \Big|_Q = \vec{a}_Q(t) \cdot \vec{n}_Q - \frac{\partial}{\partial t} \left(\frac{\partial \phi_I}{\partial n} \right) \Big|_Q, \quad Q \in \bar{S}_{pm} \tag{2.72}$$

At the floating body boundary, the acceleration can be described in terms of the center of gravity acceleration (2.73). The stokes expansion for this condition leads to (2.74), neglecting the centripetal acceleration term, since it is, at least, of order ϵ^2.

$$\vec{a}_Q = \frac{\partial \vec{v}_Q}{\partial t} = \vec{a}_G + \ddot{\vec{\theta}} \wedge (Q - G) + \dot{\vec{\theta}} \wedge [\dot{\vec{\theta}} \wedge (Q - G)] \tag{2.73}$$

$$\frac{\partial}{\partial t}\left(\frac{\partial \varphi}{\partial n}\right)\Big|_Q = n_{zQ}[\ddot{z}_G(t) + \ddot{\theta}(t).(x_Q - x_G)] + n_{xQ}[\ddot{x}_G(t) - \ddot{\theta}(t).(z_Q - z_G)] - \frac{\partial}{\partial t}\left(\frac{\partial \phi_I}{\partial n}\right)\Big|_Q, \quad Q \in \bar{S}_{fb} \tag{2.74}$$

The acceleration of the center of gravity can be described in terms of the equations of motion (2.54), (2.53) and (2.55), which then result dependent of the acceleration potential as shown in (2.75), with v as a dummy variable concerning the body wetted surface. By following this procedure the body acceleration can be eliminated from the integral equation and the acceleration potential remains as the only variable.

$$\vec{a}_Q \cdot \vec{n}_Q = \rho n_{xQ} \oint_v (\frac{\partial \varphi_v}{\partial t}) \left\{ \frac{n_{xv}}{m} - \frac{(z_Q - z_G)[n_{zv}(x_v - x_G) - n_{xv}z_v]}{I_0} \right\} dl_v +$$

$$n_{xQ} \left[\frac{\rho g \nabla GM \, (z_Q - z_G)}{I_0}\theta \right] -$$

$$\rho n_{zQ} \oint_v (\frac{\partial \varphi_v}{\partial t}) \left\{ \frac{n_{zv}}{m} - \frac{(x_Q - x_G)[n_{zv}(x_v - x_G) - n_{xv}z_v]}{I_0} \right\} dl_v +$$

$$n_{zQ} \left[-\frac{\rho g L_{WL}}{m}z_G - \frac{\rho g \nabla GM \, (x_Q - x_G)}{I_0}\theta \right] \tag{2.75}$$

The first order boundary condition at the free surface is given by (2.76), where η is evaluated through the dynamic free surface condition.

$$\eta_Q = -\frac{1}{g}\frac{\partial \varphi_Q}{\partial t} \Rightarrow \frac{\partial \varphi_Q}{\partial t} = -g\eta_Q, \quad z = 0 \tag{2.76}$$

The BVP for the acceleration potential is then complete. The solution provides the time derivative of the potential function, which may then be used for the body forces evaluation. Since the problem is solved on time domain, initial conditions concerning the initial value problem should be provided, as discussed next.

2.4   Initial conditions

The initial conditions concerning the floating body are basically the initial velocity and position to be nulls, since the body is assumed at rest initially, the undisturbed free surface $\eta(\vec{x}, 0) = 0$

and the velocities and acceleration as zero at the prescribed motion boundaries.

At the floating bodies, prescribed motion and fixed surfaces the variable to be evaluated in the BVP is the potential function, because the Neumman conditions are known (for the fixed and prescribed motion surfaces) or can be evaluated (for the floating bodies using the equations of motion) at all time. However, for the free surface neither the potential nor the flux are known, which means that both could be chosen as variable to be evaluated in the BVP. In this work the choice was the imposition of a Dirichlet condition (the potential function) at the free surface and the evaluation of the flux, in order to convert the free surface partial differential equations into ordinary differential equations.

The free surface Dirichlet condition can be derived from the mass conservation condition on the interior region translated into flux conservation by Gauss theorem (2.77).

$$\int_{\Omega} \nabla^2 \varphi d\Omega = \oint_{\partial \Omega} \frac{\partial \varphi}{\partial n} d\partial \Omega = \int_{S_{fixed}} \frac{\partial \varphi}{\partial n} dS + \int_{S_{pm}} \frac{\partial \varphi}{\partial n} dS + \int_{S_{fb}} \frac{\partial \varphi}{\partial n} dS + \int_{S_{fs}} \frac{\partial \varphi}{\partial n} dS = 0 \quad \forall t \geqslant 0$$

(2.77)

The flux through the free surface is zero and replacing the linearized free surface condition into the zero flux condition and since the surfaces are fixed in time, the condition (2.78) can be derived.

$$\int_{S_{fs}} \left(\frac{\partial \varphi}{\partial n} \right)_{t=0} dS = \int_{S_{fs}} \left(\frac{\partial \varphi}{\partial z} \right)_{t=0} dS = -\frac{1}{g} \int_{S_{fs}} \left(\frac{\partial^2 \varphi}{\partial t^2} \right)_{t=0} dS = -\frac{1}{g} \frac{\partial^2}{\partial t^2} \int_{S_{fs}} \varphi(x, z, 0) dS = 0$$

(2.78)

The simplest function that satisfies this condition is the null function and it was assumed for the whole free surface ($\varphi(x, z, 0)$=0). The BVP and IVP are now complete. The next chapter will discuss the numerical procedure adopted for solving the BVP.

Chapter 3

Boundary Elements Method (BEM)

In this chapter a brief discussion on boundary elements method is done in order to discuss the benefits from the potential flow hypothesis. The discussion about the adoption of Rankine sources as the Green function for the numerical model is performed and after that, the velocity and acceleration potential BVPs are translated into integral equations, which may then be solved by the numerical scheme described in Chapter 4.

3.1   Green's second identity

As it was discussed before, the assumption of potential flow allows the velocity field to be completely described by the boundaries values of a potential function. Under this assumption the solution of flow dynamics is based on BVPs governed by Laplace's equation.

However, this equation must be satisfied in the entire fluid region, which is not convenient in terms of a numerical solution because then the whole volume domain should be discretized and the velocity field does not depend of the interior domain values directly. The basic idea of a boundary elements method is to relate the interior values of the function with the boundary values and this can be done by making use of Green's second identity (3.1), so the interior values can be related to the function values and flux at the boundaries.
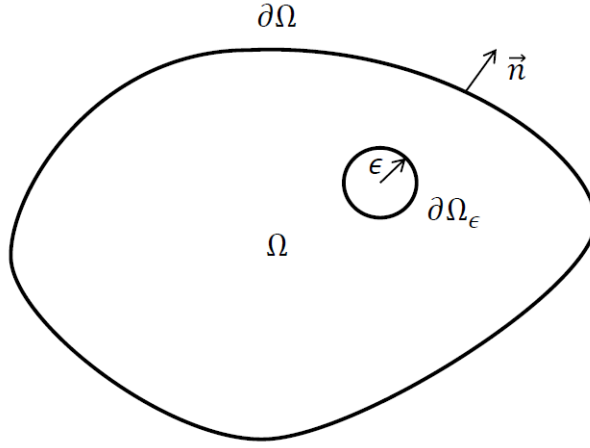
Figure 3.1: Representation of Ω, $\partial\Omega$, $\partial\Omega_\epsilon$ and ϵ

$$\iiint\limits_{\Omega} (G\Delta\varphi - \varphi\Delta G)d\Omega = \iint\limits_{\partial\Omega}(G\frac{\partial\varphi}{\partial n} - \varphi\frac{\partial G}{\partial n})d\partial\Omega \qquad (3.1)$$

The region Ω is assumed to be singly connected and bounded by piecewise smooth surfaces $\partial\Omega$, as shown in Figure (3.1), with the normal vector pointing outward concerning an observer inside the fluid domain. The potential function φ and the Green's function G are assumed harmonic and C^2-continuous, which means that both satisfy Laplace's equation ($\nabla^2\varphi = \nabla^2 G = 0$) in Ω, but for a finite number of points where the functions may not be defined.

It is possible to isolate the points where the functions are not defined (being $\vec{x}$ the vector pointing from the origin of the coordinate system to those points) by using a small sphere of radius ϵ and surface $\partial\Omega_\epsilon$ centered at $\vec{x}$, if those points are placed in the interior of Ω. If those points are at the boundary $\partial\Omega$, half a sphere is used, taking advantage of the smooth piecewise boundary, meaning that half a sphere can always isolate those points. For a more generic surface that is not smooth, such as a corner, a spherical cap defined by the solid angle, it is, the interior space angle, should be taken.

Now that all precautions were taken and there are two surfaces bounding the points where the function is not defined, Green's identity can be applied to the region between those surfaces if the point is inside Ω or at the region $\Omega\backslash\Omega_\epsilon$ if the point is at the boundaries, leading to (3.2). The fact that the potential function and Green's function are harmonic can be used to cancel the left side of the equality, obtaining (3.3).

$$\iiint\limits_{\Omega} (G\Delta\varphi - \varphi\Delta G)d\Omega = \iint\limits_{\partial\Omega+\partial\Omega_\epsilon} (G\frac{\partial\varphi}{\partial n} - \varphi\frac{\partial G}{\partial n})d\partial\Omega \qquad (3.2)$$

47

$$\iint\limits_{\partial\Omega}(G\frac{\partial\varphi}{\partial n} - \varphi\frac{\partial G}{\partial n})d\partial\Omega = -\iint\limits_{\partial\Omega_\epsilon}(G\frac{\partial\varphi}{\partial n} - \varphi\frac{\partial G}{\partial n})d\partial\Omega \qquad (3.3)$$

The next step is to evaluate the right side of (3.3). Since the radius can be as small as desired and so may be the surface $\partial\Omega_\epsilon$, one may take the limit $\epsilon \to 0$ (3.4). Before proceeding, however, the function G needs to be defined.

$$\lim_{\epsilon\to 0}\iint\limits_{\partial\Omega_\epsilon}(G\frac{\partial\varphi}{\partial n} - \varphi\frac{\partial G}{\partial n})d\partial\Omega \qquad (3.4)$$

3.2 Rankine sources

The choice of the most appropriate Green's function is particular to each boundary problem, the convenience to the numerical method and approach adopted. In the context of seakeeping problems there are some famous ones, such as the transient Green function, Kelvin sources and Rankine sources, this last one being adopted in this work.

The transient Green function for deep water is given by (3.5), where r and r' are given by (3.6) and (3.7), K is the wave number, J_0 is the Bessel function, Q is the point where the singularity is placed and P the evaluation point. This singularity is usually adopted in the frequency domain approach automatically satisfies the linear free surface and radiation conditions, which means that the free surface does not need to be discretized. However, this Green's function has the inconvenient of involving a improper integral containing a Bessel function in the integrand, which requires some computational effort to guarantee its numerical convergence. Furthermore, it only satisfies the linearized free surface condition and so non-linearities cannot be included easily.

$$G(P,Q) = \frac{1}{r} + \frac{1}{r'} + \frac{2K}{\pi}\int_0^\infty dk\frac{e^{k(z_P+z_Q)}}{k-K}J_0(kR) \qquad (3.5)$$

$$r = \sqrt{(x_P - x_Q)^2 + (y_P - y_Q)^2 + (z_P - z_Q)^2} \qquad (3.6)$$

$$r' = \sqrt{(x_P - x_Q)^2 + (y_P - y_Q)^2 + (z_P + z_Q)^2} \qquad (3.7)$$

Despite the Rankine sources do not satisfy any boundary condition automatically (like the free surface or a plane bottom) it is simple to evaluate and appropriate for future works con-

cerning non-linear calculations, justifying it's first use in this work. This Green's function is given by (3.8), where c_0 is an arbitrary constant (the source strength).

$$G(P, Q) = \frac{c_0}{r_{PQ}} \tag{3.8}$$

$$r_{PQ} = \sqrt{(x_P - x_Q)^2 + (y_P - y_Q)^2 + (z_P - z_Q)^2} \tag{3.9}$$

This expression should be replaced into Green's identity and, as discussed before, the precautions should be taken because Rankine source is singular at $r_{PQ} = 0$, leading to an indetermination problem for interior or boundary points.

After choosing the Green function (3.8) the limiting process (3.4) can be continued, but for convenience a spherical coordinate system will be used, where $(\theta : 0 \leqslant \theta \leqslant 2\pi)$ is the azimuth angle, $(\psi : 0 \leqslant \psi \leqslant \pi)$ is the polar angle and r is the radial distance. The jacobian for a spherical coordinate system is $r^2 \sin(\psi)$ and assuming the function φ_Q as finite, the first part of the limit can be evaluated as (3.10), which is independent of the angle ψ^*.

$$\lim_{\epsilon \to 0} \iint_{\partial\Omega_\epsilon} G \frac{\partial\varphi}{\partial n} d\partial\Omega = \lim_{\epsilon \to 0} \int_0^{\psi^*} \int_0^{2\pi} \left[\frac{c_0}{r} \frac{\partial\varphi_Q}{\partial n_Q} r^2 \sin(\psi) \right]_{r=\epsilon} d\theta d\psi =$$

$$\lim_{\epsilon \to 0} \int_0^{\psi^*} \int_0^{2\pi} \left[c_0 r \frac{\partial\varphi_Q}{\partial n_Q} \sin(\psi) \right]_{r=\epsilon} d\theta d\psi = \lim_{\epsilon \to 0} 2\pi[-\cos(\psi)]_0^{\psi^*} \epsilon = 0 \tag{3.10}$$

For the evaluation of the second part of the limit, the gradient operator in spherical coordinates is given by (3.11) and the term $\frac{\partial G}{\partial n}$ becomes (3.12), with the normal vector pointing outward the fluid region.

The limiting process is taken in (3.13).

$$\nabla \cdot = \left(\frac{\partial}{\partial r} \vec{e}_r + \frac{1}{r} \frac{\partial}{\partial \theta} \vec{e}_\theta + \frac{1}{r \sin(\theta)} \frac{\partial}{\partial \psi} \vec{e}_\psi \right) \cdot \tag{3.11}$$

$$\frac{\partial G}{\partial n} = \nabla G \cdot \vec{n} = \frac{\partial}{\partial r} \left(\frac{c_0}{r} \right) \vec{e}_r \cdot (-\vec{e}_r) = \frac{c_0}{r^2} \tag{3.12}$$

$$\lim_{\epsilon \to 0} \iint_{\partial\Omega_\epsilon} \varphi \frac{\partial G}{\partial n} d\partial\Omega = \lim_{\epsilon \to 0} \int_0^{\psi^*} \int_0^{2\pi} \left[\varphi_Q \frac{c_0}{r^2} r^2 \sin(\psi) \right]_{r=\epsilon} d\theta d\psi =$$

$$\lim_{\epsilon \to 0} \int_0^{\psi^*} \int_0^{2\pi} \varphi_Q c_0 \sin(\psi) d\theta d\psi = 2\pi \varphi_Q c_0 [-\cos(\psi)]_0^{\psi^*} \tag{3.13}$$

As discussed before, if the point is interior to Ω then $\psi^* = \pi$. Otherwise, if the point is at the boundary $\partial\Omega$ and the surface is smooth, $\psi^* = \pi/2$.

This leads to the results in (3.14), where the integration region does not contain the point P, since the residues were already evaluated and is shown in the right side of the expression. (For the boundary values it was considered only smooth surfaces). The constant c_0 is assumed as unit since it is arbitrary anyway.

$$\iint\limits_{\partial\Omega_{-P}} \left(\varphi_Q \frac{\partial G_{PQ}}{\partial n_Q} - G_{PQ}\frac{\partial \varphi_Q}{\partial n_Q}\right) d\partial\Omega_Q = \begin{cases} -4\pi\varphi_P, & if \quad P \quad is \quad inside \quad \Omega \\ -2\pi\varphi_P, & if \quad P \quad is \quad at \quad \partial\Omega \\ 0, & if \quad P \quad is \quad outside \quad \Omega \end{cases} \tag{3.14}$$

For the bidimensional problem, focus of this work, the Rankine source should be replaced by (3.15) and the integral equation to be solved is reduced to (3.17).

$$G(P,Q) = c_0 ln(r_{PQ}) \tag{3.15}$$

$$r_{PQ} = \sqrt{(x_P - x_Q)^2 + (z_P - z_Q)^2} \tag{3.16}$$

$$\int_{\partial\Omega_{-P}} \left[\varphi_Q \frac{\partial G_{PQ}}{\partial n_Q} - G_{PQ}\frac{\partial \varphi_Q}{\partial n_Q}\right] d\partial\Omega_Q = \begin{cases} 2\pi\varphi_P, & if \quad P \quad is \quad inside \quad \Omega \\ \pi\varphi_P, & if \quad P \quad is \quad at \quad \partial\Omega \\ 0, & if \quad P \quad is \quad outside \quad \Omega \end{cases} \tag{3.17}$$

The Rankine sources are also one of the fundamental solutions of Laplace's equation in polar coordinates. For instance, consider Laplace's equation in polar coordinates (3.18). If it is assumed that $\varphi = \varphi(r)$, the equation is easily simplified into the ordinary differential equation (3.19) with the basic solution given generically by (3.20); more details can be seen on Ang [2007].

$$\frac{1}{r}\frac{\partial}{\partial r}\left(r\frac{\partial \varphi}{\partial r}\right) + \frac{1}{r^2}\frac{\partial^2 \varphi}{\partial \theta^2} = 0 \tag{3.18}$$

$$\frac{d}{dr}\left(r\frac{d\varphi}{dr}\right) = 0 \tag{3.19}$$

$$\varphi = C_1 \ln(r) + C_2, \quad r \neq 0 \tag{3.20}$$

3.3 Fredholm integral equation

The equation (3.17) is part of a group of equations known as integral equations, characterized by the integrand function (or part of it) as the variable of the problem, in this case, the potential function $\varphi(\vec{x}, t)$. Equation (3.17), either choosing points at the boundaries or inside the domain for evaluation is a Fredholm inhomogeneous equation of the second kind (generally represented by (3.21)) because the limits of the integral operator are fixed (Fredholm), the function $\varphi(\vec{x}, t)$ appears inside and outside the integral (second kind) and there is another function $f(\vec{x})$ outside the integral sign (inhomogeneous). The function $K(\vec{x}, \vec{s})$ is known as the kernel function and due to the nature of the Green's function adopted (Rankine sources) the kernels obtained are symmetric, it is, satisfies (3.23).

$$\varphi(\vec{x}, t) = f(\vec{x}, t) + \int_S K(\vec{x}, \vec{s})\varphi(\vec{s}, t)d\vec{s} \tag{3.21}$$

$$f(\vec{x}, t) = \int_S K(\vec{x}, \vec{s})\varphi(\vec{s}, t)d\vec{s} \tag{3.22}$$

$$K(\vec{x}, \vec{s}) = K(\vec{s}, \vec{x}) \tag{3.23}$$

This classification is important because if the points chosen to evaluate the equation are outside the domain Ω, the equation to be solved would be a first kind Fredholm equation. However, even if the points are chosen inside the domain or at the boundaries, we can still have a first kind equation because at the free surface both the potential and the flux are unknown and if the choice is by the flux as a variable, a first kind equation is obtained.

In this work, the points will be chosen only at the boundaries because it is convenient for the numerical method that will be applied, as will become clear in Chapter 4. The potential as variable to be found for all boundaries but for the free surface, where the variable will be chosen the flux. This will lead to a mixed second and first kind equation.

It is possible to demonstrate that the set of linear algebraic equations (3.24) when $n \to \infty$, with $\delta x_j = \sqrt{(x_j - x_{j+1})^2 + (z_j - z_{j+1})^2}$, applied for points in the equation domain ($\partial\Omega$) is

exactly the solution of the integral equation. This is an important fact, because it allows changing the integral equation by a set of linear algebraic equations with infinite degrees of freedom, which is reduced by finite approximation adopting the collocation method. This is the procedure adopted in this work.

The collocation method approximates the equation domain by splitting the boundary $\partial\Omega$ in small line segments (elements) and the term $K(\vec{x}_i, \vec{x}_j)\varphi(\vec{x}_j, t)$ has a different value inside each one. The function $\varphi(\vec{x}, t)$ (unknown a priori and the one that we are looking for an approximation) and the domain surface are expanded in Taylor series and the order of approximation defines the accuracy of the method for a given number of elements.

$$\varphi(\vec{x}_i, t) = f(\vec{x}_i, t) + \sum_{j=0}^{n} K(\vec{x}_i, \vec{x}_j)\varphi(\vec{x}_j, t)\delta x_j, \quad i = 1, 2, ..., n \tag{3.24}$$

This simple description of integral equations are sufficient for the purpose of this work, but more details can found on Tricomi [1985], Moiseiwitsch [2005] and Rahman [2007].

Looking carefully into the boundary value problem and considering the flux at all boundaries as known, the boundary problem is reduced to the classic Neumman problem, which has an unique solution, but for a constant, if the total flux is zero. This constant is unknown and cannot be defined easily.

3.3.1 Numerical solution procedure

In this work the collocation method was adopted because other methods, such as Neummann approximations, which is iterative, would be very costly because for each order of approximation the integral equation needs to be evaluated at all points of the grid.

The integral equation to be solved is (3.25), which can be replaced by (3.26), suppressing the potential time dependence in order to simplify the notation, with P as an arbitrary point at the boundary and P_j the segments of the closed curve that composes the boundary.

$$-\pi\varphi(\vec{x}_P, t) + \oint_{Q \neq P} \varphi(\vec{x}_Q, t)\frac{\partial ln(r_{PQ})}{\partial n_Q}d\partial\Omega_Q - \oint_{Q \neq P} \frac{\partial\varphi(\vec{x}_Q, t)}{\partial n_Q}ln(r_{PQ})d\partial\Omega_Q = 0, \quad P \in \partial\Omega \tag{3.25}$$

$$\lim_{N\to\infty} -\pi\varphi_P + \sum_{j=0}^{N}\left(\int_{\substack{P_j \\ Q\neq P \\ ifP\in P_j}} \varphi_Q\frac{\partial ln(r_{PQ})}{\partial n_Q}dl_j - \int_{\substack{P_j \\ Q\neq P \\ ifP\in P_j}} \frac{\partial\varphi_Q}{\partial n_Q}ln(r_{PQ})dl_j\right) = 0, \; P \in \partial\Omega, \; \sum_{j=0}^{N} P_j = \partial\Omega$$

$$\tag{3.26}$$

Let's consider the existence of a parametrization (3.27) that takes the points of a line segment to the domain boundaries, which is a closed curve and cannot intersect itself. It allows the definition of an inverse transformation since $\gamma(s_1) = \gamma(s_2)$ only if $s_1 = a$ and $s_2 = b$.

$$\gamma(s) = \{(x(s), z(s)) | \forall\ a \leqslant t \leqslant b, \partial\Omega \equiv\ \gamma\} \tag{3.27}$$

In equation (3.26), the domain geometry and the logarithmic function are known but the potential function φ is not. However, the potential function can be expressed locally by a spatial Taylor series (3.28), where $\varphi(x, z, t) = \varphi(x(s), z(s), t) = \varphi(s, t)$ and, in order to simplify the notation, will be referred only as $\varphi(s)$.

$$\varphi(s) = \sum_{j=0}^{\infty} \varphi^{(j)}(s_0) \frac{(s - s_0)^j}{j!} \tag{3.28}$$

φ is replaced by the Taylor series in the second term of (3.26), assuming a convenient point s_0 inside each segment of the curve (this can be, for example, the center point of the element). The expression (3.29) is then derived, where the s_{0j} correspondent point is inside each segment of the curve bounded by the points $(x(s_{1j}), z(s_{1j}))$ and $(x(s_{2j}), z(s_{2j}))$, $j = 0, 1, 2, ..., N$.

$$\sum_{j=0}^{N} \int_{\substack{P_j \\ Q \neq P \\ if P \in P_j}} \varphi_Q \frac{\partial ln(r_{PQ})}{\partial n_Q} dl_j = \sum_{j=0}^{\infty} \sum_{k=0}^{\infty} \varphi^{(k)}(s_{0j}) \int_{s_{1j}}^{s_{2j}} \frac{(s - s_{0j})^k}{k!} \frac{\partial ln(r(s))}{\partial n(s)} \left\| \gamma'(s) \right\| ds \tag{3.29}$$

As discussed before, the imposition of a Dirichlet condition in some parts of the boundaries requires the flux at those parts to become variables of the problem. The flux can also be expanded locally by a Taylor series, as shown in (3.30) and replaced in the third term of (3.26), thus obtaining (3.31).

$$\frac{\partial \varphi}{\partial n}(s) = \sum_{j=0}^{\infty} \frac{d^j}{ds^j} \left(\frac{\partial \varphi}{\partial n} \right)_{s_0} \frac{(s - s_0)^j}{j!} \tag{3.30}$$

$$\sum_{j=0}^{N} \int_{\substack{P_j \\ Q \neq P \\ if P \in P_j}} \frac{\partial \varphi_Q}{\partial n_Q} ln(r_{PQ}) dl_j = \sum_{j=0}^{\infty} \sum_{k=0}^{\infty} \frac{d^k}{ds^k} \left(\frac{\partial \varphi}{\partial n} \right)_{s_0} \int_{s_{1j}}^{s_{2j}} \frac{(s - s_{0j})^k}{k!} ln(r(s)) \left\| \gamma'(s) \right\| ds \tag{3.31}$$

These expressions allow the representation of the functions φ and $\frac{\partial \varphi}{\partial n}$ by an arbitrary order of approximation by retaining the corresponding terms in the series. Although the geometry (the domain) is known, it is not easy to find a parametrization for a generic curve in space, which

means that it is convenient to express this curve by a Taylor series, as shown in (3.32).

$$\gamma(s) = \begin{cases} x(s) = x(s_0) + \sum_{j=0}^{\infty} x^{(j)}(s_0)\dfrac{(s-s_0)^j}{j!} \\ z(s) = z(s_0) + \sum_{j=0}^{\infty} z^{(j)}(s_0)\dfrac{(s-s_0)^j}{j!} \end{cases} \tag{3.32}$$

The last approximation to be done regards the normal vector, that should satisfy the condition (3.33) for any order of approximation and is almost completely defined by the unity norm condition (3.34), remaining only the external normal vector definition.

$$\vec{n}(s_0) \cdot \gamma'(s_0) = 0 \Rightarrow [x^* - x(s_0)]x'(s_0) + [z^* - z(s_0)]z'(s_0) = 0 \tag{3.33}$$

$$\sqrt{[x^* - x(s_0)]^2 + [z^* - z(s_0)]^2} = 1, \ \vec{n}(s_0) = (x^* - x(s_0), z^* - z(s_0)) \tag{3.34}$$

The Taylor series approximation for the potential function and the flux through the boundaries transform the problem variables from continuum functions to the corresponding Taylor series coefficients, which can then be evaluated by applying a collocation method. If one adopts a representation concerning only the first term of the potential function and line segments for the geometry, the method obtained is called as low order method. Otherwise, if the representation of the potential function and geometry is done by choosing more terms on their Taylor series, the method is generically referred as higher order.

The low order method leads to equation (3.35), which is discretized by a finite number of panels and when evaluated at all panels compose a fully determined linear system. Its solution provides the potential at the panels without any guarantee of continuity, recovering the continuum distribution when the number of panels increases to infinity.

The point where the potential and the flux will be evaluated inside each panel is arbitrary, but is common to adopt the midpoint. For the geometry, although the Taylor series could be written using an arbitrary point inside each panel, it is convenient to choose a point that guarantees the "connection" between the nodes of neighbor panels in order to avoid discontinuities in the geometry representation. The mean value theorem (3.36) guarantees the existence of such point.

$$-\pi\varphi_i + \sum_{j=0}^{N} \varphi_j \int_{P_j} \frac{\partial ln(r_{ij})}{\partial n_j} dl_j - \sum_{j=0}^{N} \frac{\partial \varphi_j}{\partial n_j} \int_{P_j} ln(r_{ij}) dl_j = 0, \ i = 1, 2, ..., N \tag{3.35}$$

$$x'(s^*) = \frac{x(s_2) - x(s_1)}{s_2 - s_1}, \quad z'(s^*) = \frac{z(s_2) - z(s_1)}{s_2 - s_1}, \quad s_1 \leqslant s \leqslant s_2 \tag{3.36}$$

The development above was done assuming the same parametrization for the geometry and potential function, but one could make use of different ones. It should be noticed that other expressions (not Taylor) could be created to represent both the potential function and the geometry, such as B-splines, NURBS[1] etc, leading to more complex expressions and involving new orders of approximation. All the approximation procedure was done concerning the velocity potential BVP. However, the procedure for the acceleration potential is analogous, providing (3.37).

$$-\pi\frac{\partial\varphi_i}{\partial t} + \sum_{j=0}^{N}\frac{\partial\varphi_j}{\partial t}\int_{P_j}\frac{\partial ln(r_{ij})}{\partial n_j}dl_j - \sum_{j=0}^{N}\frac{\partial}{\partial t}\left(\frac{\partial\varphi_j}{\partial n_j}\right)\int_{P_j}ln(r_{ij})dl_j = 0, \ i = 1, 2, ..., N \qquad (3.37)$$

The next step is to define the numerical scheme to be adopted for solving the integral equations for the boundary value problems together with the boundary conditions and the initial value problem. This will be done in the next chapter.

---

[1]Non Uniform Rational Basis Spline

Chapter 4

Numerical scheme

The numerical scheme implemented for solving the fluid-structure interaction is presented in this chapter. Some particularities adopted during the implementation, such as the ramp function and the numerical beach are also discussed. The first one to avoid an impulse response of the system, which could compromise the numerical stability, and the second one was used to avoid wave reflections at the domain' edges. The numerical integration method and the time marching scheme are also discussed. A simple method for the evaluation of the volume and water plan area of an arbitrary body using only the panels, required for free floating simulations, is shown in the Appendix A.

4.1 Linear system

4.1.1 Velocity potential

The linear system for the potential velocity BVP is shown in (4.1), where the terms A_{ij} and B_{ij} are given by (4.2) and (4.3), respectively. In the right hand side C_i^t is evaluated imposing the Neumman conditions at the body and other fixed and prescribed domain boundaries and the Dirichlet conditions at the free surface, as seen in (4.4), with N_B as the sum of the fixed,

prescribed motion and floating body panels and N as the total panels.

$$\begin{bmatrix} -\pi + A_{11} & A_{12} & A_{13} & ... & B_{1N-1} & B_{1N} \\ A_{21} & -\pi + A_{22} & A_{23} & ... & B_{2N-1} & B_{2N} \\ \vdots & & & & & \\ A_{N-11} & A_{N-12} & A_{N-13} & ... & B_{N-1N-1} & B_{N-1N} \\ A_{N1} & A_{N2} & A_{N3} & ... & B_{NN-1} & B_{NN} \end{bmatrix} \begin{bmatrix} \varphi_1^t \\ \varphi_2^t \\ \vdots \\ \left(\frac{\partial\varphi}{\partial z}\right)_{N-1}^t \\ \left(\frac{\partial\varphi}{\partial z}\right)_N^t \end{bmatrix} = \begin{bmatrix} C_1^t \\ C_2^t \\ \vdots \\ C_{N-1}^t \\ C_N^t \end{bmatrix} \tag{4.1}$$

$$A_{ij} = \int_{P_j} \frac{\partial ln(r_{ij})}{\partial n_j} dl_j \tag{4.2}$$

$$B_{ij} = \int_{P_j} ln(r_{ij}) dl_j \tag{4.3}$$

$$C_i^t = \begin{cases} \sum_{j=1}^{N_B} \left(\vec{V}\cdot\vec{n} - \frac{\partial\phi_I}{\partial n}\right)_j^t B_{ij} - \sum_{j=N_B+1}^{N} \varphi_j^t A_{ij}, & i = 1,2,...N_B \\ \sum_{j=1}^{N_B} \left(\vec{V}\cdot\vec{n} - \frac{\partial\phi_I}{\partial n}\right)_j^t B_{ij} - \sum_{j=N_B+1}^{N} \varphi_j^t(-\pi + A_{ij}), & i = N_B+1,...,N \end{cases} \tag{4.4}$$

The integral terms A_{ij} and B_{ij} are only geometry dependent since the linear approach was adopted, and they are constant along the whole simulation, being only evaluated once. The linear system for the velocity potential BVP can be summarized in (4.5), (4.6) and (4.7) and only the last term in (4.5) needs to be updated for each time step.

$$S_{NXN} \begin{bmatrix} (\varphi^t)_{N_B X1} \\ \left(\frac{\partial\varphi}{\partial z}\right)_{(N_{FS}X1)}^t \end{bmatrix} = R_{NXN} \begin{bmatrix} \left(\vec{V}\cdot\vec{n} - \frac{\partial\phi_I}{\partial n}\right)_{N_B X1}^t \\ (\varphi)_{(N_{FS}X1)}^t \end{bmatrix} \tag{4.5}$$

$$S_{NXN} = \left(-\pi \begin{bmatrix} I_{(N_B XN_B)} & 0_{(N_B XN_{FS})} \\ 0_{(N_{FS}XN_B)} & 0_{(N_{FS}XN_{FS})} \end{bmatrix} + [A_{(NXN_B)}, -B_{(NXN_{FS})}]\right) \tag{4.6}$$

$$R_{NXN} = \left(\pi \begin{bmatrix} 0_{(N_B XN_B)} & 0_{(N_B XN_{FS})} \\ 0_{(N_{FS}XN_B)} & I_{(N_{FS}XN_{FS})} \end{bmatrix} + [B_{(NXN_B)}, -A_{(NXN_{FS})}]\right) \tag{4.7}$$

4.1.2 Acceleration potential

The linear system for the acceleration potential BVP is similar to the one for the velocity potential one. However, there are some differences because of the floating bodies condition, since the acceleration term is eliminated by replacing the motion equation into the corresponding boundary condition. The linear system (4.8) is obtained with the floating body terms given by (4.9) and right side given by (4.10).

$$
\begin{bmatrix}
-\pi + A_{11} & A_{12} & D_{1,N_B-N_{FB}+1} & ... & B_{1N-1} & B_{1N} \\
A_{21} & -\pi + A_{22} & D_{2,N_B-N_{FB}+1} & ... & B_{2N-1} & B_{2N} \\
& & & & & \\
\vdots & & & & & \\
A_{N-11} & A_{N-12} & D_{N-1,N_B-N_{FB}+1} & ... & B_{N-1N-1} & B_{N-1N} \\
A_{N1} & A_{N2} & D_{N,N_B-N_{FB}+1} & ... & B_{NN-1} & B_{NN}
\end{bmatrix}
\begin{bmatrix}
\varphi_{t1}^t \\
\varphi_{t2}^t \\
\vdots \\
\frac{\partial}{\partial t}\left(\frac{\partial \varphi}{\partial z}\right)_{N-1}^t \\
\frac{\partial}{\partial t}\left(\frac{\partial \varphi}{\partial z}\right)_{N}^t
\end{bmatrix}
=
\begin{bmatrix}
C_1^t \\
C_2^t \\
\vdots \\
C_{N-1}^t \\
C_N^t
\end{bmatrix}
$$

(4.8)

$$
D_{i,j} = A_{ij} + \rho l_j (M^{-1}[n_{xj}, n_{zj}][n_{xj}, n_{zj}]^T + I_0^{-1}[-n_{xj}(z_j - z_G), n_{zj}(x_j - x_G)][-n_{xj}z_j, n_{zj}(x_j - x_G)]^T)
$$

(4.9)

$$C_i^t = \begin{cases} \displaystyle\sum_{j=1}^{N_B-N_{FB}} \left(\vec{a}\cdot\vec{n} - \frac{\partial}{\partial t}\frac{\partial\phi_I}{\partial n}\right)_j^t B_{ij} - \sum_{j=N_B-N_{FB}+1}^{N_B} \left(\frac{\partial}{\partial t}\frac{\partial\phi_I}{\partial n}\right)_j^t B_{ij} - \sum_{j=N_B+1}^{N} \varphi_j^t A_{ij} \\[2ex] \displaystyle -z_G^t \sum_{j=N_B-N_{FB}+1}^{N_B} M^{-1}n_{zj}\rho g L_{WL}B_{ij} \\[2ex] \displaystyle -\theta^t \sum_{j=N_B-N_{FB}+1}^{N_B} I_0^{-1}\rho g\nabla GM[-n_{xj}(z_j-z_G), n_{zj}(x_j-x_G)][-n_{xj}z_j, n_{zj}(x_j-x_G)]^T B_{ij}, \\[2ex] \quad i = 1, 2, ... N_B \\[1ex] \displaystyle\sum_{j=1}^{N_B-N_{FB}} \left(\vec{a}\cdot\vec{n} - \frac{\partial}{\partial t}\frac{\partial\phi_I}{\partial n}\right)_j^t B_{ij} - \sum_{j=N_B-N_{FB}+1}^{N_B} \left(\frac{\partial}{\partial t}\frac{\partial\phi_I}{\partial n}\right)_j^t B_{ij} - \sum_{j=N_B+1}^{N} \varphi_j^t(-\pi + A_{ij}) \\[2ex] \displaystyle -z_G^t \sum_{j=N_B-N_{FB}+1}^{N_B} M^{-1}n_{zj}\rho g L_{WL}B_{ij} \\[2ex] \displaystyle -\theta^t \sum_{j=N_B-N_{FB}+1}^{N_B} I_0^{-1}\rho g\nabla GM[-n_{xj}(z_j-z_G), n_{zj}(x_j-x_G)][-n_{xj}z_j, n_{zj}(x_j-x_G)]^T B_{ij}, \\[2ex] \quad i = N_B + 1, ..., N \end{cases} \tag{4.10}$$

4.2 Numerical integration

4.2.1 Spatial integration

There are two different integrals in the equations that need to be evaluated, concerning the Rankine source and the dot product of the source gradient by the normal vector. A numerical integration process is adopted using Gauss-Legendre quadrature with 4 points. The convergence was verified by evaluating the integrals with Gaussian points ranging from 4 to 8 and the results compared with the software Mathematica®, and no significant was observed. Therefore 4 points was assumed sufficient and this value was adopted for all the integration processes.

The spatial integrals that need to be performed are line integrals and so a parametrization must be found. The linear parametrization (4.11) was performed with the Jacobian equals to half the panel length and integral is changed by a weighted sum of the integrand values (4.12).

$$\gamma(s) = \begin{cases} x(s) = x_1 + \dfrac{(x_2 - x_1)(s+1)}{2} \\[2ex] z(s) = z_1 + \dfrac{(z_2 - z_1)(s+1)}{2} \end{cases} \quad -1 \leqslant s \leqslant 1 \tag{4.11}$$
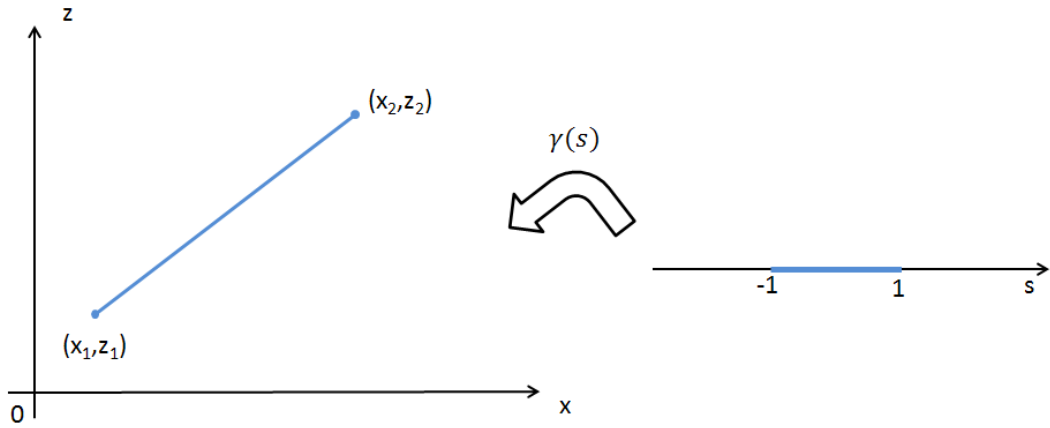
Figure 4.1: Isoparametric domain

$$\int f(x,z)dl = \int_{-1}^{1} f(\gamma(s)) \, \|J(s)\| \, ds \approx \sum_{i=0}^{N} w_i f(s_i) \qquad (4.12)$$

Actually, in a low order method the integrals could be performed analytically using a similar procedure to the one presented by Hess and Smith [1964] for tridimensional cases, requiring the coordinate system to be changed during the integrations to a local coordinate system at the panel side, as shown in Figure (4.2). However, since one of the goals of this work is the development of numerical procedures aiming at future improvements and one of them is the consideration of higher order methods, the integrals were performed numerically.
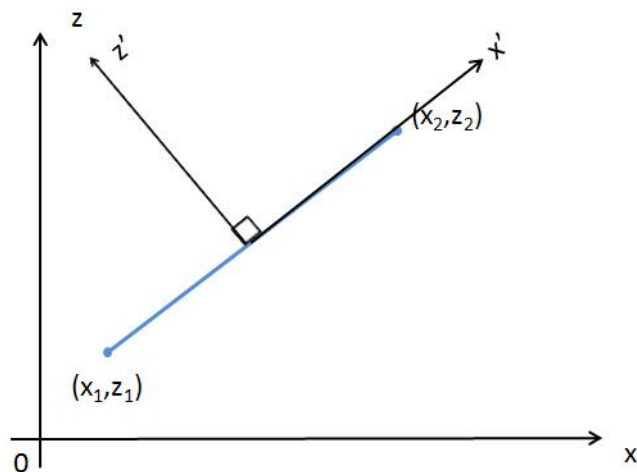
Figure 4.2: Changing coordinate system during integration

4.2.2 Time integration

The equations that guarantee the time marching solution are the free surface and body motion equations. The motion equations are already ODEs and the free surface equations were transformed from a system of PDEs into a system of ODEs because the flux through the free surface can be evaluated at all times through the acceleration potential BVP. The 4th order Runge-Kutta (RK-4) method was adopted, as suggested by Yang [2004], Koo [2003] and Tanizawa [2000], because it provides a large stability region and good accuracy. Although the predicted values are good, the computational cost is higher if compared to predictor/corrector schemes, since inside each time step the equations need to be evaluated 3 times, while the predictor/corrector schemes evaluate then only once per time step.

4.3 Additional Schemes

4.3.1 Ramp function

As discussed before, to avoid the system impulsive response a ramp function was adopted at the prescribed motion boundaries and for the incident wave potential. The ramp function adopted for the prescribed motion boundaries can be seen in (4.13), where U_x is the amplitude of the velocity and T_r is the ramp time (usually adopted as multiple of the motion period). The function adopted for the incident wave potential is basically the same, only the wave amplitude modified.

$$\vec{V}(t) \cdot \vec{n} = \begin{cases} \dfrac{1}{2}U_x[1 - \cos(\dfrac{\pi t}{T_r})], & if \quad t \leqslant T_r \\ U_x, & if \quad t > T_r \end{cases} \tag{4.13}$$

4.3.2 Numerical beach

In the offshore seakeeping context, the incident waves and the waves irradiated from the body usually cannot reflect and come back to the body. In the ocean, this occurs because the boundaries that could reflect part of the wave energy are usually far way and the energy is dissipated by non conservative forces or wave breaking before the reflected waves could come back to the body

considered in the analysis. In towing tanks there is usually a physical beach or active absorbers that avoid (at least partially) that the reflected waves come back to the model. The beach basic function is to dissipate the energy transported by the waves, but in the numerical simulation it is impossible to reproduce its physical behavior because all mathematical formulation is based on conservative fields and therefore no dissipation is expected.

There are two ways to overcome this inconvenient, both based on modelling some new equations or conditions: to transmit the energy through the domain boundaries or to artificially damp the waves. The most common condition that transmits the wave energy outside the domain is the so-called Sommerfeld boundary condition, which will be discussed latter in this text, associated to the wave-maker problem, presented ahead. However, the basic problem of these conditions is that, although they are usually very efficient for normal incidences of linear waves, the same is not true for oblique incidences or non-linear waves. Besides, these conditions are usually imposed for a single well defined frequency, having a narrow range of frequencies for which the condition will be efficient. Since for a fully developed ocean the frequencies have a large variation, the choice was done for a damping region, because, despite the beach factor being frequency dependent, it's efficiency is not restricted to a narrow range of frequencies.

The damping condition is also known as "sponge boundary condition" and was first proposed by Israeli and Orszag [1981]. It has been largely adopted on numerical simulations and satisfactory performances have been reported. Since there are some variations, the formulation here presented was taken from Zhen et al. [2010]. The condition is applied on both kinematic and dynamic free surface conditions, modifying them to (4.14) and (4.15), respectively, with d_{beach} being the distance between the generation region and the beginning of the damping zone and $\nu(x)$ being the damping function, define by (4.16) with a parabolic profile. The coefficients a and b define the intensity and length of the beach, respectively.

$$\frac{\partial \eta}{\partial t} = \frac{\partial \varphi}{\partial z} - \nu(x)\eta, \quad for \ z = 0 \ in \ |x| > d_{beach} \tag{4.14}$$

$$\frac{\partial \varphi}{\partial t} = -g\eta - \nu(x)\varphi, \quad for \ z = 0 \ in \ |x| > d_{beach} \tag{4.15}$$

$$\nu(x) = a\omega\left(\frac{x - d_{beach}}{b\lambda}\right)^2 \tag{4.16}$$

The choice of a and b values should be done carefully because low values for the a coefficient lead to an incomplete damping, while high values lead to numerical reflection in the beginning of the damping zone. The coefficient b defines the length of the beach and so the higher this value the smoother is the damping process for the same value of a coefficients. However, large damping zones have an impact on the computational performance because the domain must increase in order to avoid the damping zone influence at the region near the floating body. More details on this matter can be found in Engquist and Majda [1977], Kumar and Narayan [2008], Cao et al. [1993], Kim [2003] and Clement [1996].
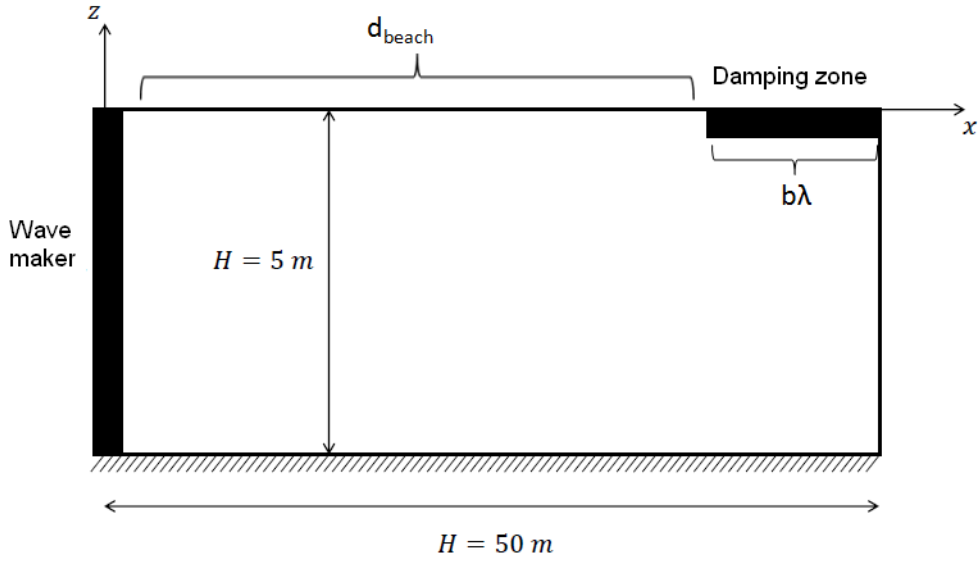
Figure 4.3: Wave-maker in a wave tank with 50 meters length and 5 meters depth

The behavior of this sponge layer can be understood in a simplified analysis by derivating expression (4.15) with respect to time and combining it with expression (4.14), obtaining (4.17).

$$\frac{\partial^2 \varphi}{\partial t^2} + g\frac{\partial \eta}{\partial t} + \nu(x)\frac{\partial \varphi}{\partial t} = 0 \Rightarrow \frac{\partial^2 \varphi}{\partial t^2} + g\frac{\partial \varphi}{\partial z} - g\nu(x)\eta + \nu(x)\frac{\partial \varphi}{\partial t} = 0, \ for \ z = 0 \ in \ |x| > d_{beach} \quad (4.17)$$

Eliminating the free surface elevation η from this equation using expression (4.15) leads to (4.18). Assuming φ as periodic in time ($\varphi = \phi(x, z)e^{i\omega t}$) and replacing in the previous equation leads to (4.19), which can be used to evaluate the wave number in the damping zone considering deep water condition in order to simplify the analysis $\left(k\phi = \dfrac{\partial \phi}{\partial z}\right)$.

$$\frac{\partial^2 \varphi}{\partial t^2} + g\frac{\partial \varphi}{\partial z} + 2\nu(x)\frac{\partial \varphi}{\partial t} + \nu(x)^2\varphi = 0 \qquad (4.18)$$

$$[-\omega^2 + 2\nu(x)i\omega + \nu(x)^2]\phi = -g\frac{\partial \phi}{\partial z} \qquad (4.19)$$

The wave number in the damping zone is then given by (4.20), which reveals an imaginary part in the frequency of oscillation, which will become a damping term of the potential function (4.21) in time. So, it can be seen that inside the damping zone the potential function will asymptotically go to zero, as the free surface elevation, since it should also be periodic ($\eta \propto e^{i\omega t}$).

$$k = \frac{\omega^2}{g} - \frac{\nu(x)^2}{g} - \frac{2\nu(x)i\omega}{g} \Rightarrow (\omega - \nu(x)i)^2 = kg \Rightarrow \omega = \pm\sqrt{kg} + \nu(x)i \qquad (4.20)$$

$$\varphi = \phi(x,z)e^{i\omega t} = \phi(x,z)e^{\pm i\sqrt{kg}t}e^{-\nu(x)t} \qquad (4.21)$$

Some brief tests were performed using the wave-maker shown in figure (4.3) and the conclusion was that at least one wave length should be used for the damping zone. In order to illustrate the results, a comparison of the free surface elevation η was done by changing the beach intensity coefficient a while keeping b fixed at a point located 6 meters far from the wave-maker. The time series of η can be seen in figure (4.4) for a wave period of 2 seconds.

As discussed before, without the damping zone (green line) there is a full reflection and the free surface elevation has the maximum value more than twice the generated wave amplitude. For the blue and red lines the wave is damped and it was important to verify that for an a coefficient equal to 2 (red line) the reflection was more intense and started at the beginning of the damping zone, due to a non-smooth damping process.

It was verified during the simulations performed that these coefficients should be adjusted for each case in order to balance the tradeoff between computational demand and satisfactory damping levels, specially because the "optimum"(here understood as the one that produces minimum wave reflection) coefficients value change with the wave frequency.
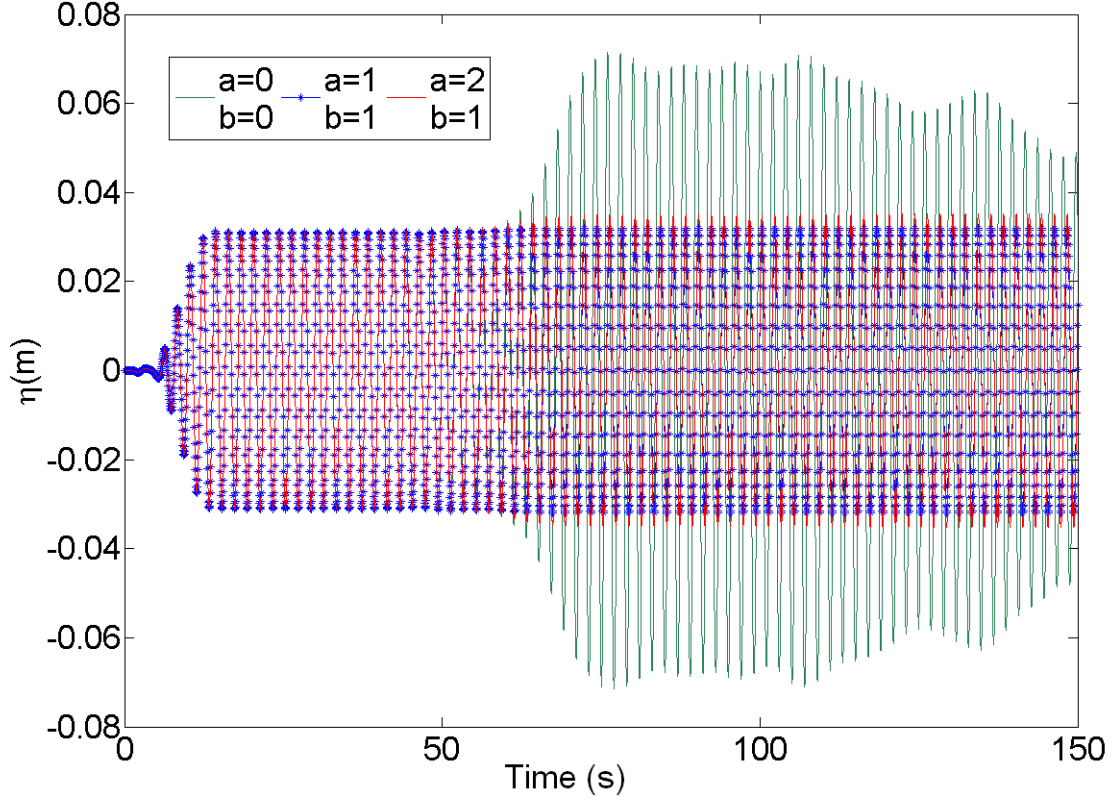
Figure 4.4: Comparison of free surface elevation for some beach coefficients for a point located 6 meters far from the wave-maker

In order to illustrate the effectiveness of the numerical beach with the wave frequency, the reflection coefficient was calculated changing the values of the coefficients a and b. The simulation setup is given in Table (4.1). The reflection coefficient was evaluated by tanking the wave amplitude average (H_1) of a point placed at the position x=10m before the reflected waves could come back to the numerical wave probe, neglecting the first crests (ramp effect), and then compared to the wave amplitude after reflection (H_2), using expression (4.22).

$$C_r = \frac{H_2 - H_1}{H_1} \qquad (4.22)$$

The reflection coefficients for several values of coefficients a and b are given in Figures (4.5) and (4.6). The results show that the higher the value of the beach length coefficient b, the lower is the reflection coefficient for an arbitrary frequency, but this conclusion cannot be extended to the intensity coefficient a, since there is an apparently strong non-linear dependence of the frequency.

Table 4.1: Simulation setup for reflection coefficient study

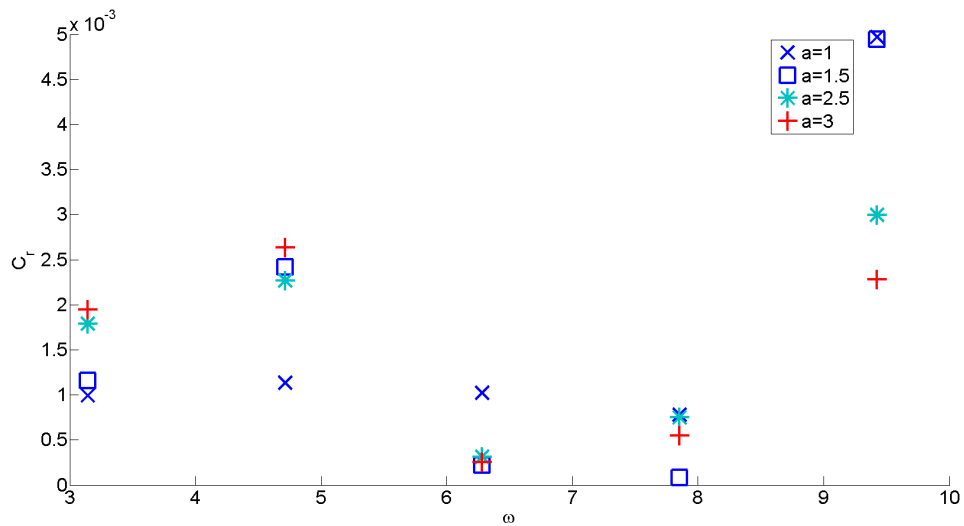| Description	Value	Unit
Length	50	m
Depth	5	m
Wave period	2	s
Velocity amplitude wave-maker	0.05	m/s
Time-step	0.05	s
Simulation time	200	s
Panel size	0.2	m
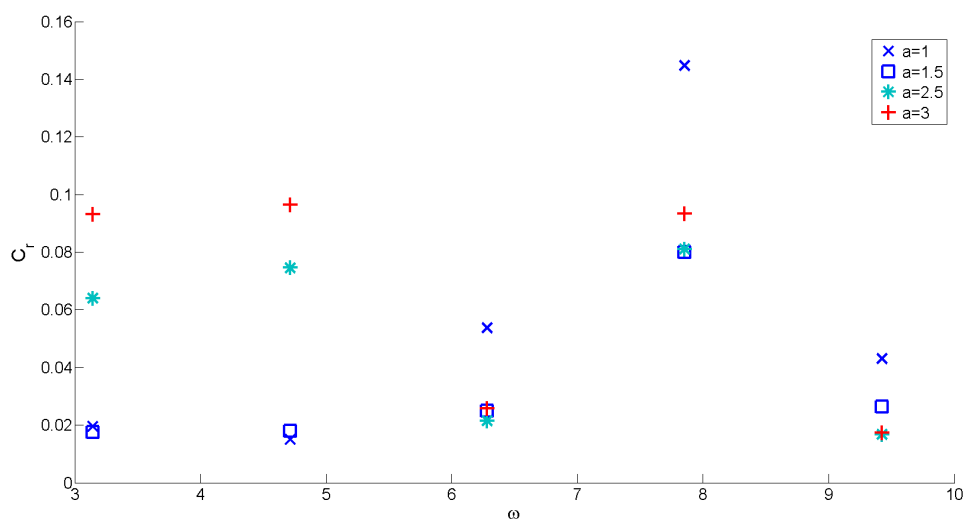
(a) beach length coefficient b=1
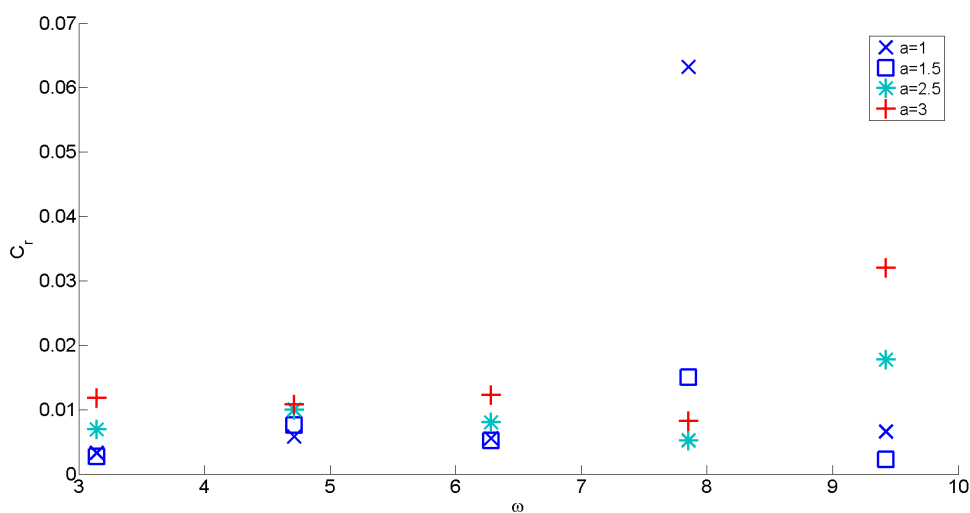
(b) beach length coefficient b=1.5

Figure 4.5: Reflection coefficient results 1
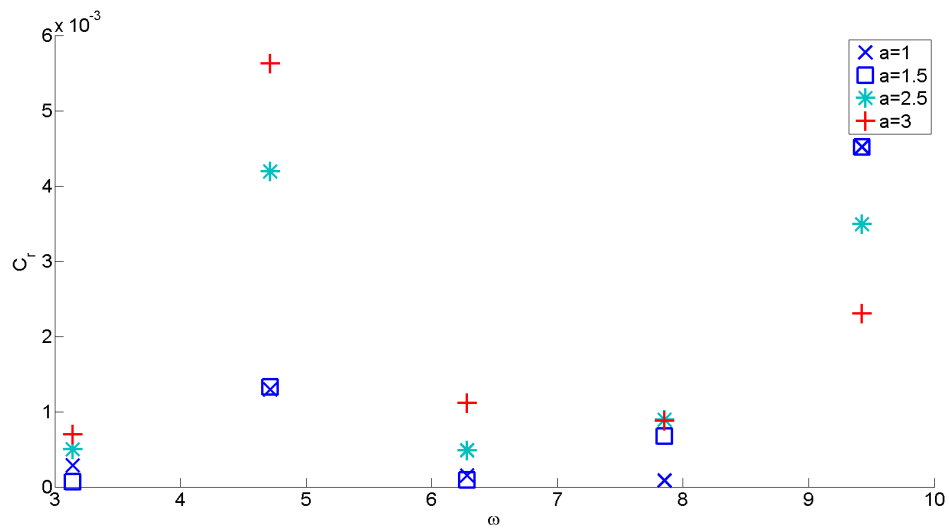
(a) beach length coefficient b=2.5

(b) beach length coefficient b=3

Figure 4.6: Reflection coefficient results 2

A longer study could be performed in order to investigate a procedure that could guarantee the beach effectiveness. However, since the numerical beach had a good performance during all simulations, this study was not deeply assessed.

Chapter 5

Numerical results

In this chapter the numerical results obtained using the theory developed in Chapter 2 and 3, combined with the numerical scheme presented in Chapter 4 are shown. The results were widely compared to analytical results, when available, or the results obtained with accepted numerical codes. Most of the compared results are obtained in frequency domain and a discussion concerning the methodology adopted for the comparison is performed before each result is presented.

The first tests were performed for the wave-maker problem, which the analytical solution was obtained assuming an eigenvector expansion procedure, as proposed by Dean and Dalrymple [2000].

The next tests were for the added mass and wave damping coefficients evaluation of simple 2D sections (circular and rectangular), reproducing Vugts [1968] experimental results and comparison considering Pesce [1988] and van Daalen [1993] numerical results. For the rectangular section an analytical solution was also available, first presented by Black et al. [1971] and re-presented by Zheng et al. [2004].

On these first simulations, the acceleration potential was not essential to guarantee the numerical stability, since the body position is force independent, which is not true for a free floating body. In order to evaluate the stability of free floating bodies simulation, the decay tests of simple cylinders were performed and the results compared with the numerical ones presented by van Daalen [1993].

However, none of the simulations until performed considered the analytic incident wave potential and, in order to evaluate this important consideration, the response amplitude operator (RAO) of a simple rectangular section was evaluated. The results were compared to the numerical ones presented by Tanizawa et al. [1999] and the analytical one combining the radiation and diffrac-

tion potentials as briefly discussed in section 2.3, evaluated following the methodology presented by Zheng et al. [2004].

5.1   Wave-maker problem

In order to validate the numerical method the first problem studied was the one of a wave-maker, which is a classical hydrodynamic problem with a useful result since it can be used on the analysis of ocean basins. The problem is sketched in Figure 5.1, and consists in solving Laplace's equation with the linearized free surface condition, the impermeability of the wave generator and bottom using a radiation condition on the x axis for $x \to \infty$, since the solution is obtained in frequency domain. The radiation condition is the one that defines the correct direction of energy propagation in frequency domain, because the solution is evaluated using separation of variables, leading to a non-unique solution if this condition is not enforced. The physically consistent one is preserved by this condition, defining that the energy goes from the wave-maker to the infinity and not the opposite.
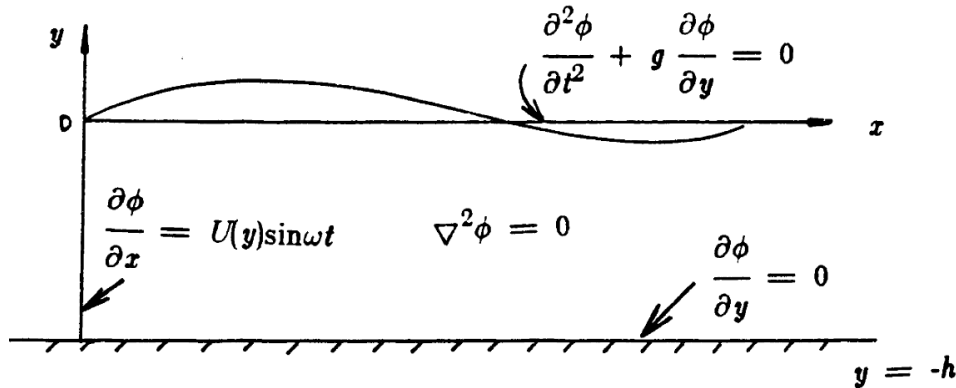
Figure 5.1: Wave-maker boundary value problem (Source:Lin [1984])

The radiation condition usually adopted is the Sommerfeld radiation condition, generically stated in (5.1), where n is the dimension of the space (3 for 3D problems and 2 for 2D problems) and k is the wave-number and i the imaginary unit. Further details can be found in Sommerfeld [1949].

$$\lim_{|x| \to \infty} |x|^{\frac{n-1}{2}} (\frac{\partial}{\partial |x|} - ik)\varphi(\vec{x}, t) = 0 \tag{5.1}$$

For the bidimensional problem this condition can be simplified into (5.2), where the x coordinate increases to infinity and the only way to get a feasible solution is imposing that the parenthesis term is zero or goes to zero faster than the x coordinate increases and for a generic case it is

69

simpler to impose directly the parenthesis term as zero.

$$\lim_{x \to \infty} \sqrt{x}(\frac{\partial \varphi}{\partial x} - ik\varphi) = 0 \Rightarrow \frac{\partial \varphi}{\partial x} - ik\varphi = 0 \tag{5.2}$$

The linear solution to this problem was first shown by Havelock [1963] using Fourier integral theorem, for the wave-maker with velocities profile given by the right side of (5.3), where $U(y)$ can be an arbitrary function of y and the wave-maker is considered as vertical and plane, changing the flux condition by the x derivative of the potential function, since the external normal vector is $-\hat{x}$.

$$\frac{\partial \varphi}{\partial n} = \frac{\partial \varphi}{\partial x} = -U(y)\sin(\omega t), \quad at \quad x = 0 \tag{5.3}$$

However, there are methods to compose the solution (not the Fourier Integral Theorem adopted by Havelock), such as the eigenvector decomposition, which is shown on Dean and Dalrymple [2000] and is adopted here, consisting in composing the full solution by the simple sum of basic harmonic functions, as can be seen in (5.4). The wave-maker kinematic boundary condition is applied in order to get the correct potential function that provides the correct $U(y)$ velocity profile at the wave-maker.

Examining the candidate solutions in (5.4), it is possible to verify that the constant B could take any value without changing the boundary value problem and so it is arbitrarily set as zero. The constant A should also be zero because it will never respect the impermeability at the wave-maker since the motion must be periodic.

$$\varphi(\vec{x}, t) = A_p \cosh[k_p(h + y)]\cos(k_p x - \omega t) + (Ax + B) + Ce^{-k_p x}\cos[k_s(h + y)]\sin(\omega t) \tag{5.4}$$

Replacing the potential into the linearized free surface condition for periodic solutions (5.5) leads to the so-called dispersion relation for progressive waves and a relation for the stationary solution (evanescent wave) as can be seen in (5.6).

$$\frac{\partial \varphi}{\partial y} - \frac{\omega^2 \varphi}{g} = 0, \quad at \quad y = 0 \tag{5.5}$$

$$\omega^2 = gk_p \tanh(k_p h), \quad \omega^2 = -gk_s \tan(k_s h) \tag{5.6}$$

The progressive wave for finite depth has a known potential, given by the first term in (5.4), where k_p is the real positive root of the dispersion relation (the negative root should be dropped

in order to keep the correct propagation direction). The evanescent wave has infinite possible values of k_s, since the frequency wave-number equation has an infinite number of solutions and all positive real roots should be taken. The final solution form is (5.7) and all constants are determined using the boundary condition (5.3).

$$\varphi(\vec{x}, t) = A_p \cosh[k_p(h + y)] \cos(k_p x - \omega t) + \sum_{n=1}^{\infty} A_n e^{-k_s(n)x} \cos[k_s(n)(h + y)] \sin(\omega t) \quad (5.7)$$

Applying this condition leads to the equation (5.8) and all $cosh[k_s(n)(h + y)]$ combinations or $cos[k_s(n)(h + y)]$ to $cosh[k_s(n)(h + y)]$ are orthogonal (except the combination of $k_s(n)$ with itself), so they are the eigenvectors of the problem and the wave-numbers k_p and $k_s(n)$ are the corresponding eigenvalues, which means that the coefficients can be calculated using (5.9), which is obtained by multiplying the equation (5.8) by the $\cos[k_s(n)(h + y)]$, integrating both sides on the interval [-h,0] and taking advantage of the orthogonality.

$$-U(y) = A_p k_p \cosh[k_p(h + y)] - \sum_{n=1}^{\infty} C_n k_s(n) \cos[k_s(n)(h + y)] \quad (5.8)$$

$$A_p = -\frac{\int_{-h}^{0} U(y) \cosh[k_p(h + y)] dy}{k_p \int_{-h}^{0} \cosh^2[k_p(h + y)] dy} \qquad C_n = \frac{\int_{-h}^{0} U(y) \cos[k_s(n)(h + y)] dy}{k_s(n) \int_{-h}^{0} \cos^2[k_s(n)(h + y)] dy} \quad (5.9)$$

Looking more carefully into the series solution it is possible to identify two types of waves, one progressive and the other local oscillations (evanescent modes), the last one due to the non-exponential velocity profile generated by the traditional wave-maker shape (flaps and pistons).

5.1.1 Piston type wave-maker

The solution for this kind of wave-maker is given by (5.10), supposing the velocity profile (5.11).

$$\varphi(\vec{x}, t) = \frac{4U \sinh(k_p h) \cosh[k_p(h + y)]}{k_p[\sinh(2k_p h) + 2k_p h]} \cos(k_p x - \omega t) -$$

$$\sin(\omega t) \sum_{n=1}^{\infty} \frac{4U \sin(k_s(n)h) \cos[k_s(n)(y + h)]}{k_s(n)[sin(2k_s(n)h) + 2k_s(n)h]} e^{-k_s(n)x} \quad (5.10)$$

$$U(y) = U \quad (5.11)$$

The free surface elevation can be determined using the linearized dynamic free surface con-

dition, obtaining (5.12).

$$\eta(x,t) = -\frac{2U\omega \sinh(2k_p h)}{gk_p[\sinh(2k_p h) + 2k_p h]} \sin(k_p x - \omega t)+$$

$$\cos(\omega t) \sum_{n=1}^{\infty} \frac{2U\omega \sin(2k_s(n)h)}{k_s(n)[sin(2k_s(n)h) + 2k_s(n)h]} e^{-k_s(n)x} \quad (5.12)$$

In order to validate the numerical results a numerical tank was created, the simulation performed using the setup conditions given by table (5.1). Three different numerical meshes were used with 275, 550 and 1100 panels. All the meshes were uniform, meaning that all their panels had the same length. A numerical wave probe was positioned at the position x=25m

Table 5.1: Simulation setup for piston wave-maker

Description	Value	Unit
Length	50	m
Depth	5	m
Wave period	2	s
Velocity amplitude wave-maker	0.05	m/s
Time-step	0.05	s
Simulation time	50	s
Beach coefficient "a"	1	-
Beach length "b"	1	-

(half the tank length) and the free surface elevation time series at this position was obtained and compared to the analytical solution, as can be seen in Figure (5.2). In order to better visualize the results, a zoom was applied and the results showed in figure (5.3), which demonstrates that for more than 550 panels the results had a very good agreement with the analytical ones. The numerical damping zone (beach) worked fine since no visual wave reflection was observed, meaning that the a and b coefficients equal to one were enough to guarantee a satisfactory simulation.
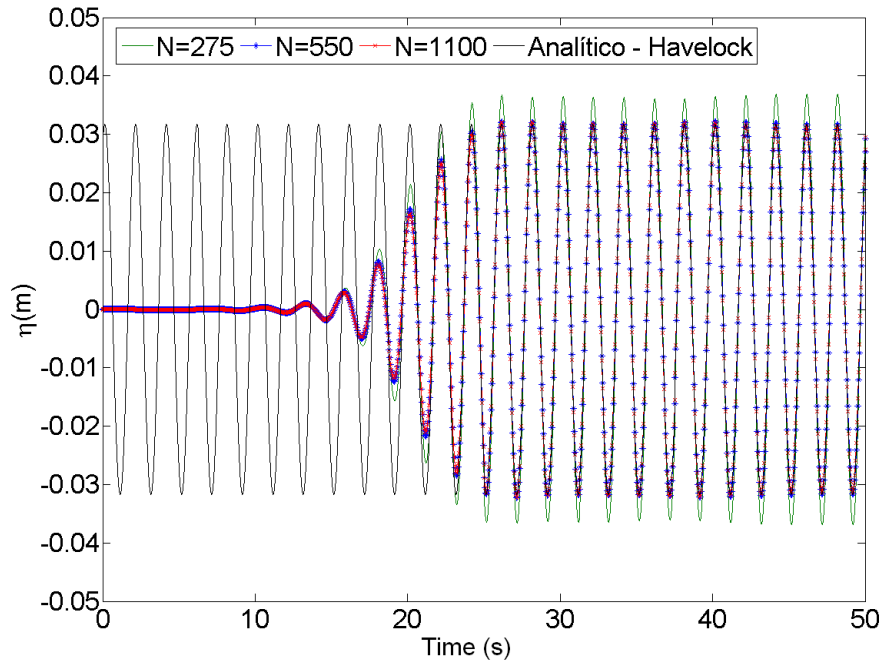
Figure 5.2: Time series for a wave probe at x=25m
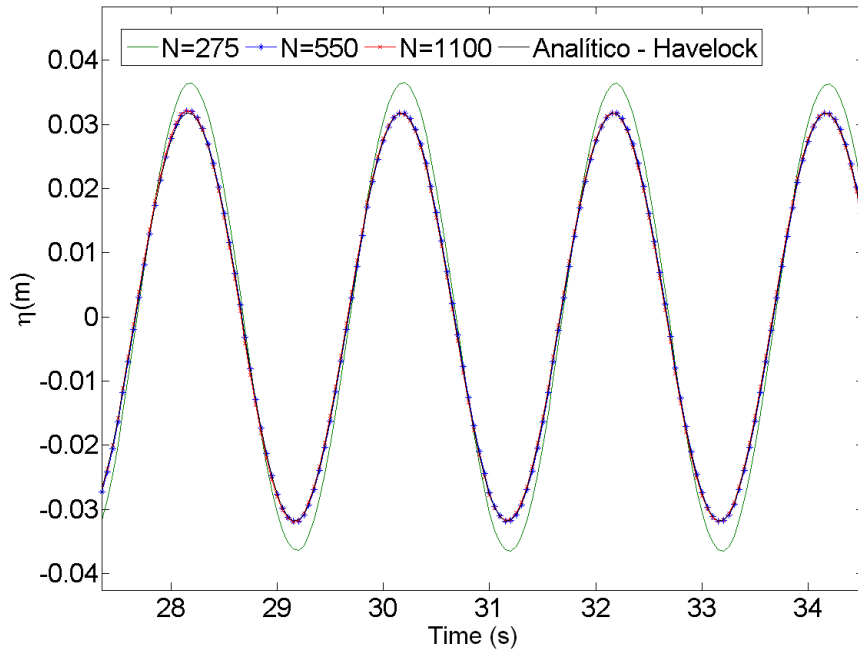
Figure 5.3: Zoom at time series for a wave probe on x=25m

For a more comprehensive verification, other wave frequencies were tested following the same methodology discussed above at the same numerical wave tank. The wave-maker transfer function concerning the probe at half the tank length was evaluated using the 550 panel mesh and the numerical results compared to the analytical predictions, as can be seen in Figure (5.4), where A is the wave amplitude of the generated wave at the probe and S is the piston stroke.

Once again a good agreement is observed.
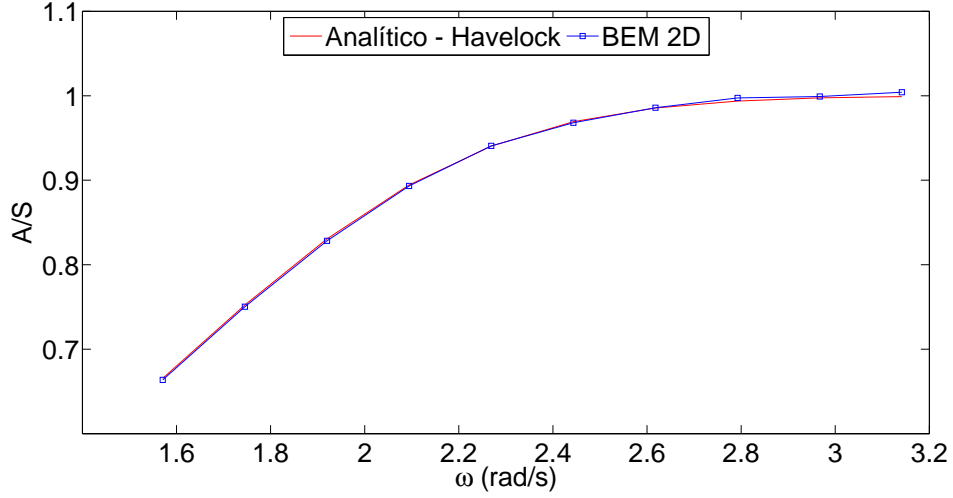
Figure 5.4: Piston-type wave-maker transfer function

5.1.2 Flap type wave-maker

The flap type wave-maker is very used on ocean basins, such as the TPN one, so the same study performed to piston type was reproduced. The velocity profile function is given in (5.13) and the potential function for this wave-maker in (5.14).

$$U(y) = U(1 + \frac{y}{h}) \tag{5.13}$$

$$\varphi(\vec{x}, t) = \frac{4U[1 + k_p h \sinh(k_p h) - \cosh(k_p h)] \cosh[k_p(h + y)]}{k_p^2 h[\sinh(2k_p h) + 2k_p h]} \cos(k_p x - \omega t) -$$

$$\sin(\omega t) \sum_{n=1}^{\infty} \frac{4U[-1 + k_s(n)h \sin(k_s(n)h) + \cos(k_s(n)h)] \cos[k_s(n)(y + h)]}{k_s^2(n)h[sin(2k_s(n)h) + 2k_s(n)h]} e^{-k_s(n)x} \tag{5.14}$$

Using the linearized dynamic free surface condition again, the free surface elevation (5.15) is obtained.

$$\eta(x, t) = -\frac{4U\omega[1 + k_p h \sinh(k_p h) - \cosh(k_p h)] \cosh(k_p h)}{gk_p^2 h[\sinh(2k_p h) + 2k_p h]} \sin(k_p x - \omega t) +$$

$$\cos(\omega t) \sum_{n=1}^{\infty} \frac{4U\omega[-1 + k_s(n)h \sin(k_s(n)h) + \cos(k_s(n)h)] \cos(k_s(n)h)}{gk_s^2(n)h[sin(2k_s(n)h) + 2k_s(n)h]} e^{-k_s(n)x} \tag{5.15}$$

The simulation setup can be seen in Table (5.2) with a mesh that contains 1550 panels, considering a 0.2m panel size. The result for the transfer function of the wave-maker can be

seen in Figure (5.5), with a good agreement of the results, except for a small shift in the curve for high frequencies. These differences suggested that the convergence was not achieved yet and, in order to minimize the discretization error, a simulation was performed with half the panel size (0.1m), obtaining the results shown in Figure (5.6). A comparison of the results can be seen in Table (5.3), where it can be verified that the differences between the finest mesh and the analytic solution is less than 3%.

Table 5.2: Simulation setup for piston wave-maker

Description	Value	Unit
Length	150	m
Depth	5	m
Velocity amplitude wave-maker	0.05	m/s
Time-step	0.05	s
Simulation time	100	s
Beach coefficient "a"	1	-
Beach length "b"	1	-
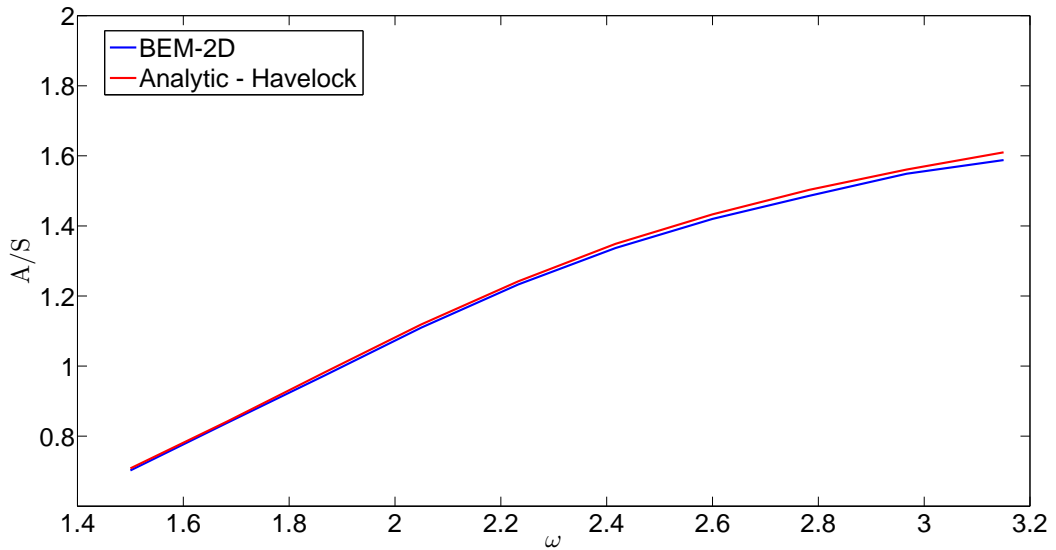
Figure 5.5: Flap-type wave-maker transfer function h=0.2m
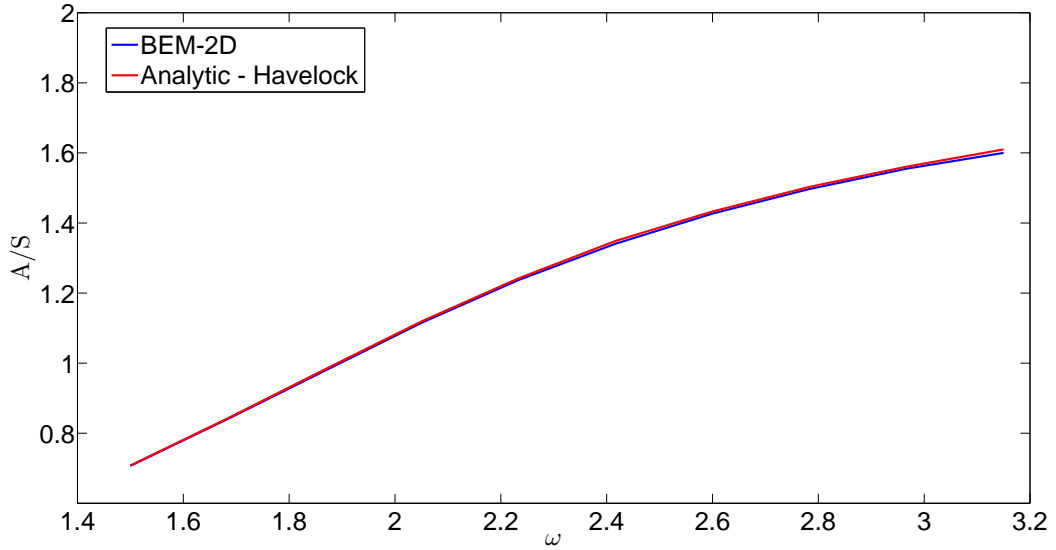
Figure 5.6: Flap-type wave-maker transfer function h=0.1m

Table 5.3: Ratio A/S for the flap wave-maker comparison

ω	Analytic-Havelock	BEM-2D (h=0.2m)	BEM-2D (h=0.1m)
1.500	0.708	0.702	0.707
1.683	0.842	0.838	0.840
1.867	0.982	0.973	0.978
2.050	1.119	1.110	1.115
2.233	1.242	1.233	1.237
2.417	1.349	1.337	1.341
2.600	1.433	1.420	1.427
2.783	1.503	1.486	1.497
2.967	1.561	1.549	1.555
3.150	1.610	1.588	1.600

5.2   Added mass and wave damping coefficients of simple forms

When a floating body is excited by ocean waves, energy is transferred from the wave to the body, generating motion. However, the body motions also transfer energy from the body to the water, being this phenomenon known as radiation problem.

In the linear analysis, the hydrodynamic force can be segregated in two components: one in phase with the body acceleration and another in phase with it's velocity, meaning that the first one can be summed with the body mass as an added mass and the second one acts as an external damping, as indicated in (5.16) and (5.17), where y is the horizontal axis and z the vertical one. The terms a_{ii} represents the added mass, b_{ii} the wave damping and c_{ii} the hydrostatic restoring.

76

In these expressions, eventual cross terms are neglected and the hydrostatic coefficient for y direction is set as zero because there is no hydrostatic restoration in this direction.

$$F_y(t) = (M + a_{yy})\ddot{y}_G + b_{yy}\dot{y}_G + c_{yy}y_G \tag{5.16}$$

$$F_z(t) = (M + a_{zz})\ddot{z}_G + b_{zz}\dot{z}_G + c_{zz}z_G \tag{5.17}$$

These coefficients can be experimentally evaluated through a forced oscillation test, where a prescribed motion like (5.18) is imposed and the dynamic forces are measured. Since the motion is periodic, a periodic behavior is expected in the hydrodynamic forces, as can be seen in (5.19) and (5.20), with a relative phase α_i between motion and force.

$$y_G(t) = a_y \sin(\omega t) \qquad z_G(t) = a_z \sin(\omega t) \tag{5.18}$$

$$F_y(t) = \int_{WS} p n_y dS = -\rho \int_{WS} \frac{\partial \varphi}{\partial t} n_y dS = A_y \sin(\omega t + \alpha_y) \tag{5.19}$$

$$F_z(t) = \int_{WS} p n_z dS = -\rho \int_{WS} \frac{\partial \varphi}{\partial t} n_z dS = A_z \sin(\omega t + \alpha_z) \tag{5.20}$$

Replacing these prescribed motions into the motion equations leads to the simple (5.21) and (5.22) formulas for the added mass and potential damping evaluation.

$$a_{yy} = -\frac{A_y \cos(\alpha_y)}{\omega^2 a_y} \qquad b_{yy} = \frac{A_y \sin(\alpha_y)}{\omega a_y} \tag{5.21}$$

$$a_{zz} = \frac{a_z c_{zz} - A_z \cos(\alpha_z)}{\omega^2 a_z} \qquad b_{zz} = \frac{A_z \sin(\alpha_z)}{\omega a_z} \tag{5.22}$$

In order to validate the numerical method, the forced oscillation test was numerically reproduced and the results compared with the experimental data from Vugts [1968], numerical results from Pesce [1988] (frequency domain) and van Daalen [1993] numerical results (time domain). The last one used a fully non-linear time domain boundary element method. For the rectangular section an analytical solution by eigenvector expansion (similar to the wave-maker problem) was obtained following the procedures first presented by (Black et al. [1971]) and reproduced by (Zheng et al. [2004]).

5.2.1 Circular section cylinder

The initial test was performed using a circular section as shown in Figure (5.7) with radius of 1m and the section placed exactly at the half the length of the tank. The range of frequencies tested were from 0.78 rad/s to 6.26 rad/s, leading to very long waves for the lowest frequencies (almost 100m of wave length). To overcome the problem of wave reflection, the damping zone influence in the body pressure and finite depth, large domains were adopted during the simulations. However, it is intuitive that for shorter waves the panel size should be smaller in order to capture the physical phenomena better and the use of large domain increases the number of panels. For this reason, the first step was the study of the domain and panel sizes to verify the ones that could capture the phenomena. The wave length was always evaluated using the dispersion relation and wave-number relation for deep waters (5.24) and the study was performed for three dimensionless frequencies, $\hat{\omega} = 0.25$, $\hat{\omega} = 1.00$ and $\hat{\omega} = 2.00$, with wave lengths of 100.53m, 6.28m and 1.57m, respectively. The domains were adopted with 500m, 60m and 60m length. The bottom influence was also studied in order to verify the sufficient values to guarantee the deep water condition, it is, no bottom influence.

For comparison purposes the results are non-dimensional according to (5.23), where $\rho = 1000 kg/m^3$ is the water density and $\forall = \pi R^2/2$ is the displacement by unit of length, supposing that the equilibrium position has the radius as draft.

$$\hat{\omega} = \omega\sqrt{\frac{R}{g}}, \quad \hat{a}_{xx} = \frac{a_{xx}}{\rho\forall}, \quad \hat{b}_{xx} = \frac{b_{xx}}{\rho\forall}\sqrt{\frac{R}{g}}, \quad \hat{a}_{zz} = \frac{a_{zz}}{\rho\forall}, \quad \hat{b}_{zz} = \frac{b_{zz}}{\rho\forall}\sqrt{\frac{R}{g}} \tag{5.23}$$

The added mass and potential damping coefficients variation with depth can be seen in Figures (5.9), (5.10) and (5.11). It was verified that for the highest frequency the ratio depth/wave length to guarantee the deep water condition is higher than the one for the smallest frequency. Since the method proposed is a time domain, the direct result obtained from the simulation is the time series of the hydrodynamic force, as can be seen in Figure (5.8) as an example.
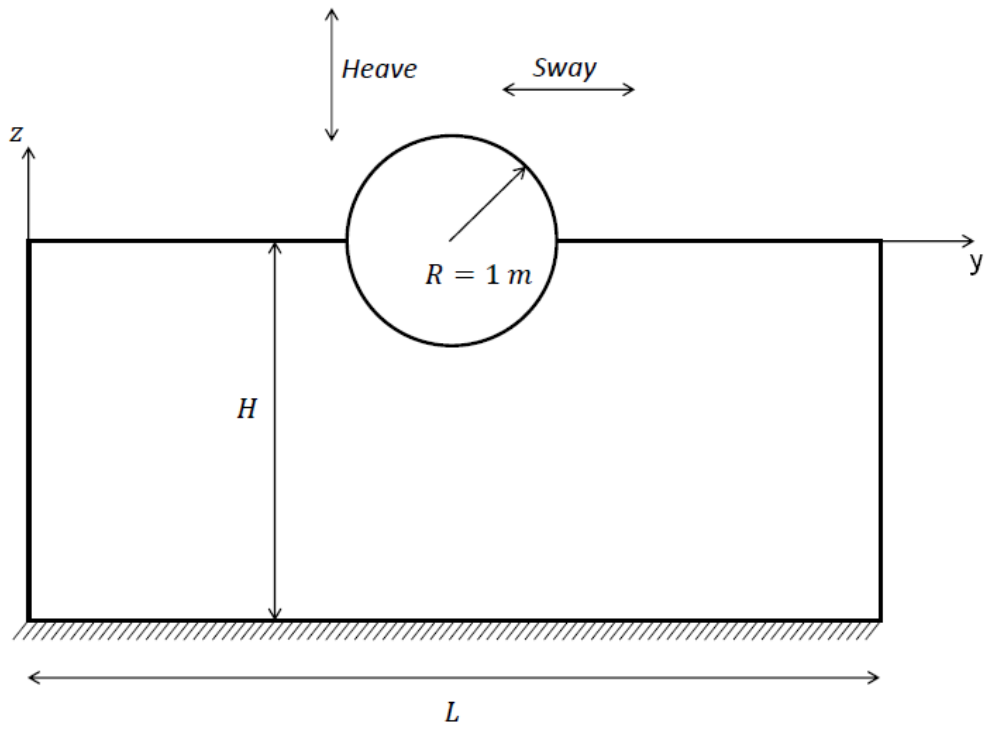
Figure 5.7: Circular section forced oscillation test

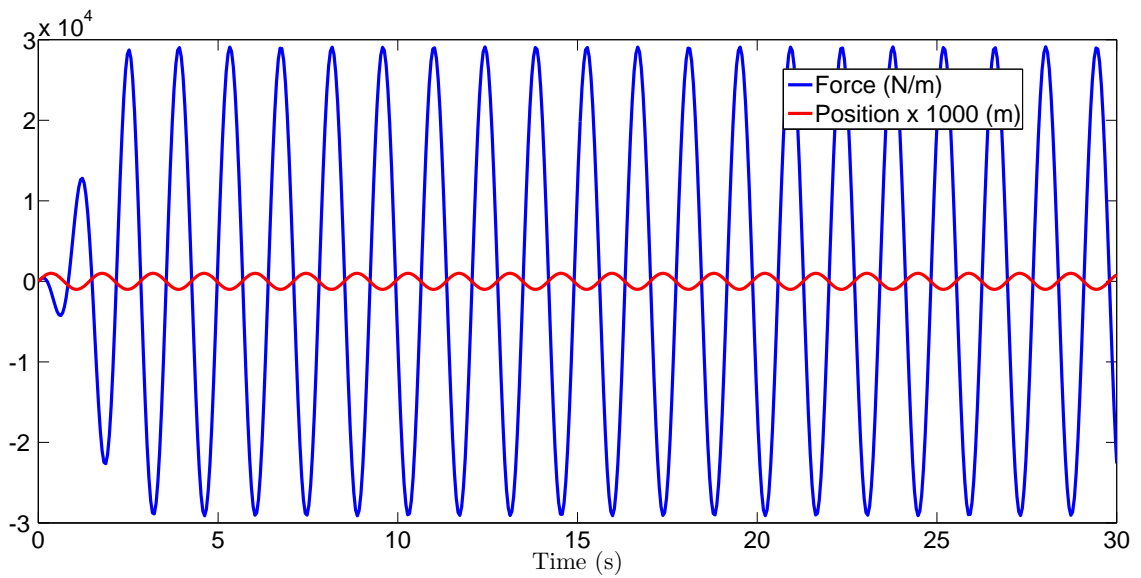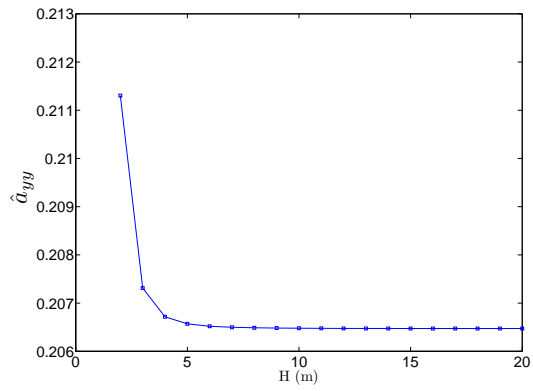$$k = \frac{2\pi}{\lambda} \stackrel{deepwater}{=} \frac{\omega^2}{g} \qquad (5.24)$$

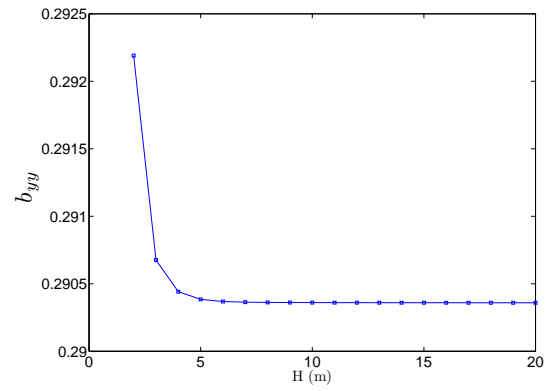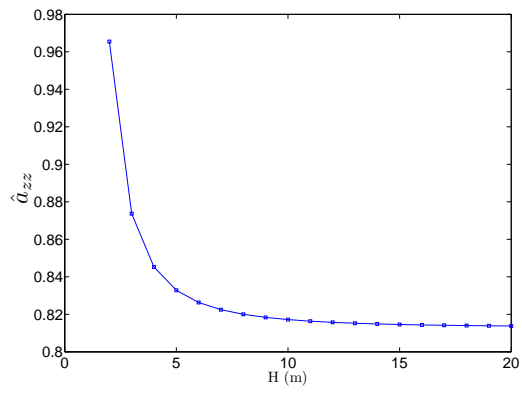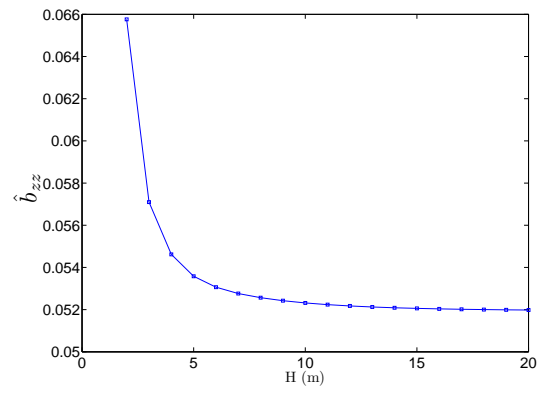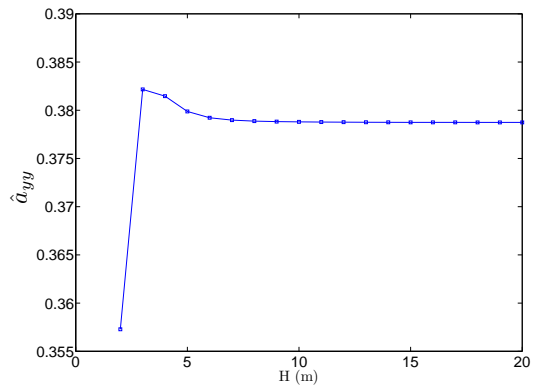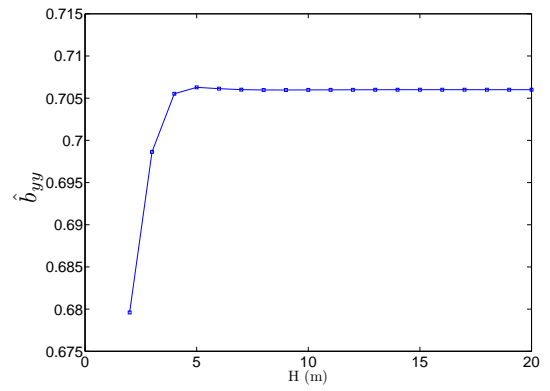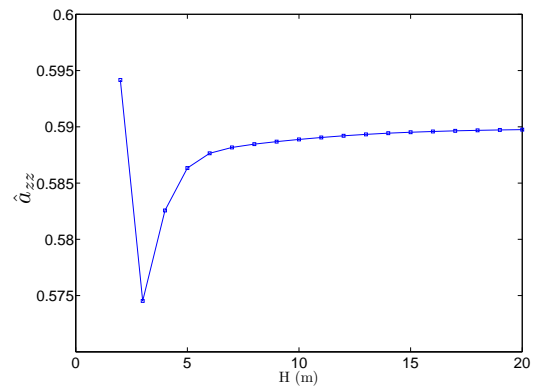Figure 5.8: Force and position series example

Figure 5.9: Variation of added mass ($\hat{a}_{yy}$, $\hat{a}_{zz}$) and potential damping ($\hat{b}_{yy}$, $\hat{b}_{zz}$) coefficients changing depth H for the dimensionless frequency $\hat{\omega} = 2$ for the circular section.
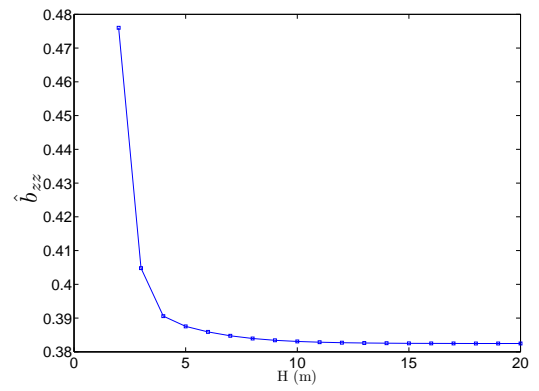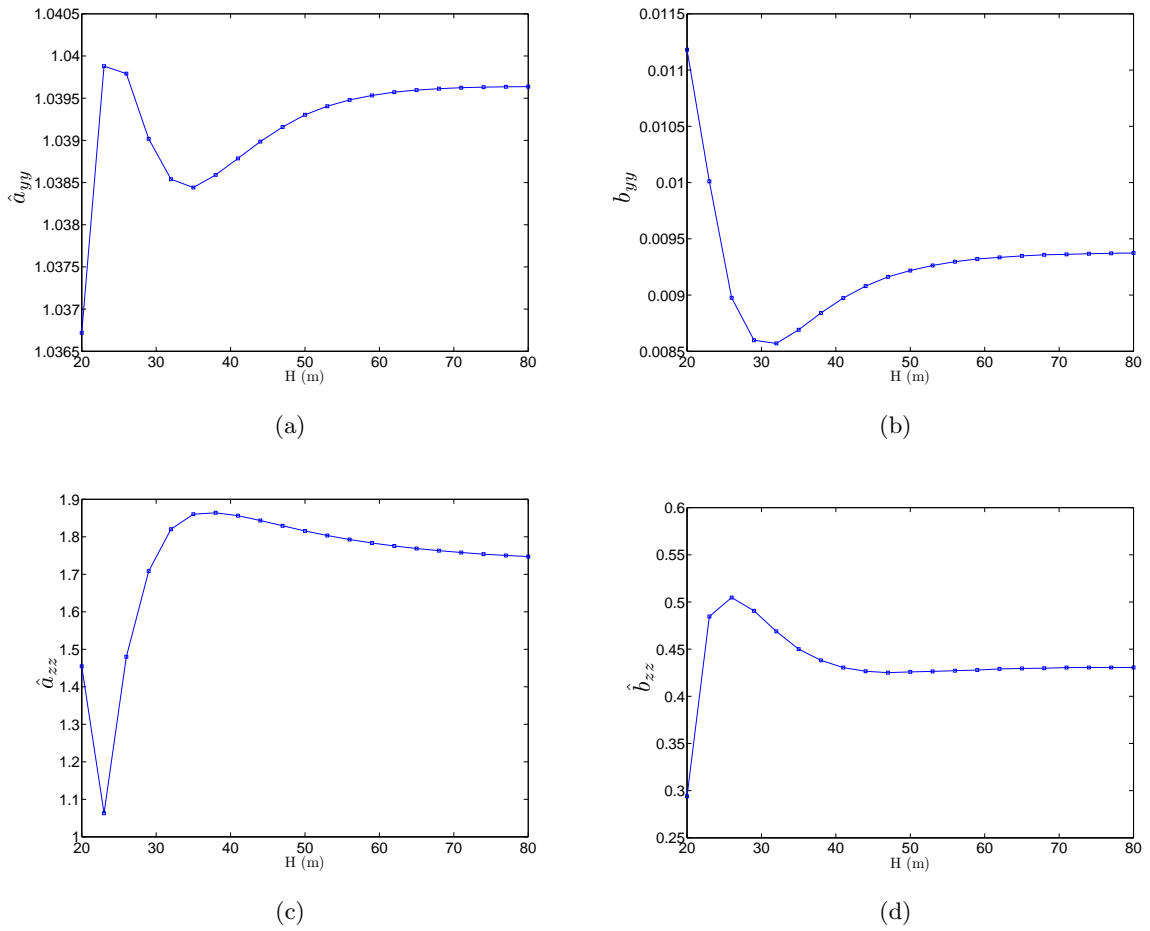
Figure 5.10: Variation of added mass ($\hat{a}_{yy}$, $\hat{a}_{zz}$) and potential damping ($\hat{b}_{yy}$, $\hat{b}_{zz}$) coefficients changing depth H for the dimensionless frequency $\hat{\omega} = 1$ for the circular section.

Figure 5.11: Variation of added mass $(\hat{a}_{yy},\ \hat{a}_{zz})$ and potential damping $(\hat{b}_{yy},\ \hat{b}_{zz})$ coefficients changing depth H for the dimensionless frequency $\hat{\omega} = 0.25$ for the circular section.

This study allowed the depth determination in order to avoid bottom influence, as shown in Table (5.4), which was adopted for both heaving and swaying.

Table 5.4: Domain dimensions for forced oscillation test of a circular section

$\hat{\omega}$	L(m)	H(m)
2.00	60	8
1.00	60	8
0.25	500	80

The discretization error were also evaluated changing the number of elements in order to guarantee the convergence. To reduce the computational effort, the meshes built were stretched, allowing the concentration of elements near the body. An example of a stretched mesh can be seen in Figure (5.12), where the red circles are the element vertices and the blue symbol the center of the elements. The stretched meshes tested are in Table (5.5), ranging from 0.05m elements up to 0.8m ones. The stretching formula adopted was a simple geometric series with a stretching factor γ, as can be seen on (5.25), where l_{min} is the smallest panel size and N the

82

number of panels in a given direction (left and right of the body). However, since the sum of these panels size may not be exactly the geometry length, the stretching factor needed to be adjusted in order to keep the number of panels and geometric length, using (5.26). Additionally there were also a maximum panel size l_{max} in order to avoid excessive large panels.

$$l_i = l_{min}(1 + \gamma)^i, \; i = 0, 1, 2, .., N - 1 \tag{5.25}$$

$$l_{geo} = l_{min} \frac{(\gamma^{*N-1})}{\gamma^* - 1} \tag{5.26}$$
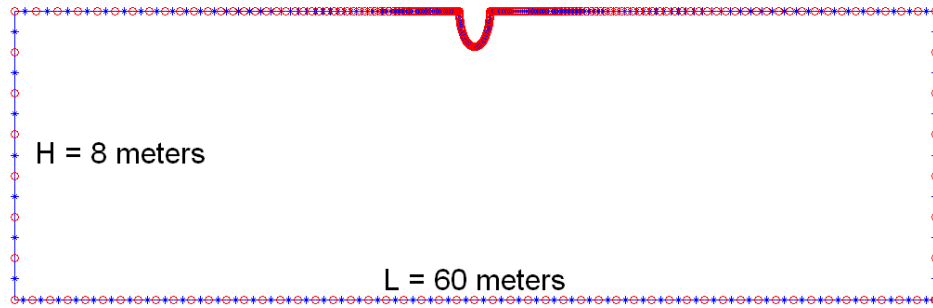
Figure 5.12: Mesh for circular section with stretching and number of panels $N = 279$

Table 5.5: Stretched meshes tested for numerical forced oscillation test of a circular section

$\hat{\omega}$	N_1	N_2	N_3	N_4	N_5
2.00	124	150	183	224	279
1.00	124	150	183	224	279
0.25	199	229	262	305	360

The convergence analysis concerning the panel size can be seen in Figures (5.13), (5.14), (5.15), (5.16), (5.17) and (5.18) and shows that a mesh with 183 elements would be enough for the dimensionless frequencies $\hat{\omega} = 1.00$ and $\hat{\omega} = 2.00$ concerning engineering purposes. However for the dimensionless frequency $\hat{\omega} = 0.25$ a bigger mesh with 262 panels would be recommended.
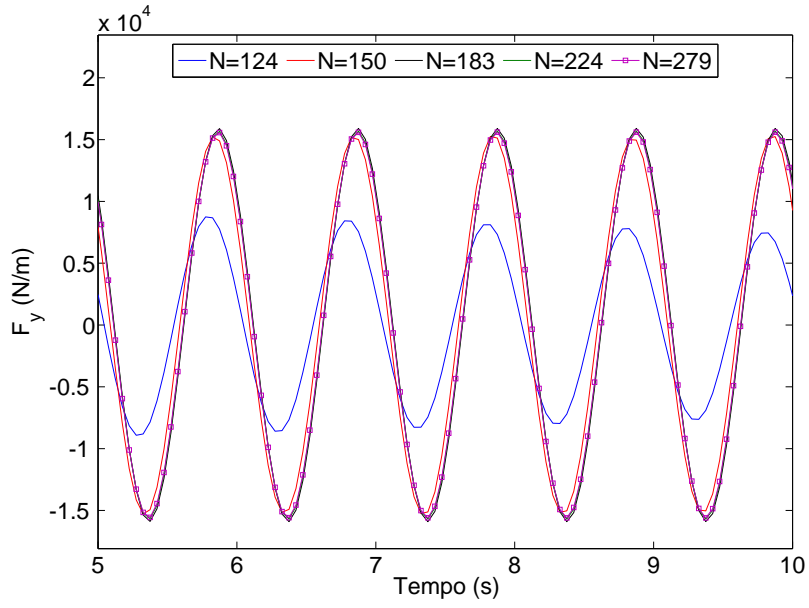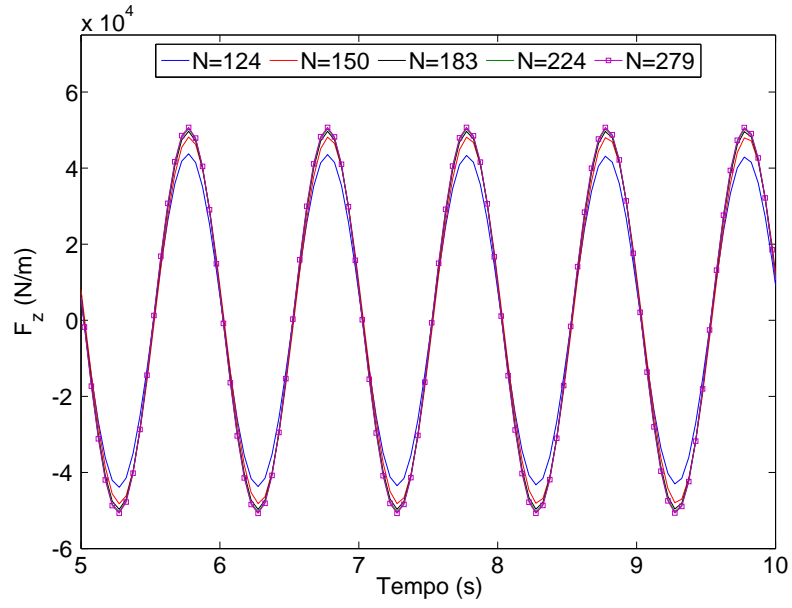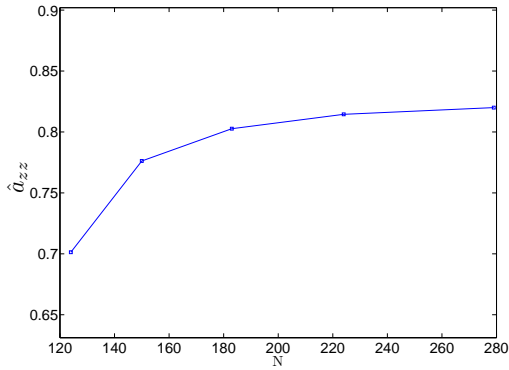
(a)
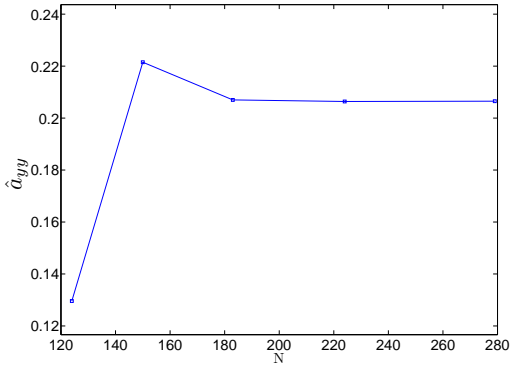
(b)
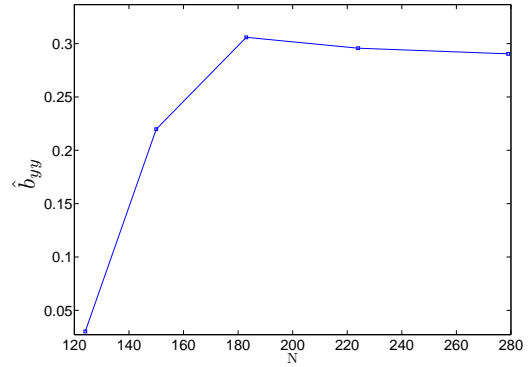
(c)

Figure 5.13: Circular section. (a) Time series of hydrodynamic force per length F_y; Convergence of (b) Added mass coefficient for swaying $\hat{a}_{yy}$ and (c) Potential damping for swaying $\hat{b}_{yy}$ as function of the panel number N, for dimensionless frequency $\hat{\omega} = 2.00$.

Table 5.6: Convergence analysis for swaying for the dimensionless frequency $\hat{\omega} = 2.00$ for the circular section
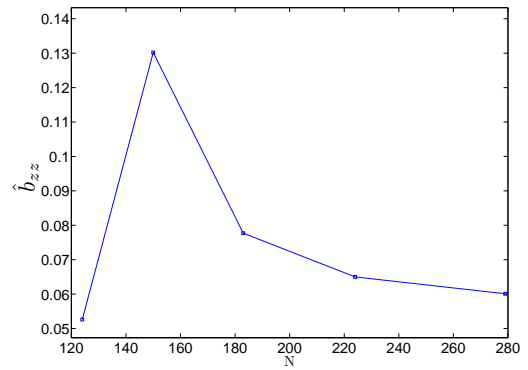
| Number of panels	$\hat{a}_{yy}$	$\hat{b}_{yy}$
124	0.130	0.030
150	0.222	0.220
183	0.207	0.306
224	0.206	0.296
279	0.206	0.290

(a)

(b)

(c)

Figure 5.14: Circular section. (a) Time series of hydrodynamic force per length F_z; Convergence of (b) Added mass coefficient for heaving $\hat{a}_{zz}$ and (c) Potential damping for heaving $\hat{b}_{zz}$ as function of the panel number N, for dimensionless frequency $\hat{\omega} = 2.00$.

Table 5.7: Convergence analysis for heaving for the dimensionless frequency $\hat{\omega} = 2.00$ for the circular section
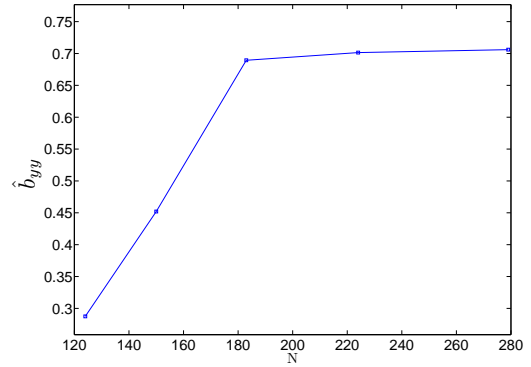
| Number of panels	$\hat{a}_{zz}$	$\hat{b}_{zz}$
124	0.701	0.053
150	0.776	0.130
183	0.803	0.078
224	0.815	0.065
279	0.820	0.060
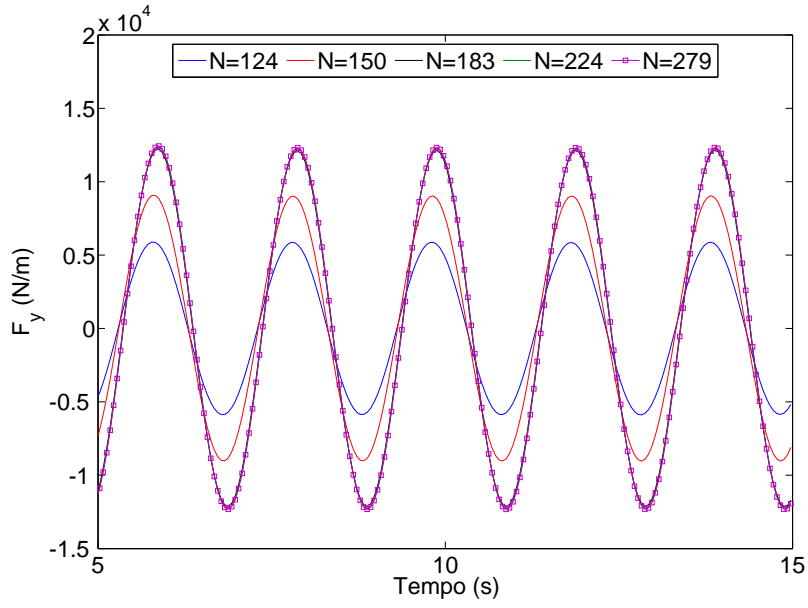
(a)
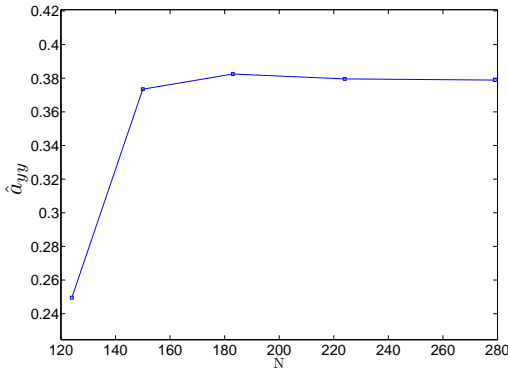
(b)

(c)

Figure 5.15: Circular section. (a) Time series of hydrodynamic force per length F_y; Convergence of (b) Added mass coefficient for swaying $\hat{a}_{yy}$ and (c) Potential damping for swaying $\hat{b}_{yy}$ as function of the panel number N, for dimensionless frequency $\hat{\omega} = 1.00$.

Table 5.8: Convergence analysis for swaying for the dimensionless frequency $\hat{\omega} = 1.00$ for the circular section
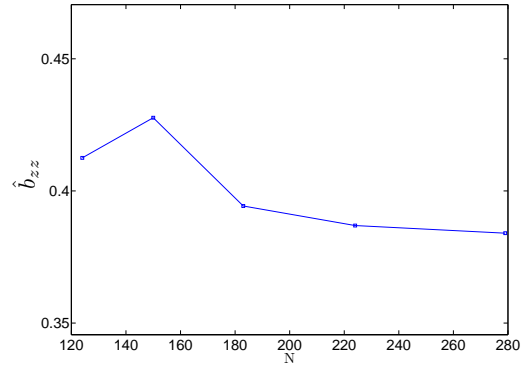
| Number of panels	$\hat{a}_{yy}$	$\hat{b}_{yy}$
124	0.250	0.288
150	0.374	0.452
183	0.383	0.689
224	0.380	0.701
279	0.379	0.706
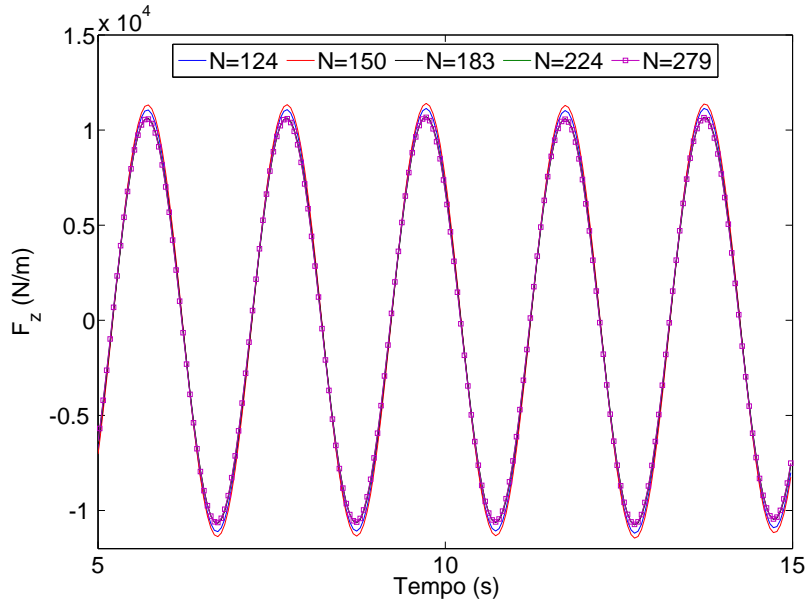
(a)
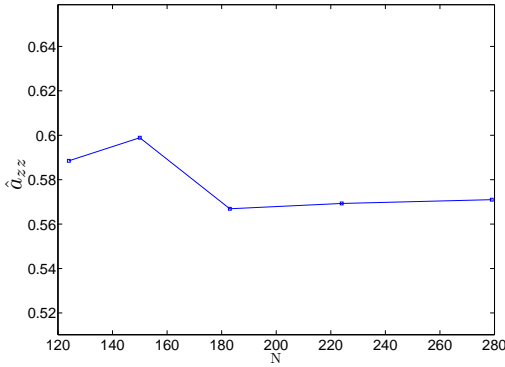
(b)

(c)

Figure 5.16: Circular section. (a) Time series of hydrodynamic force per length F_y; Convergence of (b) Added mass coefficient for heaving $\hat{a}_{zz}$ and (c) Potential damping for heaving $\hat{b}_{zz}$ as function of the panel number N, for dimensionless frequency $\hat{\omega} = 1.00$.

Table 5.9: Convergence analysis for heaving for the dimensionless frequency $\hat{\omega} = 1.00$ for the circular section
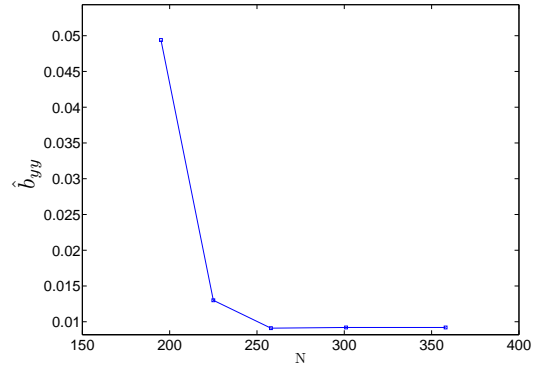
Number of panels	$\hat{a}_{zz}$	$\hat{b}_{zz}$
124	0.589	0.413
150	0.599	0.423
183	0.567	0.394
224	0.569	0.387
279	0.571	0.384
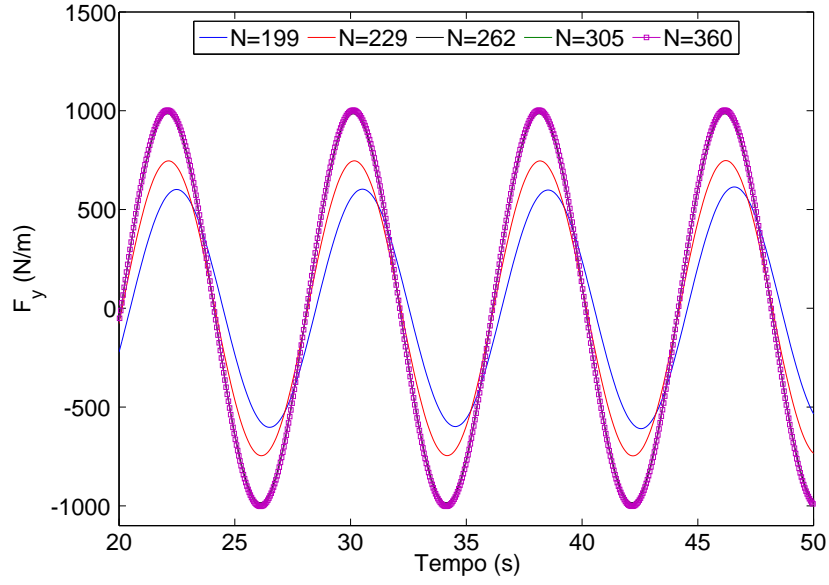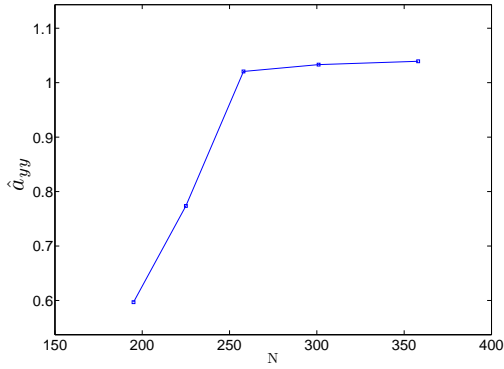
Figure 5.17: Circular section. (a) Time series of hydrodynamic force per length F_y; Convergence of (b) Added mass coefficient for swaying $\hat{a}_{yy}$ and (c) Potential damping for swaying $\hat{b}_{yy}$ as function of the panel number N, for dimensionless frequency $\hat{\omega} = 0.25$.

Table 5.10: Convergence analysis for swaying for the dimensionless frequency $\hat{\omega} = 0.25$ for the circular section

Number of panels	$\hat{a}_{yy}$	$\hat{b}_{yy}$
195	0.597	0.050
225	0.774	0.013
258	1.021	0.009
301	1.033	0.009
358	1.034	0.009

(a)

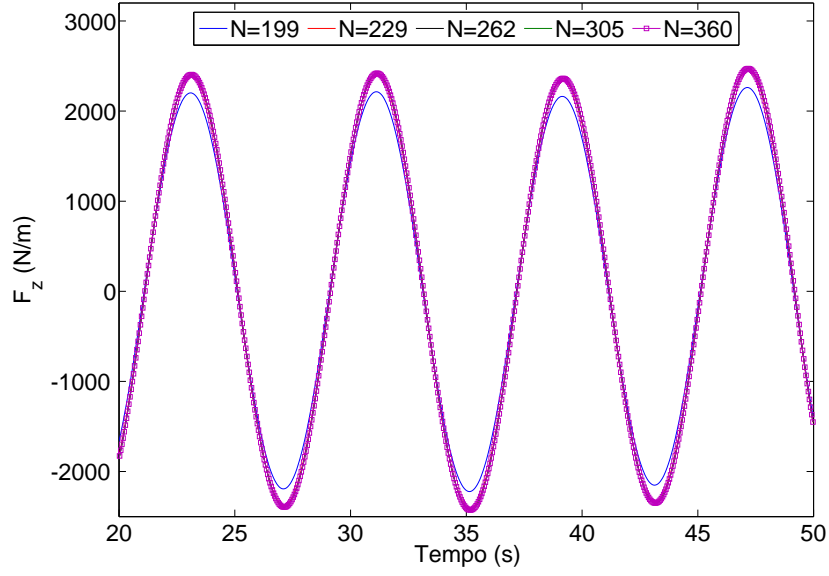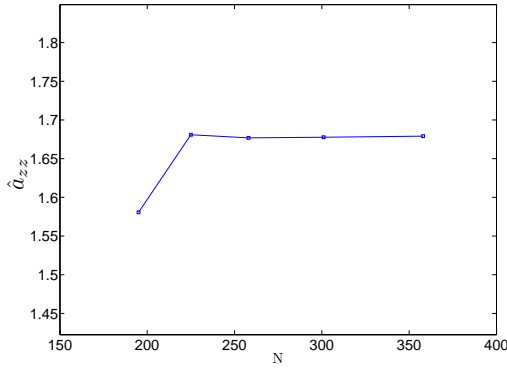(b)   (c)

Figure 5.18: Circular section. (a) Time series of hydrodynamic force per length F_z; Convergence of (b) Added mass coefficient for heaving $\hat{a}_{zz}$ and (c) Potential damping for heaving $\hat{b}_{zz}$ as function of the panel number N, for dimensionless frequency $\hat{\omega} = 0.25$.

Table 5.11: Convergence analysis for heaving for the dimensionless frequency $\hat{\omega} = 0.25$ for the circular section
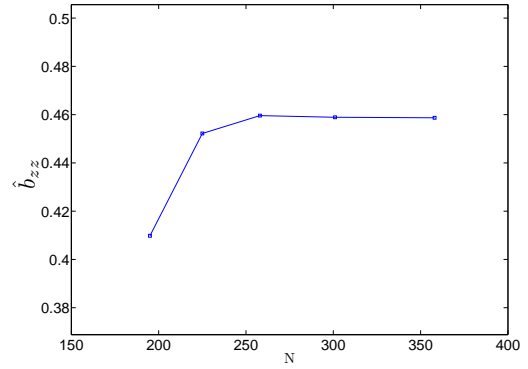
Number of panels	$\hat{a}_{zz}$	$\hat{b}_{zz}$
124	1.581	0.410
150	1.681	0.452
183	1.677	0.460
224	1.678	0.459
279	1.679	0.459

Following a similar convergence procedure, the results for added mass and potential damping coefficients in sway could be evaluated for a wider range of frequencies, as can be seen in Table

(5.12) and Table (5.13), respectively, with the data plotted in (5.19) and (5.20) in order to better visualize the results. It can be seen that the results of the present method BEM-2D (2011), Pesce [1988], Vugts [1968] and van Daalen [1993] agree very well for the added mass and potential damping coefficients, except the results of van Daalen [1993] for low frequencies. Regarding these discrepancies, it should be noticed that since he used a time domain fully non linear method, the numerical scheme had a very high computational cost (specially in 1993), which probably made the long time simulation on large domains unfeasible.

Table 5.12: Added mass coefficient for circular section in sway $\hat{a}_{yy}$

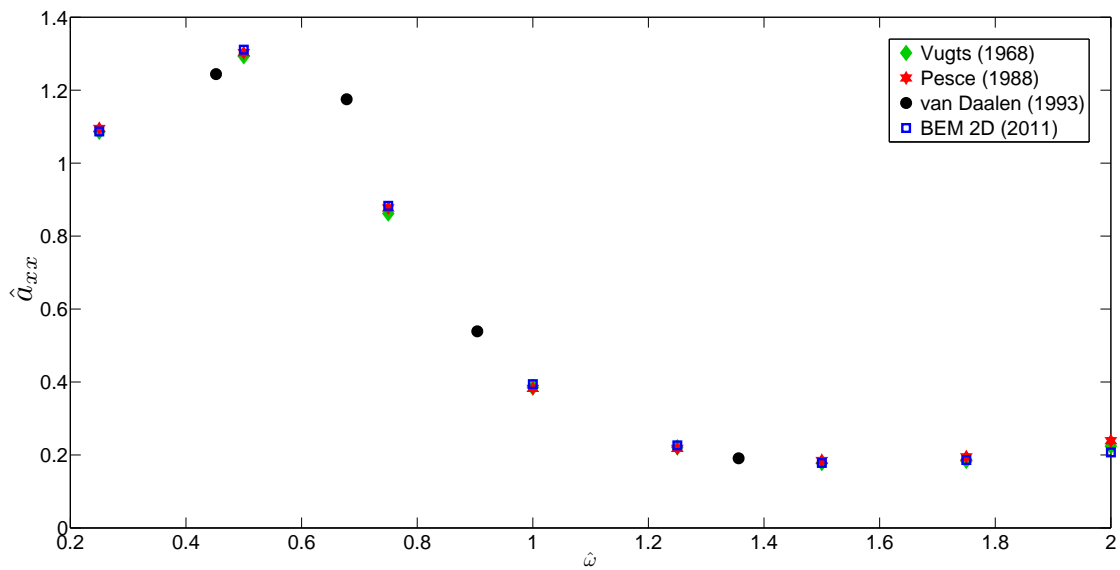| $\hat{\omega}$ | $\hat{a}_{yy}$ | | | |
	Vugts (1968)	Pesce (1988)	van Daalen (1993)	USP (2011)
0.250	1.086	1.095	—	1.087
0.452	—	—	1.244	—
0.500	1.293	1.303	—	1.311
0.677	—	—	1.175	—
0.750	0.862	0.877	—	0.883
0.903	—	—	0.539	—
1.000	0.385	0.383	—	0.394
1.250	0.221	0.218	—	0.226
1.355	—	—	0.191	—
1.500	0.178	0.185	—	0.178
1.750	0.184	0.195	—	0.186
2.000	0.224	0.239	—	0.207

Figure 5.19: Added mass for sway motion in sway direction of a circular cylinder

Table 5.13: Potential damping coefficient for circular section in sway $\hat{b}_{yy}$

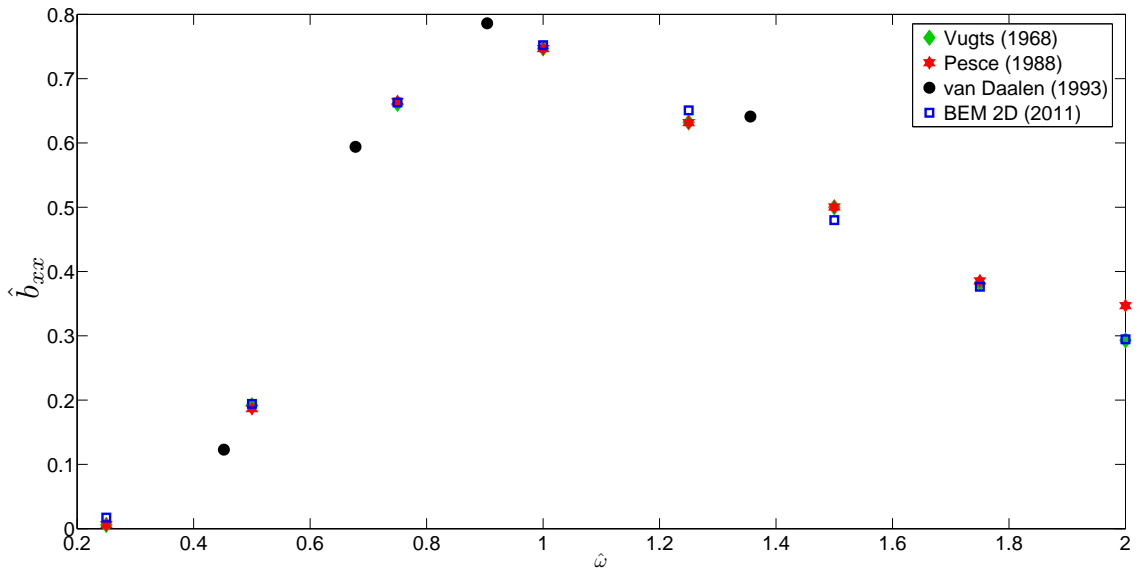| $\hat{\omega}$	$\hat{b}_{yy}$			
	Vugts (1968)	Pesce (1988)	van Daalen (1993)	USP (2011)
0.250	0.006	0.006	–	0.017
0.452	–	–	0.123	–
0.500	0.192	0.187	–	0.194
0.677	–	–	0.594	–
0.750	0.661	0.664	–	0.663
0.903	–	–	0.786	–
1.000	0.747	0.747	–	0.752
1.250	0.632	0.632	–	0.651
1.355	–	–	0.641	–
1.500	0.500	0.500	–	0.480
1.750	0.382	0.386	–	0.376
2.000	0.293	0.347	–	0.295

Figure 5.20: Potential damping for sway motion in sway direction of a circular cylinder

The results for added mass and potential damping coefficient for the heave motion can be seen in Tables (5.14) and (5.15), being the results plotted in Figures (5.21) and (5.22). The conclusions were very similar to those concerning the sway motion analysis.

91

Table 5.14: Added mass coefficient for circular section in heave $\hat{a}_{zz}$

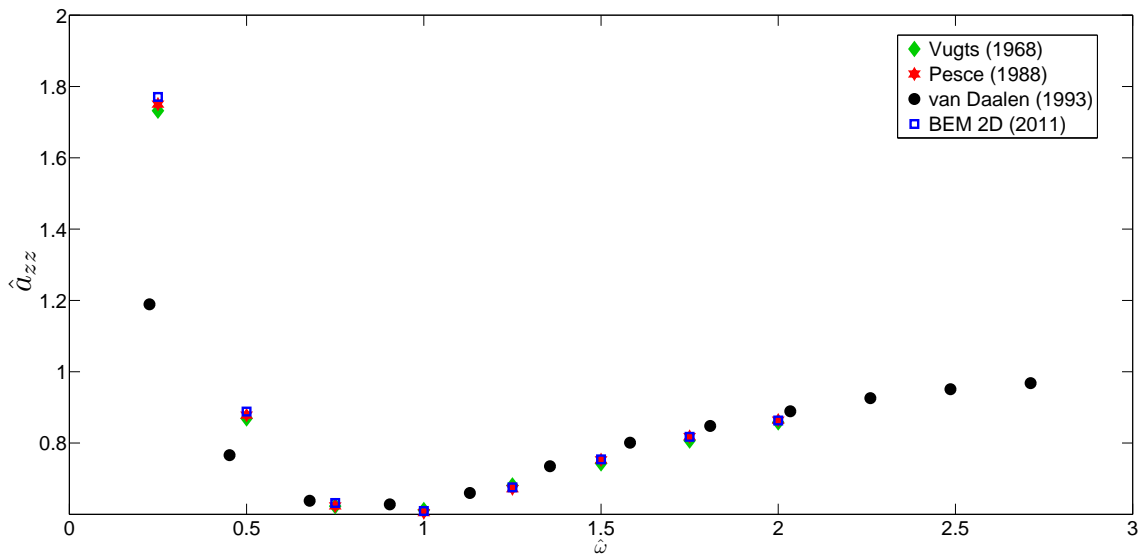| $\hat{\omega}$ | $\hat{a}_{zz}$ | | | |
	Vugts (1968)	Pesce (1988)	van Daalen (1993)	BEM-2D (2011)
0.226	–	–	1.189	–
0.250	1.732	1.751	–	1.771
0.452	–	–	0.766	–
0.500	0.869	0.879	–	0.888
0.677	–	–	0.638	–
0.750	0.623	0.624	–	0.632
0.903	–	–	0.628	–
1.000	0.612	0.605	–	0.610
1.250	0.681	0.672	–	0.676
1.129	–	–	0.660	–
1.355	–	–	0.735	–
1.500	0.743	0.753	–	0.754
1.580	–	–	0.801	–
1.750	0.807	0.818	–	0.817
1.806	–	–	0.848	–
2.000	0.858	0.864	–	0.863

Figure 5.21: Added mass for heave motion in heave direction of a circular cylinder

Table 5.15: Potential damping coefficient for circular section in heave $\hat{b}_{zz}$

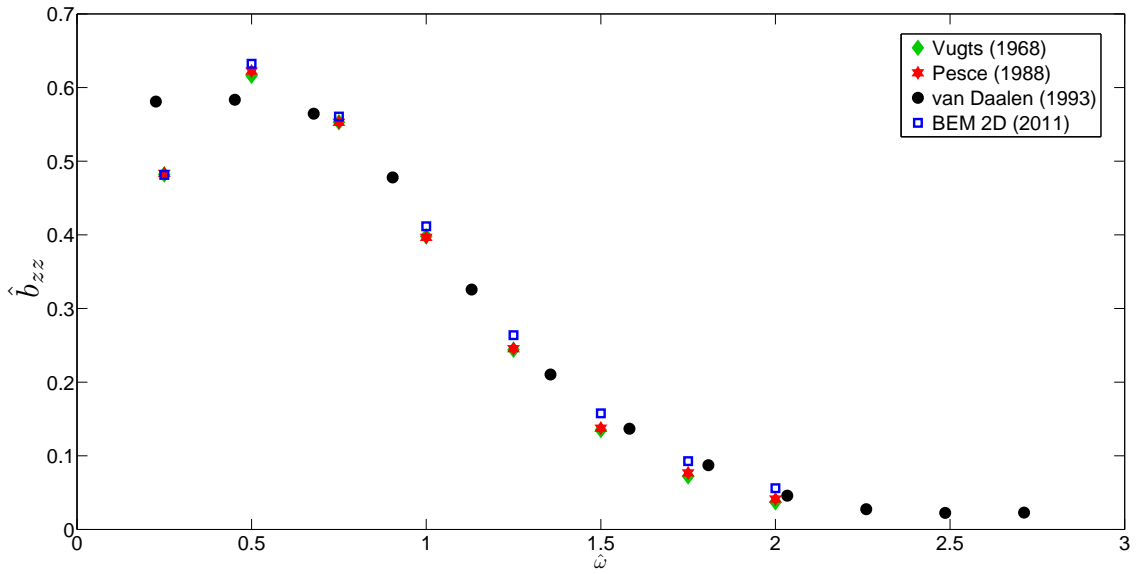| $\hat{\omega}$ | $\hat{b}_{zz}$ | | | |
	Vugts (1968)	Pesce (1988)	van Daalen (1993)	BEM-2D (2011)
0.226	–	–	0.581	–
0.250	0.482	0.484	–	0.481
0.452	–	–	0.584	–
0.500	0.616	0.622	–	0.632
0.677	–	–	0.565	–
0.750	0.553	0.553	–	0.561
0.903	–	–	0.478	–
1.000	0.398	0.397	–	0.412
1.250	0.244	0.245	–	0.264
1.129	–	–	0.326	–
1.355	–	–	0.211	–
1.500	0.135	0.138	–	0.158
1.580	–	–	0.137	–
1.750	0.072	0.077	–	0.093
1.806	–	–	0.087	–
2.000	0.037	0.041	–	0.056

Figure 5.22: Potential damping for heave motion in heave direction of a circular cylinder

5.2.2 Rectangular section cylinder

For the rectangular cylinder a similar procedure was adopted, with the dimensionless calculations given by (5.27) and the arrangement considering a box with breadth of 6.4m and draft of 0.8m, illustrated in Figure (5.23).
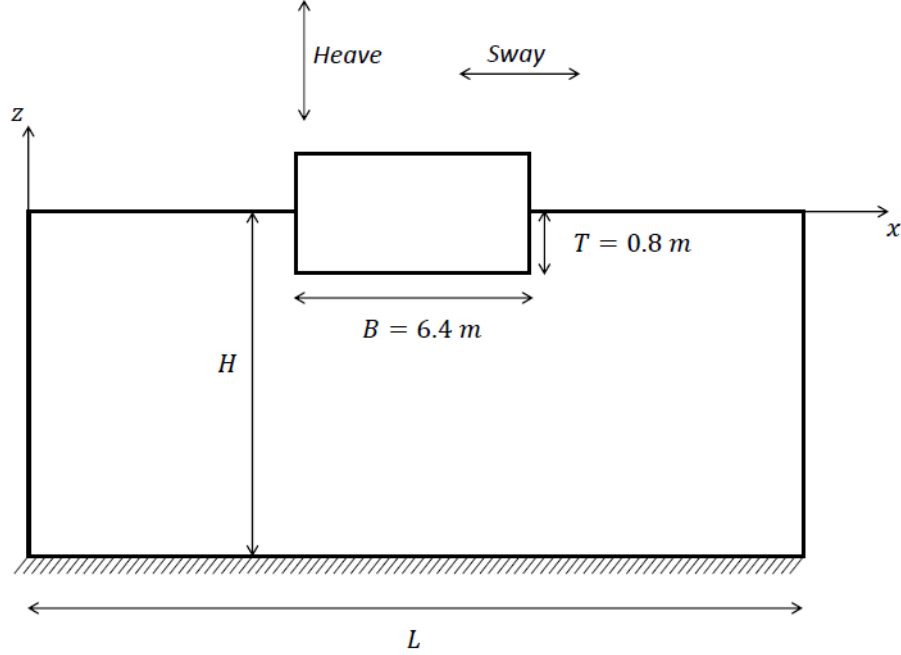

Figure 5.23: Rectangular section forced oscillation test

The numerical results of the present method were compared to the results of Pesce [1988], Vugts [1968] and with the analytical solution of Black et al. [1971], as reproduced by Zheng et al. [2004]. The analytic solution is built by an eigenvector expansion similar to the one developed for the wave-maker but with 3 different regions. This solution requires some compatibility conditions that avoid pressure or velocity jumps betweens the regions. The analytical results presented were obtained considering the first 30 terms of the series.

$$\hat{\omega} = \omega\sqrt{\frac{B}{g}}, \quad \hat{a}_{xx} = \frac{a_{xx}}{\rho\forall}, \quad \hat{b}_{xx} = \frac{b_{xx}}{\rho\forall}\sqrt{\frac{B}{2g}}, \quad \hat{a}_{zz} = \frac{a_{zz}}{\rho\forall}, \quad \hat{b}_{zz} = \frac{b_{zz}}{\rho\forall}\sqrt{\frac{B}{2g}} \qquad (5.27)$$

Following the same analysis procedure adopted for the circular cylinder, the results for swaying and heaving test were obtained and are presented next. The depth influence and discretization convergence analyse were similar to the one applied for the circular section. The determination of depth influence in the added mass and potential damping can be seen in

Figures (5.24), (5.25) and (5.26), for the same dimensionless frequencies $\hat{\omega} = 2.00$, $\hat{\omega} = 1.00$ and $\hat{\omega} = 0.25$.
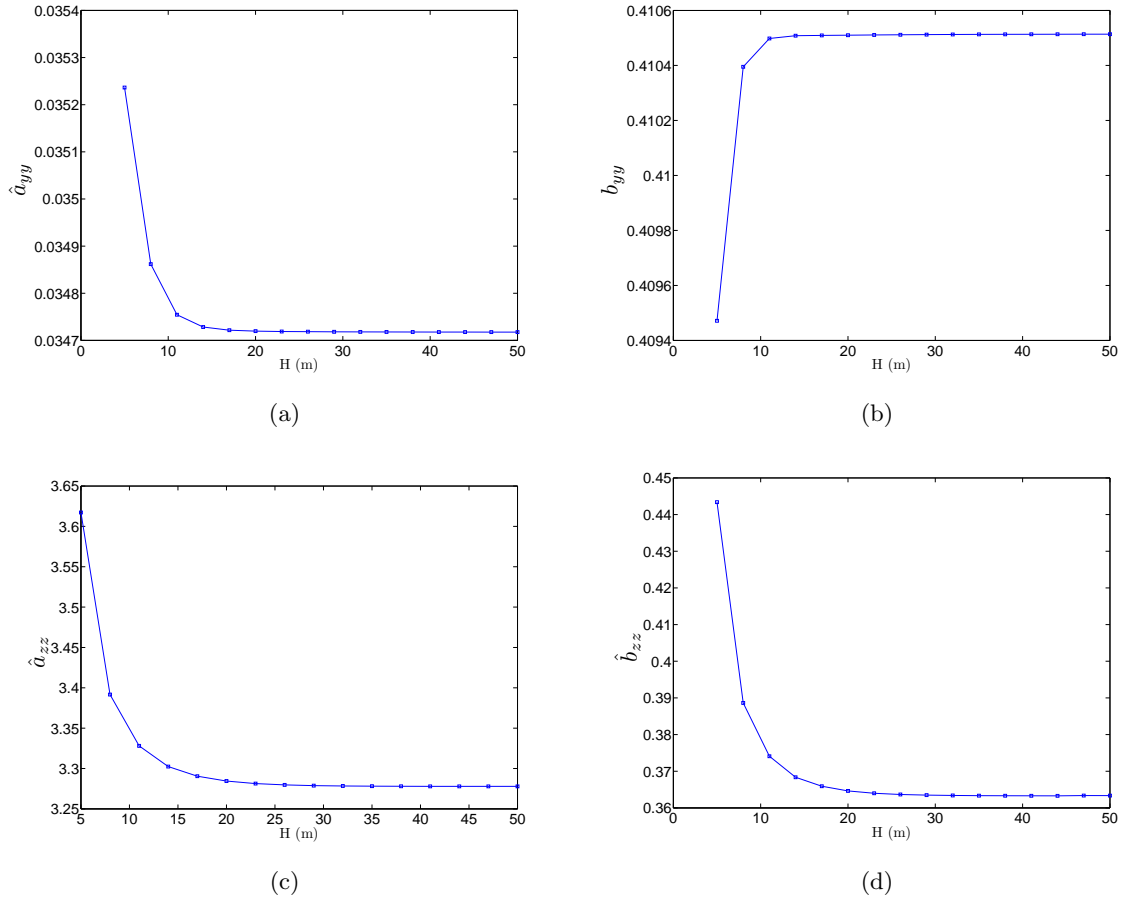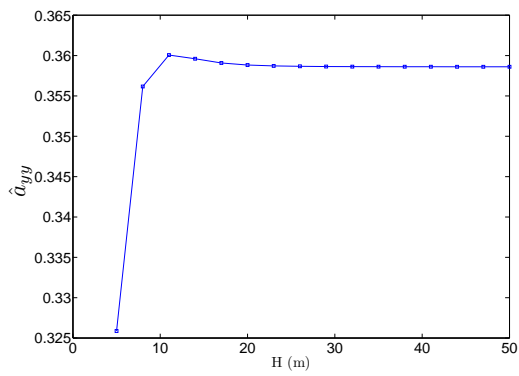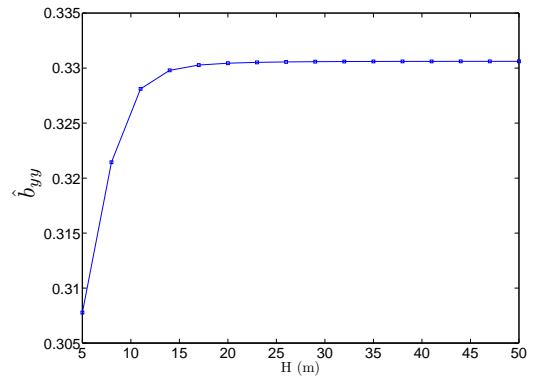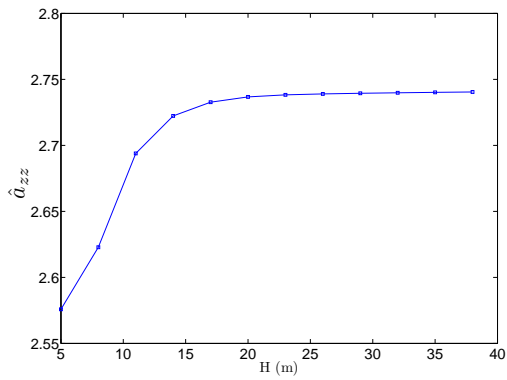

(a)

(b)

(c)

(d)

Figure 5.24: Variation of added mass ($\hat{a}_{yy}$, $\hat{a}_{zz}$) and potential damping ($\hat{b}_{yy}$, $\hat{b}_{zz}$) coefficients changing depth H for the dimensionless frequency $\hat{\omega} = 2.00$ for the rectangular section.

Figure 5.25: Variation of added mass ($\hat{a}_{yy}$, $\hat{a}_{zz}$) and potential damping ($\hat{b}_{yy}$, $\hat{b}_{zz}$) coefficients changing depth H for the dimensionless frequency $\hat{\omega} = 1$ for the rectangular section.

Figure 5.26: Variation of added mass ($\hat{a}_{yy}$, $\hat{a}_{zz}$) and potential damping ($\hat{b}_{yy}$, $\hat{b}_{zz}$) coefficients changing depth H for the dimensionless frequency $\hat{\omega} = 0.25$ for the rectangular section.
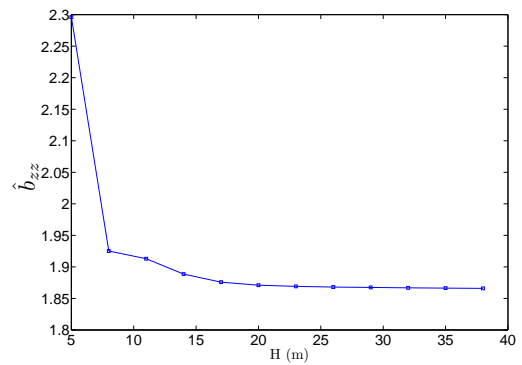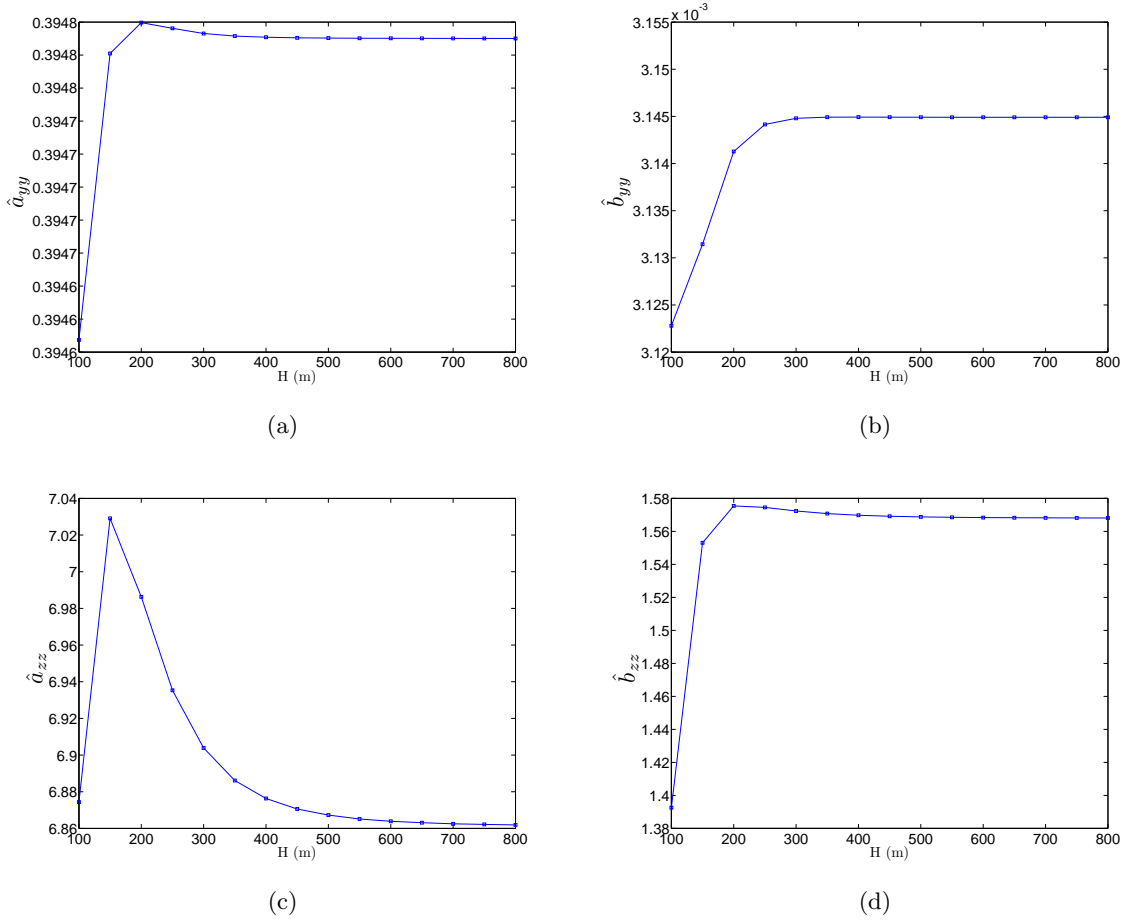
This study defined the domain dimensions as given in Table (5.16). The meshes were also created using stretching ranging the minimum panel size from 0.05m up to 0.8m, providing meshes with the number of panels given in Table (5.17).

Table 5.16: Domain size for forced oscillation test of a rectangular section

$\hat{\omega}$	L (m)	H (m)
2.00	60	20
1.00	140	20
0.25	1600	600

Table 5.17: Stretched meshes tested for numerical forced oscillation test of a rectangular section

$\hat{\omega}$	N_1	N_2	N_3	N_4	N_5
2.00	165	199	241	304	408
1.00	163	196	241	305	412
0.25	269	305	350	419	526

The discretization convergence tests can be seen in Figures (5.27), (5.28), (5.29), (5.30),

(5.31) and (5.32), with the hydrodynamic forces, added mass and potential damping coefficients presented for sway and heave motions. It can be seen that the convergence is easier for this kind of geometry, since the results almost do not change by increasing the panel number.
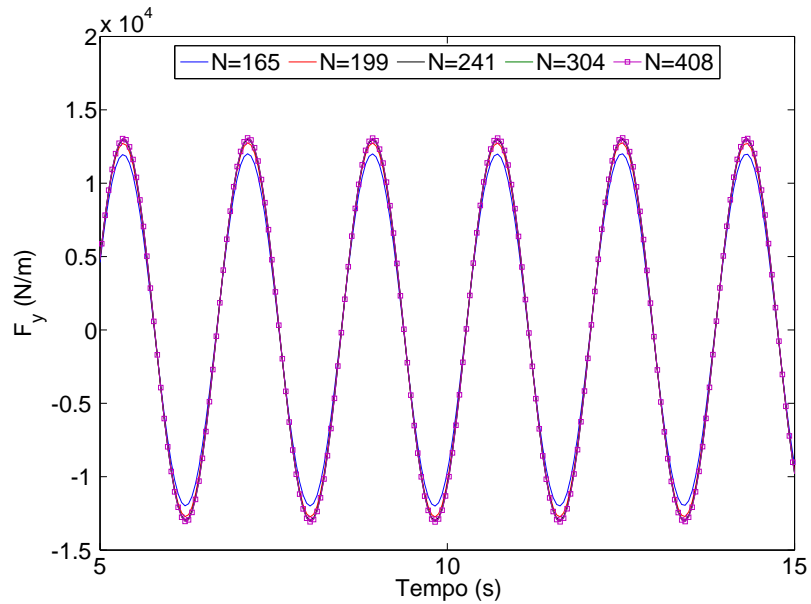
(a)
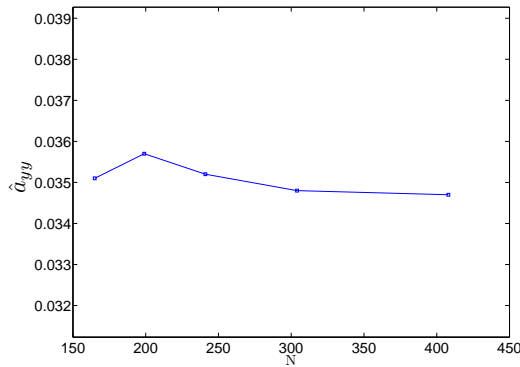
(b)
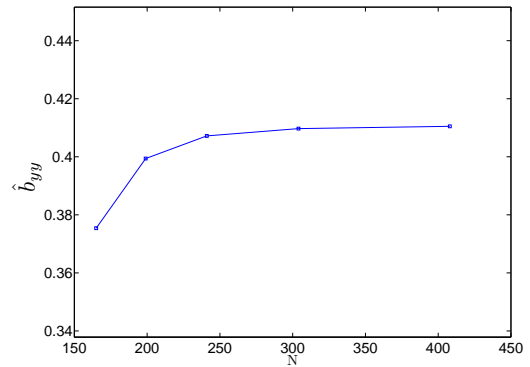
(c)

Figure 5.27: Rectangular section. (a) Time series of hydrodynamic force per length F_y; Convergence of (b) Added mass coefficient for swaying $\hat{a}_{yy}$ and (c) Potential damping for swaying $\hat{b}_{yy}$ as function of the panel number N, for dimensionless frequency $\hat{\omega} = 2.00$.

Table 5.18: Convergence analysis for swaying for the dimensionless frequency $\hat{\omega} = 2.00$ for the rectangular section

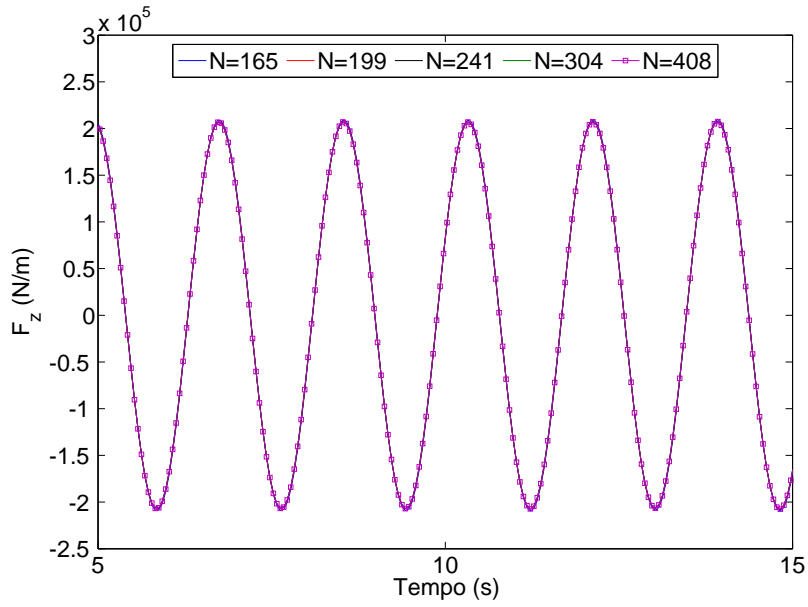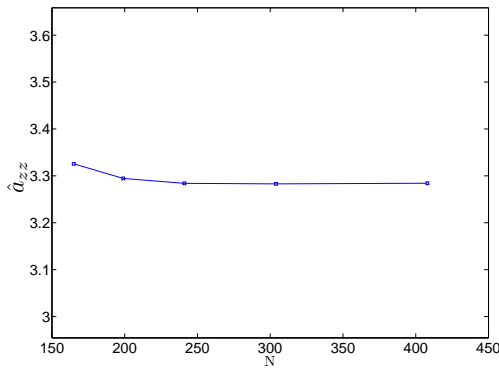| Number of panels	$\hat{a}_{yy}$	$\hat{b}_{yy}$
165	0.035	0.375
199	0.036	0.399
241	0.035	0.407
304	0.035	0.410
408	0.035	0.411

(a)

(b)
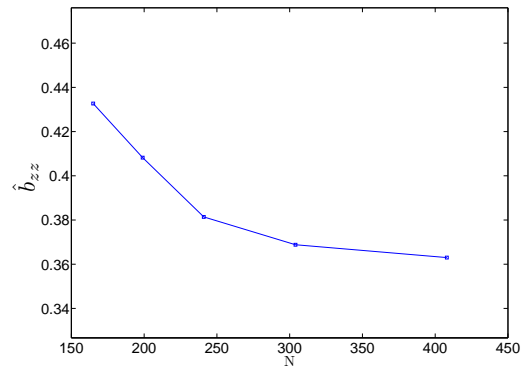
(c)

Figure 5.28: Rectangular section. (a) Time series of hydrodynamic force per length F_z; Convergence of (b) Added mass coefficient for heaving $\hat{a}_{zz}$ and (c) Potential damping for heaving $\hat{b}_{zz}$ as function of the panel number N, for dimensionless frequency $\hat{\omega} = 2.00$.

Table 5.19: Convergence analysis for heaving for the dimensionless frequency $\hat{\omega} = 2.00$ for the rectangular section

Number of panels	$\hat{a}_{zz}$	$\hat{b}_{zz}$
165	3.326	0.433
199	3.295	0.402
241	3.284	0.381
304	3.283	0.367
408	3.284	0.363

(a)

(b)
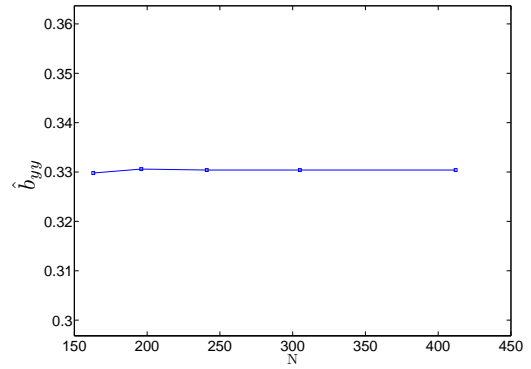
(c)

Figure 5.29: Rectangular section. (a) Time series of hydrodynamic force per length F_y; Convergence of (b) Added mass coefficient for swaying $\hat{a}_{yy}$ and (c) Potential damping for swaying $\hat{b}_{yy}$ as function of the panel number N, for dimensionless frequency $\hat{\omega} = 1.00$.

Table 5.20: Convergence analysis for swaying for the dimensionless frequency $\hat{\omega} = 1.00$ for the rectangular section

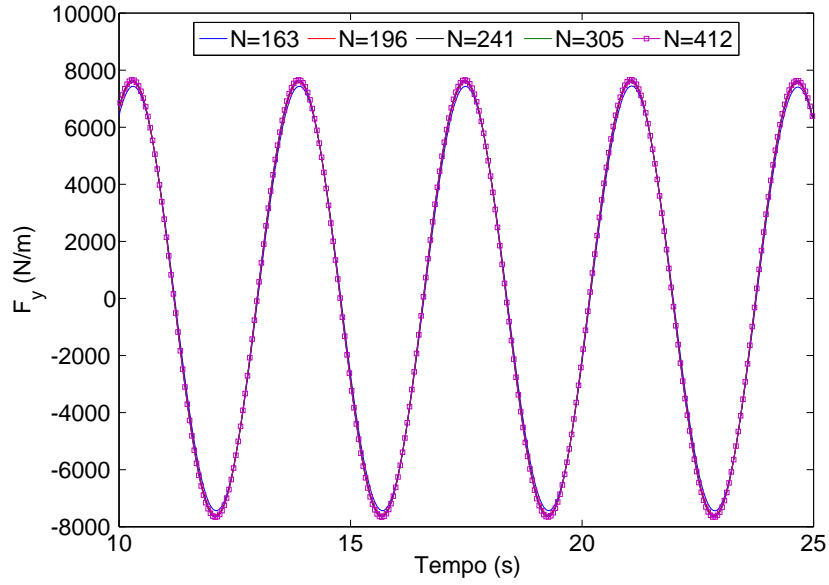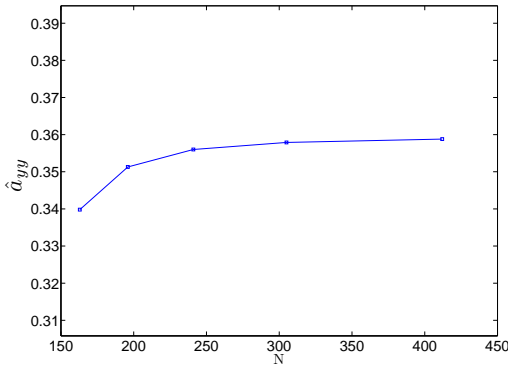| Number of panels	$\hat{a}_{yy}$	$\hat{b}_{yy}$
163	0.340	0.330
196	0.351	0.331
241	0.356	0.330
305	0.358	0.330
412	0.359	0.330

(a)

(b)
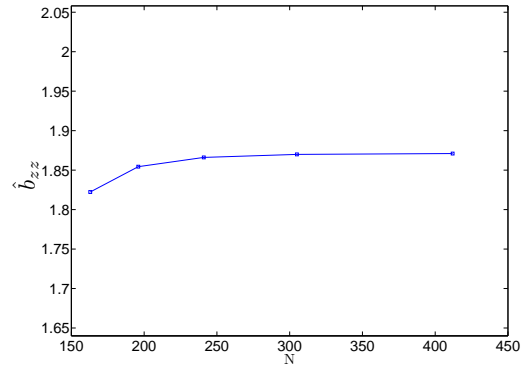
(c)

Figure 5.30: Rectangular section. (a) Time series of hydrodynamic force per length F_z; Convergence of (b) Added mass coefficient for heaving $\hat{a}_{zz}$ and (c) Potential damping for heaving $\hat{b}_{zz}$ as function of the panel number N, for dimensionless frequency $\hat{\omega} = 1.00$.

Table 5.21: Convergence analysis for heaving for the dimensionless frequency $\hat{\omega} = 1.00$ for the rectangular section

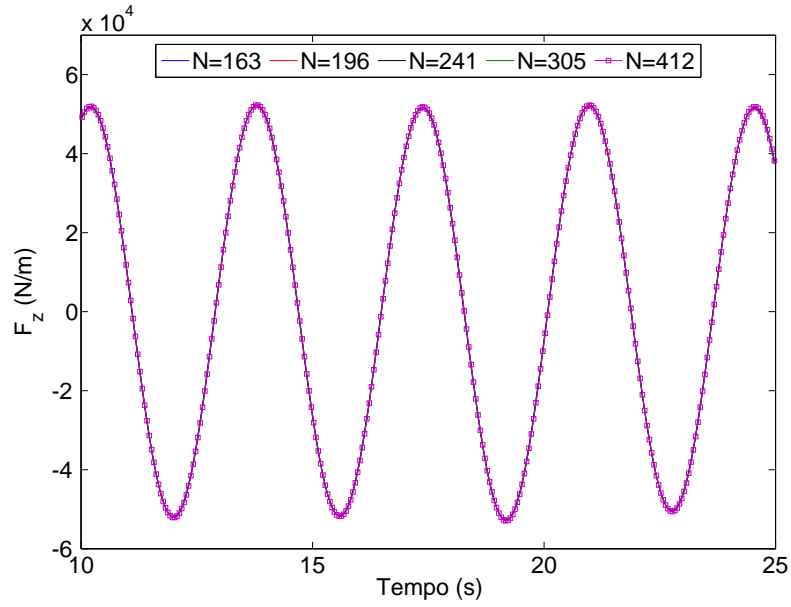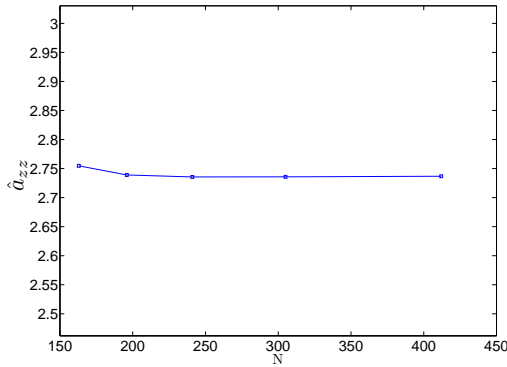| Number of panels	$\hat{a}_{zz}$	$\hat{b}_{zz}$
163	2.755	1.822
196	2.739	1.854
241	2.736	1.866
305	2.734	1.870
412	2.734	1.871
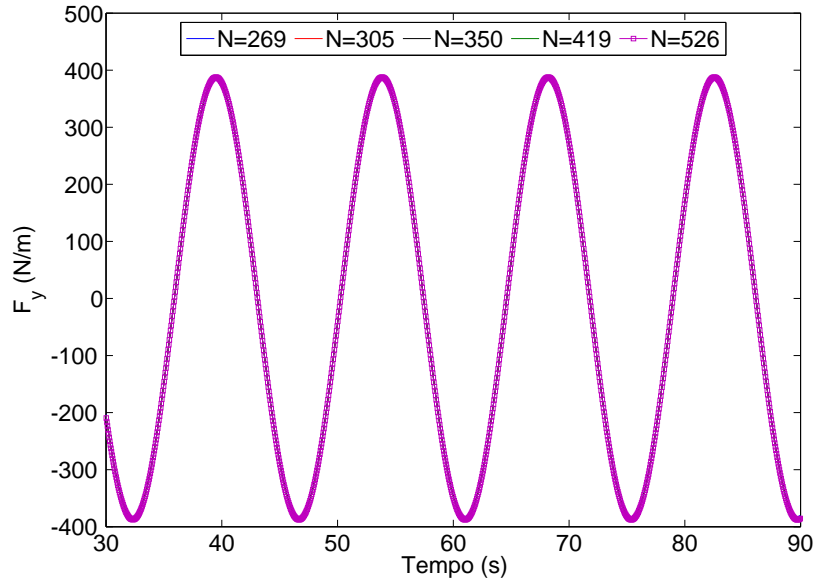
(a)
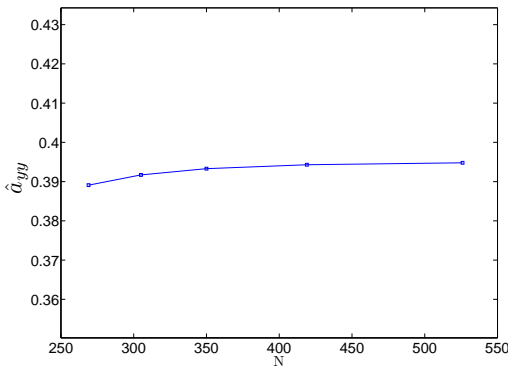
(b)
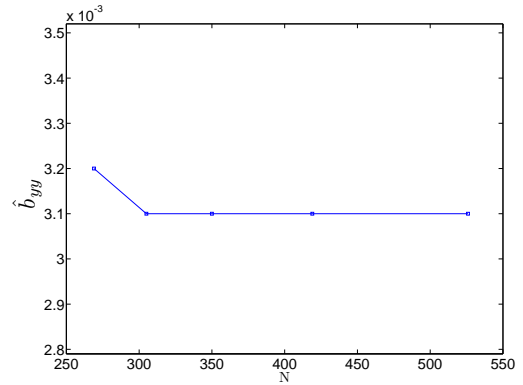
(c)

Figure 5.31: Rectangular section. (a) Time series of hydrodynamic force per length F_y; Convergence of (b) Added mass coefficient for swaying $\hat{a}_{yy}$ and (c) Potential damping for swaying $\hat{b}_{yy}$ as function of the panel number N, for dimensionless frequency $\hat{\omega} = 0.25$.

Table 5.22: Convergence analysis for swaying for the dimensionless frequency $\hat{\omega} = 0.25$ for the rectangular section

Number of panels	$\hat{a}_{yy}$	$\hat{b}_{yy}$
269	0.389	0.003
305	0.392	0.003
350	0.393	0.003
419	0.394	0.003
526	0.395	0.003

(a)

(b)
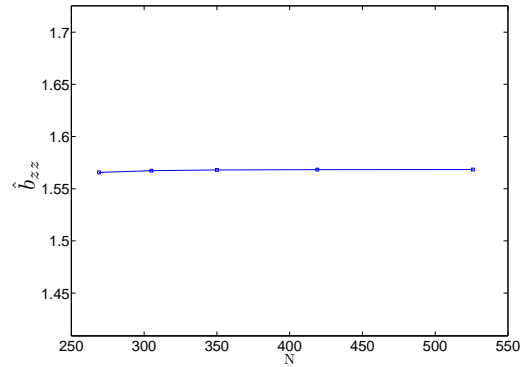
(c)

Figure 5.32: Rectangular section. (a) Time series of hydrodynamic force per length F_z; Convergence of (b) Added mass coefficient for heaving $\hat{a}_{zz}$ and (c) Potential damping for heaving $\hat{b}_{zz}$ as function of the panel number N, for dimensionless frequency $\hat{\omega} = 0.25$.

Table 5.23: Convergence analysis for heaving for the dimensionless frequency $\hat{\omega} = 0.25$ for the rectangular section
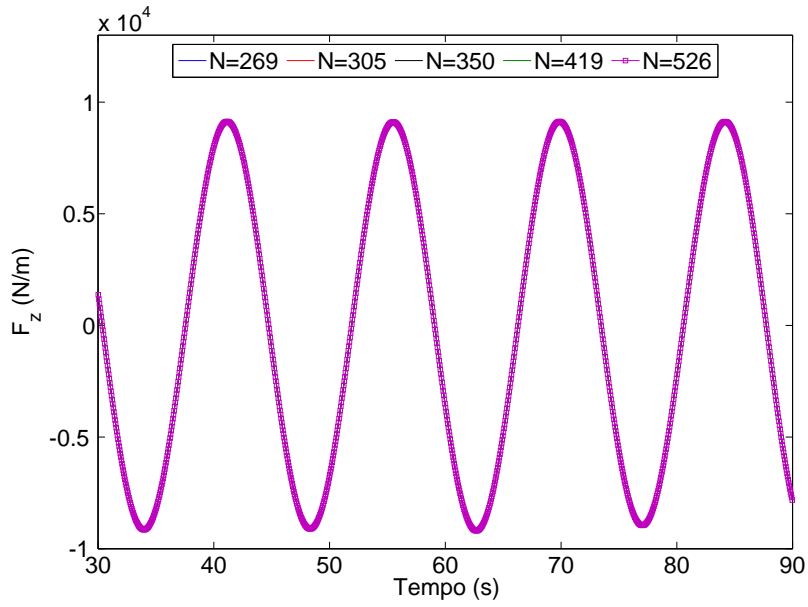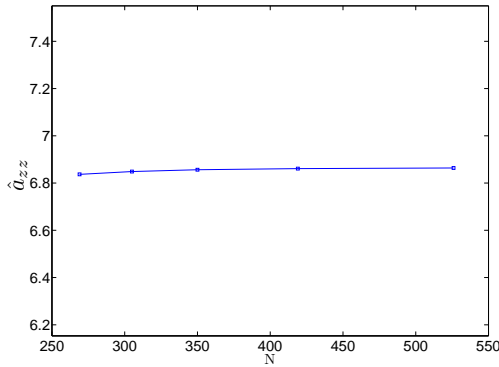
Number of panels	$\hat{a}_{zz}$	$\hat{b}_{zz}$
269	6.837	1.566
305	6.845	1.567
350	6.856	1.568
419	6.861	1.568
526	6.864	1.568

From this convergence analysis, the number of panels chosen for the dimensionless frequencies $\hat{\omega} = 2.00$, $\hat{\omega} = 1.00$ and $\hat{\omega} = 0.25$ was 408, 241 and 305 panels, respectively. The results for swaying of the rectangular section can be seen in Tables (5.24) and (5.25) and plotted in Figures (5.33) and (5.34). It can be seen that the agreement between results is very good and in terms of engineering the differences would be negligible. The results for swaying can be seen on Tables (5.24) and (5.25) and to better visualize they are plotted on Figures (5.33) and (5.34). It can be seen that the agreement between all results are very good, and the differences between the present results and the analytical solution could be considered negligible from an engineering point of view.

Table 5.24: Added mass coefficient for rectangular section in sway $\hat{a}_{yy}$

$\hat{\omega}$	Vugts (1968)	Pesce (1988)	Black and Mei (1971) Zheng (2004)	BEM-2D (2011)
0.250	0.390	0.357	0.390	0.388
0.500	0.430	0.426	0.455	0.455
0.750	0.454	0.441	0.473	0.446
1.000	0.350	0.336	0.356	0.351
1.250	0.215	0.205	0.216	0.217
1.500	0.115	0.113	0.120	0.120
1.750	0.057	0.050	0.062	0.063
2.000	0.023	0.027	0.032	0.033
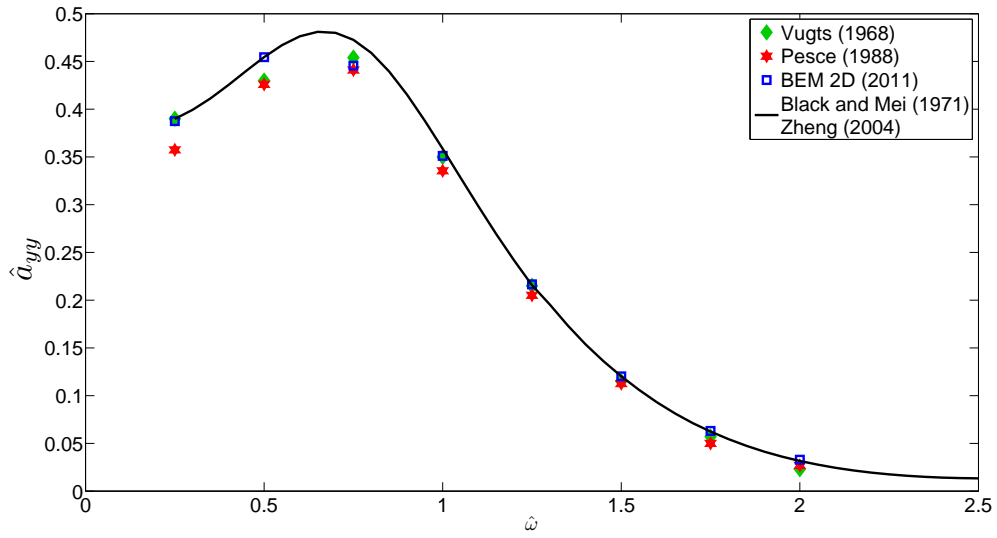
Figure 5.33: Added mass for sway motion in sway direction of a rectangular cylinder

Table 5.25: Potential damping coefficient for circular section in sway $\hat{b}_{yy}$

| $\hat{\omega}$ | $\hat{b}_{yy}$ | | | |
	Vugts (1968)	Pesce (1988)	Black and Mei (1971) Zheng (2004)	BEM-2D (2011)
0.250	0.000	0.001	0.001	0.005
0.500	0.026	0.026	0.027	0.031
0.750	0.150	0.142	0.152	0.160
1.000	0.318	0.307	0.330	0.325
1.250	0.428	0.407	0.438	0.429
1.500	0.448	0.428	0.463	0.458
1.750	0.440	0.428	0.447	0.444
2.000	0.405	0.396	0.411	0.409
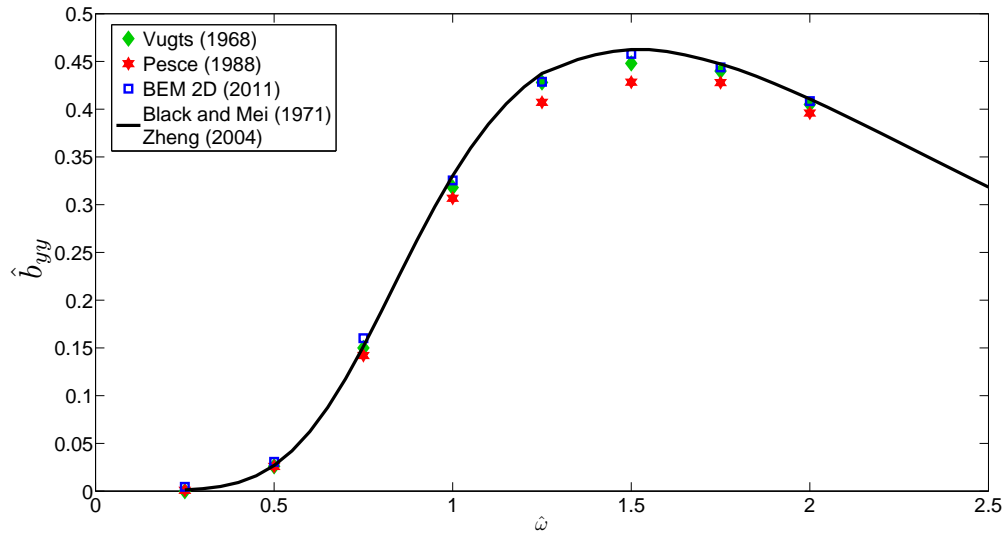
Figure 5.34: Potential damping for sway motion in sway direction of a rectangular cylinder

The results for heaving can be seen on Tables (5.26) and (5.27) and are plotted in Figures (5.35) and (5.36), it can be seen that the agreement is good for the heave motion too recovering the analytic solution very well.

Table 5.26: Added mass coefficient for rectangular section in heave $\hat{a}_{zz}$

|			$\hat{a}_{zz}$	
$\hat{\omega}$	Vugts (1968)	Pesce (1988)	Black and Mei (1971) Zheng (2004)	USP (2011)
0.250	–	6.895	6.994	6.790
0.500	4.080	4.080	4.129	4.060
0.750	3.045	3.066	3.104	3.070
1.000	2.736	2.706	2.753	2.735
1.250	2.701	2.672	2.743	2.738
1.500	2.816	2.802	2.919	2.895
1.750	3.046	2.992	3.172	3.100
2.000	3.218	3.176	3.386	3.288
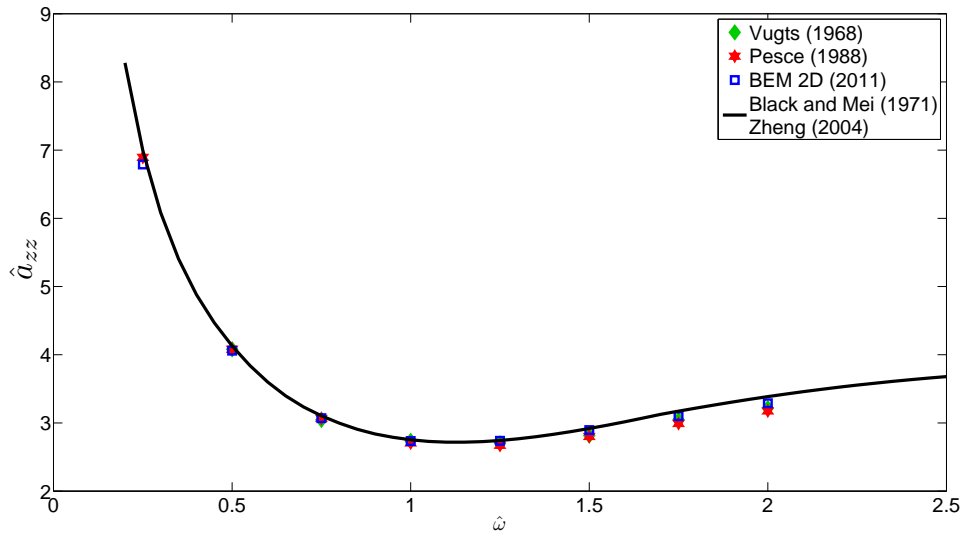
Figure 5.35: Added mass for heave motion in heave direction of a rectangular cylinder

Table 5.27: Potential damping coefficient for circular section in heave $\hat{b}_{zz}$

$\hat{\omega}$	Vugts (1968)	Pesce (1988)	$\hat{b}_{zz}$ Black and Mei (1971) Zheng (2004)	USP (2011)
0.250	1.550	1.556	1.550	1.540
0.500	2.155	2.161	2.144	2.140
0.750	2.195	2.203	2.167	2.170
1.000	1.908	1.922	1.868	1.866
1.250	1.465	1.477	1.414	1.433
1.500	0.975	1.012	0.956	0.974
1.750	0.590	0.626	0.590	0.602
2.000	0.330	0.356	0.341	0.349
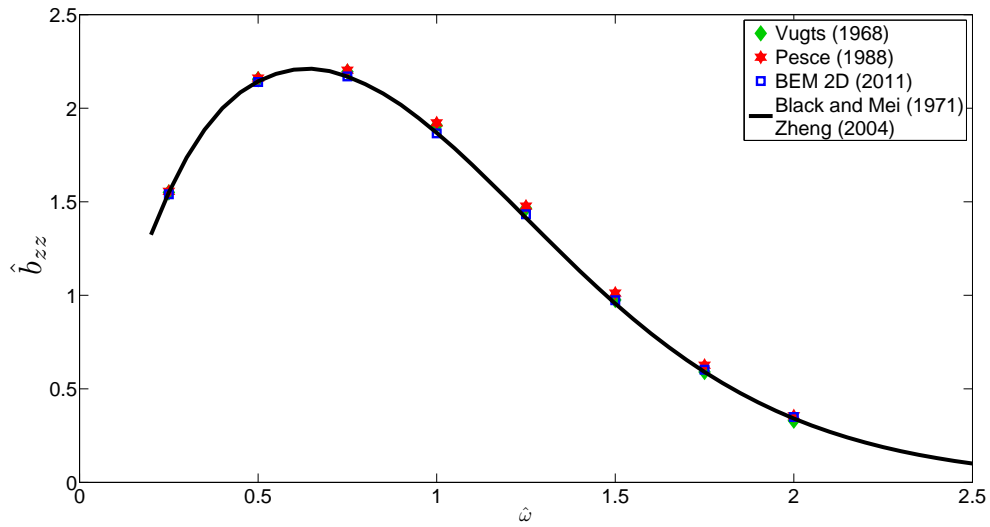
Figure 5.36: Potential damping for heave motion in heave direction of a rectangular cylinder

5.3   Decay tests

Until this point, none of the simulations performed requested the acceleration potential in order to guarantee the numerical stability, since the motion series is independent of the hydrodynamic forces. In order to verify the fluid-structure interaction capabilities for floating bodies, numerical decay test simulations were performed. The comparison was done for the circular and rectangular cylinders and the results were compared to the numerical results of van Daalen [1993]. Since his method is fully nonlinear, he presented the results for several initial displacements in order to verify the influence of non-linearities. The comparison was done taking only the lowest initial displacement in order to minimize the non-linear effects, although his conclusion was that the non linear effects were minimum, but for the roll decay test.

5.3.1 Circular cylinder

The circular section was the first one studied and a simulation considering the section at the middle of the numerical tank was performed. An illustrative picture is shown in Figure (5.37) and considers the center of gravity at the symmetry axis with coordinates (x_G, z_G). Initially the cylinder is at rest with the center of gravity at $(20, 0)m$ and then moved upside by an initial displacement of δz and released, irradiating waves (energy) and reducing it's motion amplitude. The simulation was performed until the motion amplitude becomes small, which does not take more than 5 cycles, as can be seen in (5.38), as an example.
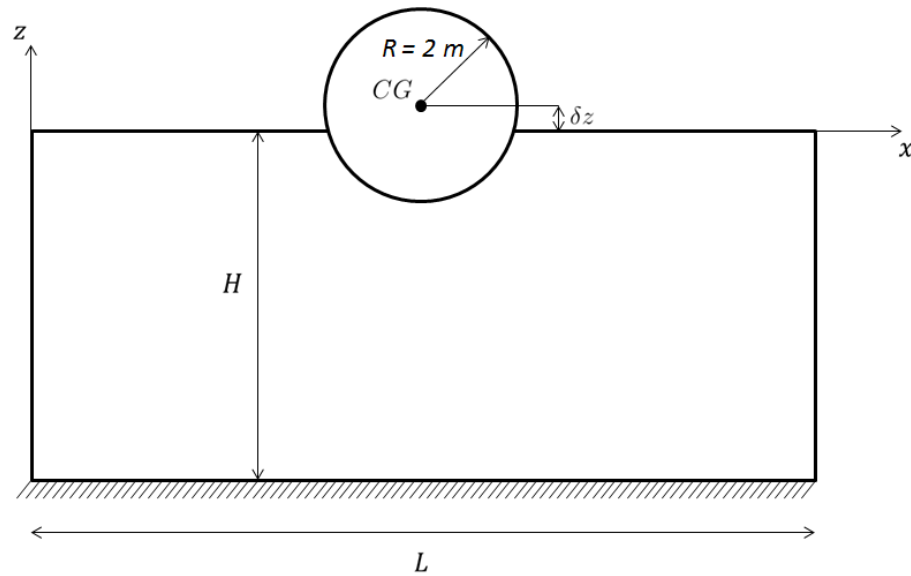
Figure 5.37: Circular section heave decay test

The simulation setup is shown in Table (5.28) and in order to keep the comparison as fair as possible, the same tank dimensions of van Daalen (1993) were adopted. The panel size was arbitrary chosen as 0.1m at all domain, since the domain dimensions were small compared to the ones adopted for the forced oscillation test (described previously), allowing the mesh generation without stretching.

Figure 5.38: Example of cylinder section heave decay test

Table 5.28: Simulation setup for heave decay test of the circular cylinder

Description	Value	Unit
Tank length	40	m
Tank depth	10	m
Time-step	0.05	s
Simulation time	15	s
Panel size (constant)	0.1	m
Initial displacement (δz)	0.05	m
Beach coefficient a	1	-
Beach length b	1	-

The comparison with van Daalen [1993] simulation are presented in Figure (5.39), with the time series reduced in order to better visualize the comparison (he presented onyl the first 10s), where the z coordinate is made non-dimensional by the initial displacement ($z_G(0) = \delta z$). The agreement of both curves are good for the first two cycles. After that, small differences appear, however, the results for the present numerical method were considered consistent, since for the last cycle the z coordinate still cross the zero, as should be expected, which does not happen in van Daalen [1993] simulation. It should be remarked that the absolute values for z coordinates on the last cycle are very small, which makes the accuracy hard to be guaranteed. Since the results of van Daalen (1993) were taken from his thesis, there may also be some small deviations from the original curve. Figure (5.38) shows that after 5 cycles, the body is already almost at rest.
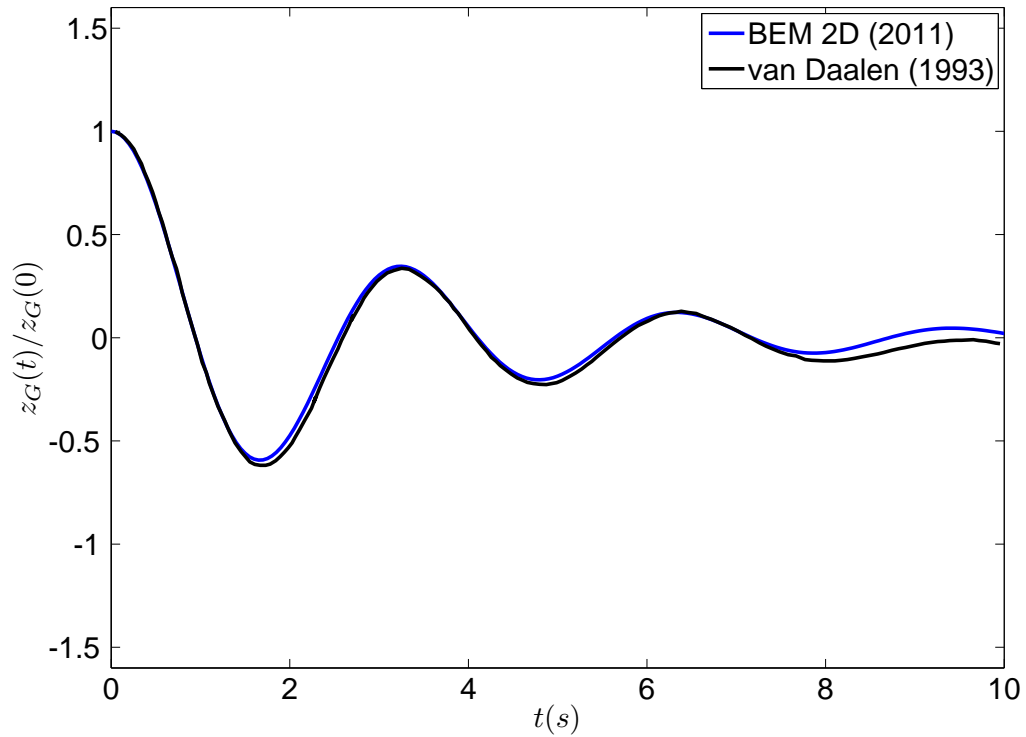
Figure 5.39: Comparison of heave temporal series for the decay test of a circular cylinder

5.3.2 Rectangular cylinder

The same type of comparison was done for a rectangular cylinder with a 4m width and draft of 1m. In addition, the roll decay test was performed in this case. The results are compared to the ones presented by van Daalen [1993]. Actually, it is not exactly a rectangular section since the corners were rounded by circles of 0.25m in order to avoid singularities at the sharp edges and keep the potential flow hypothesis as well as possible, this reported by van Daalen [1993].

An illustration of the test can be seen in Figure (5.40) and the tank used was the same of the circular cylinder. The simulation setup can be seen in Table (5.29). The mesh was kept non-stretched with a constant panel size of 0.1m.
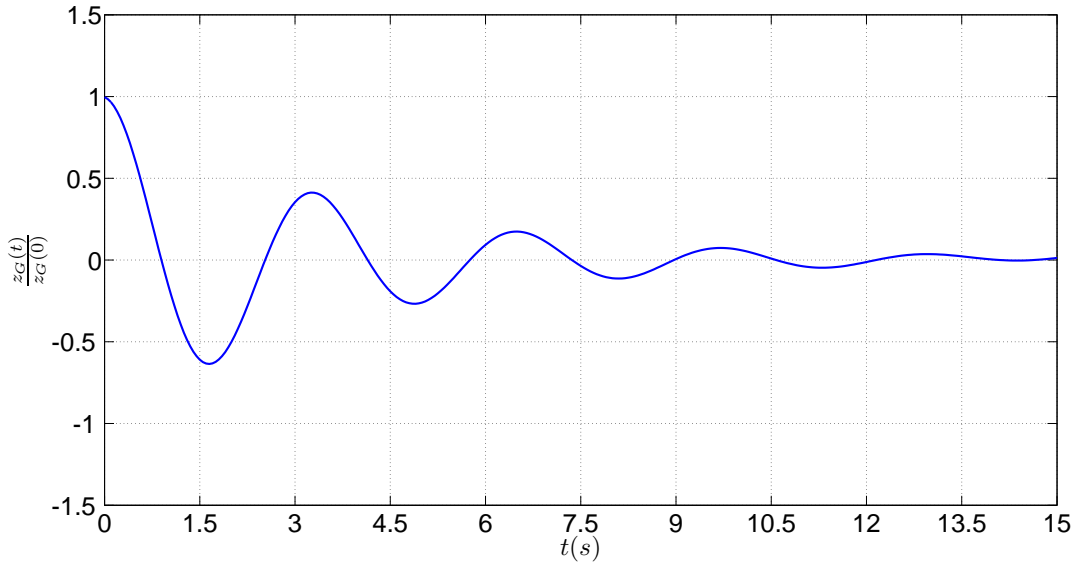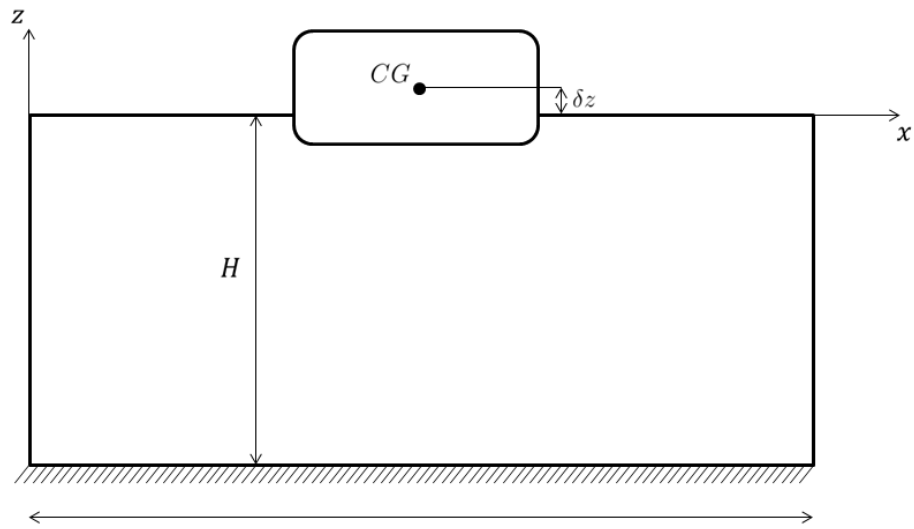
Figure 5.40: Rectangular section heave decay test

Table 5.29: Simulation setup for heave decay test of the rectangular cylinder

Description	Value	Unit
Tank length	40	m
Tank depth	10	m
Time-step	0.05	s
Simulation time	15	s
Panel size (constant)	0.1	m
Initial displacement (δz)	0.25	m
Beach coefficient a	1	-
Beach length b	1	-

The results of this simulation is shown in Figure (5.41) and in this case the agreement is very good along the whole simulation time compared (van Daalen [1993] presented only 10s), even for the small amplitudes, observed at the last cycles of the simulation.
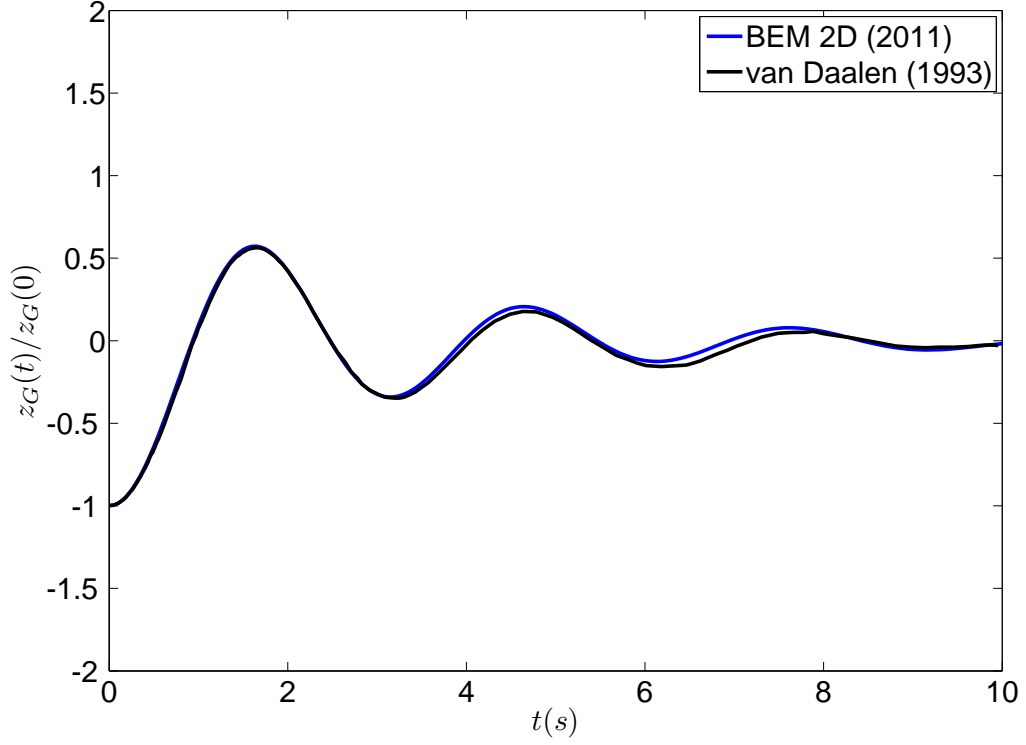
Figure 5.41: Comparison of heave temporal series for the decay test of a rectangular cylinder

The next simulation performed was the same section with rounded corners on roll decay test (single degree of freedom), as can be seen in Figure (5.42), being the initial displacement a small $\delta\theta$. For this simulation, the moment of inertia need to be provided, since it cannot be evaluated directly following the methodology presented in appendix A. The moment of inertia per length can be evaluated by (5.28), where R is the radius concerning the rounded corner and H is the box height (assumed as twice the draft), assuming an homogeneous mass distribution.

$$
I_G = \rho\Big\{ \frac{H(B-2R)}{12}[H^2 + (B-2R)^2] + \frac{R(H-2R)[R^2 + (H-2R)^2]}{6} + 2R(H-2R)\Big(\frac{B-R}{2}\Big)^2
$$
$$
+ \frac{\pi R^4}{4} + \pi R^2\Big[\Big(\frac{B}{2} - R\Big)^2 + \Big(\frac{H}{2} - R\Big)^2\Big]\Big\} \quad (5.28)
$$
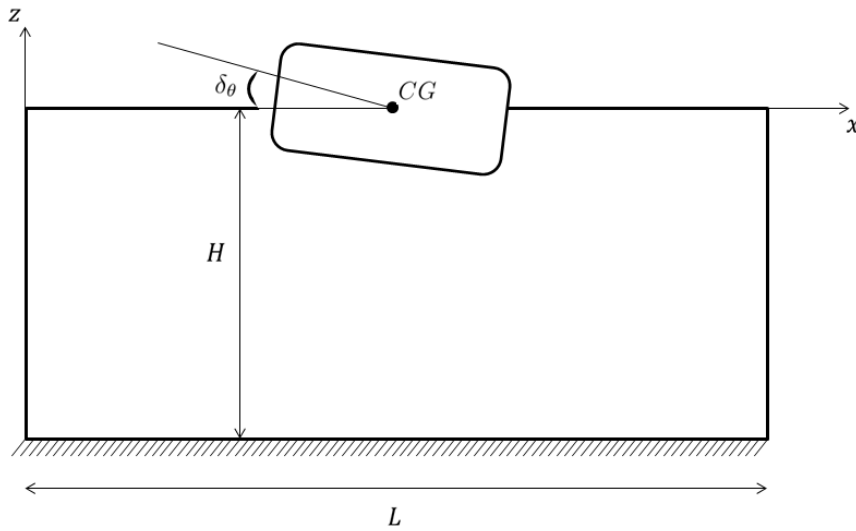
Figure 5.42: Rectangular section roll decay test

The simulation setup can be seen in Table (5.30) and the results are presented in Figure (5.43), compared with van Daalen [1993] numerical results. He states that, although there is some non-linear behavior concerning the roll degree of freedom, observed because the roll period slightly decreased when the initial roll angle is increased, the effect was small. The comparison of linear method here presented and his nonlinear computations shows that in the first cycle the agreement is very good, but there is differences concerning the next cycles. During the simulation, the linear method provided a constant frequency of 1.795 rad/s, while the non-linear computations of van Daalen [1993] provided a time varying frequency, although there was only a few cycles to confirm this conclusion and some inaccuracy due to the scanning process of the results. Maybe those differences were due to non-linear effects, but the agreement still good enough for engineering purposes, specially because the viscous effects were not considered and are very appreciable for this condition.

Table 5.30: Simulation setup for roll decay test of the rectangular cylinder

Description	Value	Unit
Tank length	40	m
Tank depth	10	m
Time-step	0.05	s
Simulation time	15	s
Panel size (constant)	0.1	m
Initial displacement ($\delta\theta$)	0.05	rad
Beach coefficient a	1	-
Beach length b	1	-
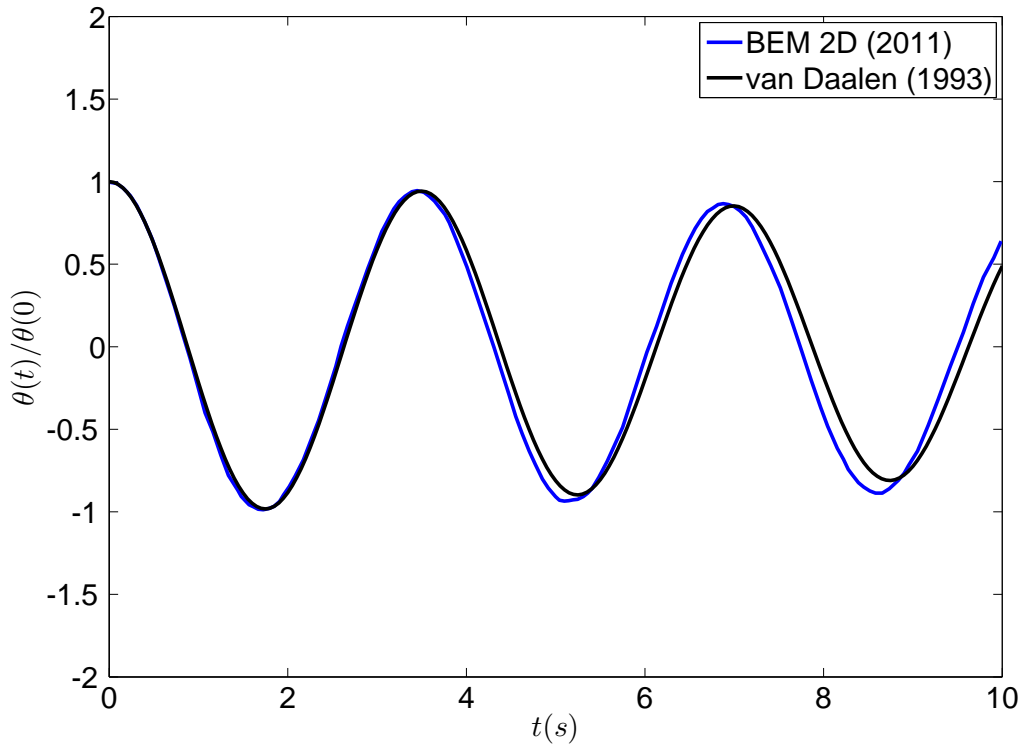
Figure 5.43: Comparison of roll temporal series for the decay test of a rectangular cylinder

5.4 Response Amplitude Operator

In the simulations concerning the decay tests, it was verified that the acceleration potential could provide a stable numerical scheme, verified through the comparisons with other numerical method. The last analysis regards the response amplitude operator of a floating rectangular cylinder, as shown in Figure (5.44), in order to confirm the acceleration potential capability and the correct implementation of the analytic incident wave potential. The results are compared with the numerical ones of Tanizawa et al. [1999], who used a fully non-linear boundary elements method in time domain, and an analytic solution built using the excitation force and radiation potential obtained by applying the methodology proposed by Zheng et al. [2004], already mentioned for the radiation problem, taking the first 40 terms of the series. All the simulations were performed using numerical beaches in order to avoid wave reflection. It is important to emphasize that the present method used an analytic incident potential (as shown in Chapter 2) in order to evaluate the implementation. Tanizawa et al. [1999] used a numerical wave tank (NWT), therefore the wave was generated by a wave-maker.

The results taken from Tanizawa et al. [1999] were for the smaller incident waves and there
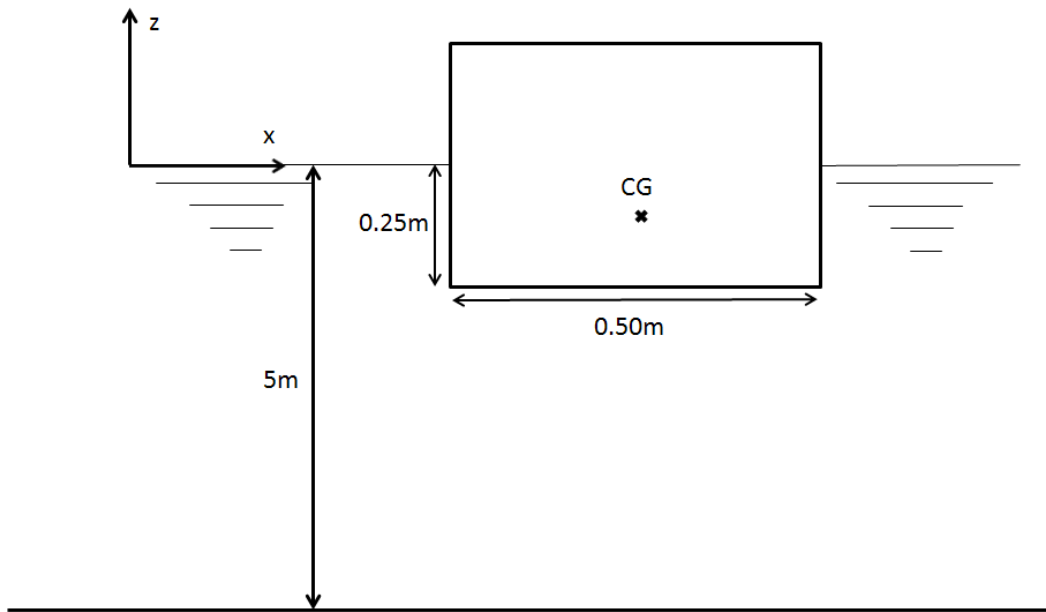
Figure 5.44: Rectangular section for floating body simulation

may be some imprecisions since the results were taken directly from the graphs. The analytic solution used for the response amplitude operator (RAO) was done considering the same depth of the numerical computation in order to keep consistency. The depth is more than one wave-length for all waves, but for the longest one, where it is ≈80%, so no bottom effects are expected.

The simulation setup can be seen in Table (5.31) and an example of the motion series can be seen in Figure (5.4), which shows the signal periodicity and numerical beach effectiveness, since no wave reflection was visually verified. The beach coefficients were kept fixed as one (both a and b) during all simulations. The mesh was arbitrary chosen with a constant panel size of 0.05m in the body, in order to have an integer number of panels, and 0.10m in the free surface and bottom.

Table 5.31: Simulation setup for rectangular section RAO calculation

Description	Value	Unit
Tank length	50	m
Tank depth	5	m
Time-step	0.05	s
Simulation time	100	s
Panel size at the body (constant)	0.05	m
Panel size at the free surface and bottom (constant)	0.10	m
Body mass per length	125	kg/m
Moment of inertia	5.208	kg.m
KG	0.135	m
Beach coefficient "a"	1	-
Beach length "b"	1	-
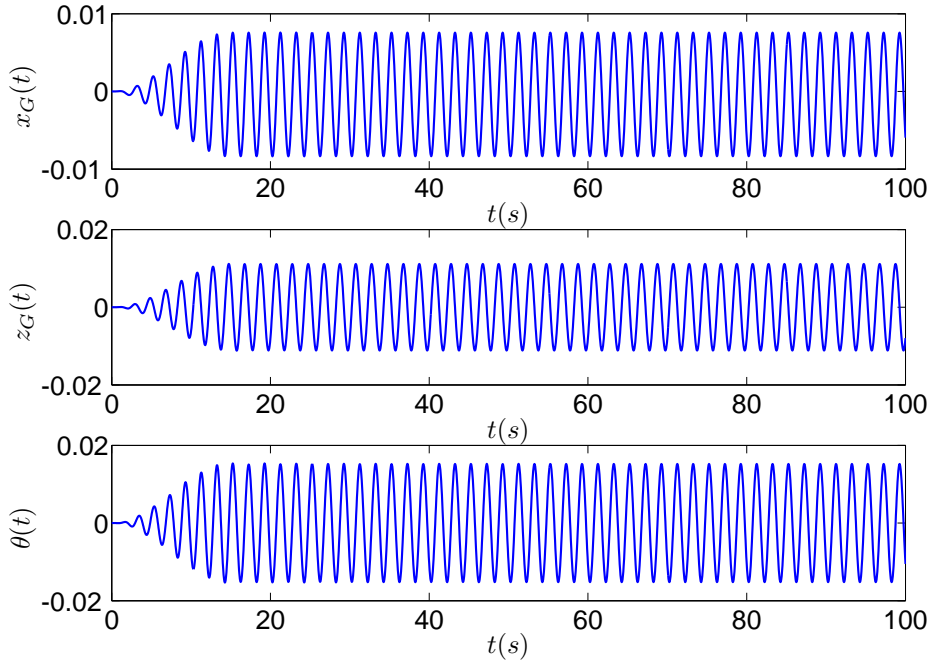
Figure 5.45: Motion series example for the rectangular section free floating

The regular waves tested are given in Table (5.32), together with the dimensionless factor $\xi = \dfrac{\omega^2 B}{2g}$ used on Tanizawa's results. The heave response operator is given in Figure (5.46), where it can be seen that the numerical results had a good agreement with the analytic solution, with small differences from the results of Tanizawa. Apparently in his results the heave peak is a little bit further in frequency and with a smaller amplification factor, which could be due to the fully non-linear approach, since the linear value is more than 2, which could generate a considerable variations in the body submerged surface. Besides that, near resonance regions the non-linear approach is difficult, specially considering higher wave amplitude, as was verified by

him in the lack of convergence for some simulations. During the simulations, the three degrees of freedom were free to oscillate.

Table 5.32: Regular waves used for RAO calculation

ξ	$\omega(rad/s)$	$\lambda(m)$
0.25	3.13	6.28
0.50	4.43	3.14
0.55	4.65	2.86
0.60	4.85	2.62
0.65	5.05	2.42
0.70	5.24	2.24
0.75	5.42	2.09
1.00	6.26	1.57
1.25	7.00	1.26
1.50	7.67	1.05
1.75	8.29	0.90
2.00	8.86	0.79

The results for sway and roll can be seen in Figures (5.47) and (5.48), respectively, and the agreement of all results are good, with the time domain simulation being capable of correctly predicting the cancelation point on the sway response operator without any kind of additional modelling, as was needed for the analytic solution due to the added mass and potential damping cross terms, which generate the hydrodynamic coupling between these degrees of freedom. It means that the presented numerical method, considering an unique disturbance potential, can evaluate the hydrodynamic field entirely.
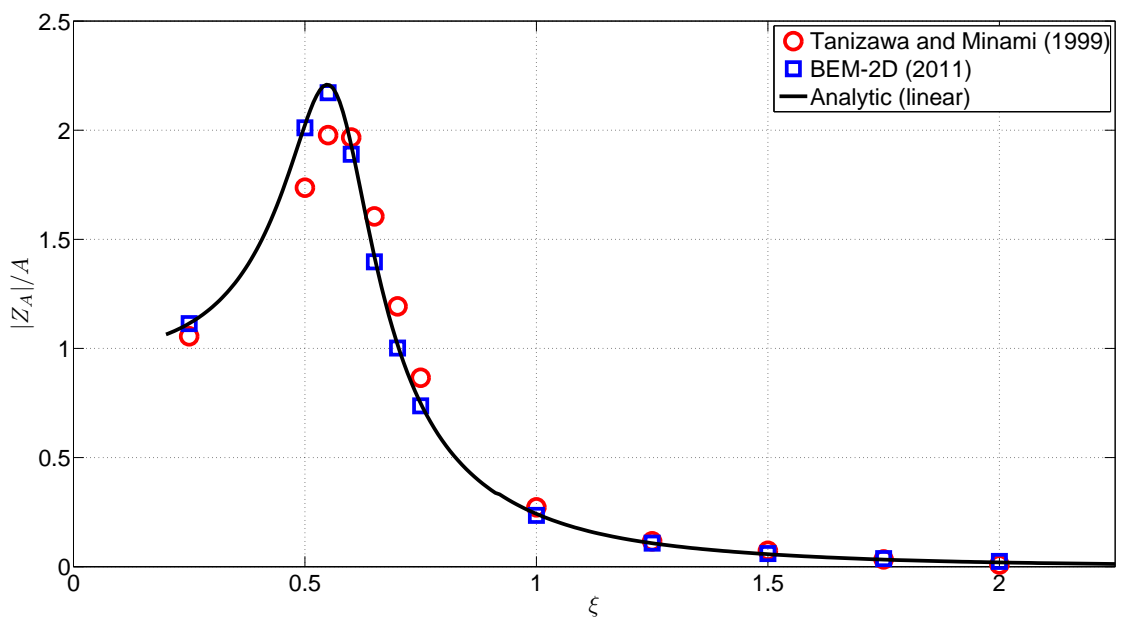

Figure 5.46: Comparison of heave response operator for a rectangular section
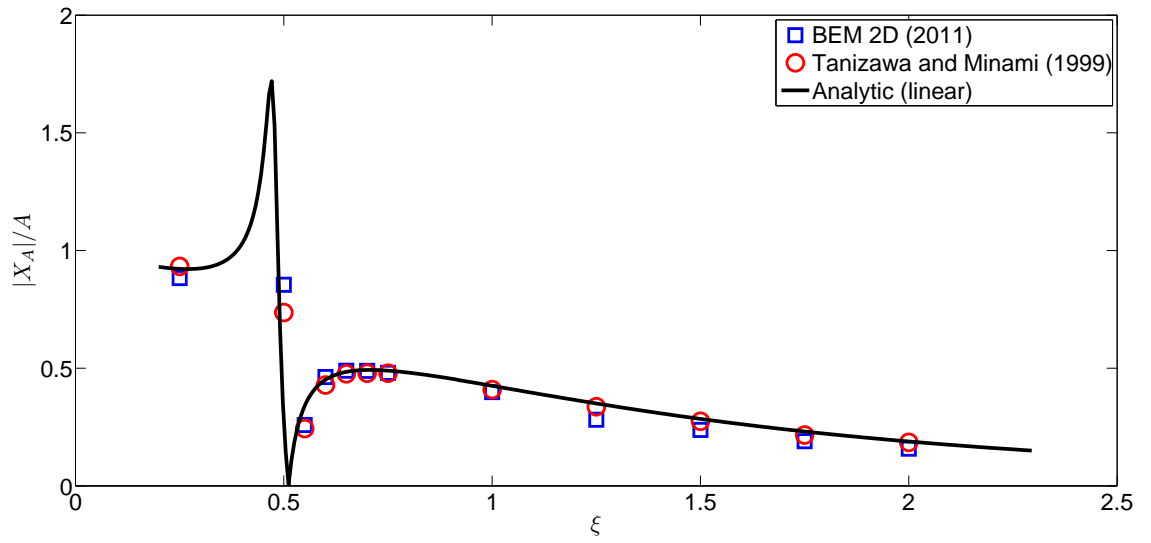
118

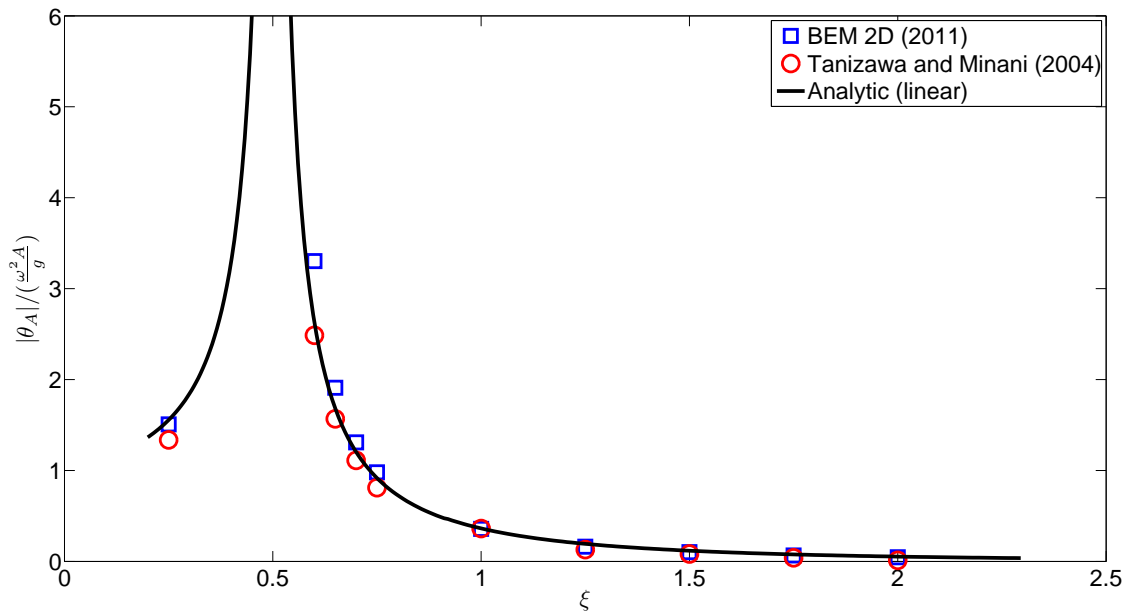Figure 5.47: Comparison of sway response operator for a rectangular section

Figure 5.48: Comparison of roll response operator for a rectangular section

Chapter 6

Conclusion and final remarks

In this work a time domain low order panel method was developed using Rankine sources for the prediction of hydrodynamic forces and motions of 2D floating structures. Two integral equations were obtained for solving the more generic case containing floating bodies and bodies with prescribed motion, being possible to reproduce both an experimental test at a wave basin or an ocean condition in a simplified way, since it is a 2D method.

A linear approach was adopted, which means that the geometry is fixed during the simulations since the boundary conditions are linearized and imposed at the mean surfaces. The numerical scheme uses the collocation method for solving the integral equation with one collocation point placed on the center of the linear panels. The free surface differential equations and body motion equations were evaluated using the Runge-Kutta 4th order method, which provided an accurate and stable numerical method, although required some evaluations of the functions per time-step, that is time consuming. A possible next step would be a more focused study on the stability conditions and time-step size in order to reduce the computational effort by using an adaptative time-stepping procedure.

The integration processes were performed numerically to develop a flexible numerical scheme that could be latter extended for a higher order method, when no analytical solutions are available for the potential distribution inside the panels.

In order to avoid the presence of reflected waves, a numerical beach were also implemented and applied in the simulations, showing good effectiveness despite the small numerical effort that it requires. The method chosen was based on damping the waves through a sponge condition, as first presented by Israeli and Orszag [1981].

The numerical results for the cases tested were in good agreement with analytic, numerical

and/or experimental results. The first application studied was a classical wave-maker problem and the numerical scheme was able to correctly predict the transfer function of piston and flap type wave-makers.

The numerical tool was also used to evaluate the added mass and potential damping of bidimensional circular and rectangular cylinders, obtaining good agreement with the results available on the literature, including the experimental results of Vugts [1968].

Decay tests were also performed in the context of a wave tank and the results showed good agreement with the ones of van Daalen [1993], even for rolling simulations.

The last result presented was the response amplitude operator (RAO) evaluation for a rectangular cylinder. The results were compared to an analytic solution and the fully non linear numerical results of Tanizawa et al. [1999]. Once again a good agreement could be obtained.

Future works could be done in order to improve the tool for three-dimensional cases, still in linear context. After that, the extension for non-linear simulations and multi-bodies could be performed and validated in order to improve the numerical code. Other applications, such as the integration with mooring line codes or structural ones would probably also lead to very interesting results. These last goals would be a long term development for the Numerical Offshore Tank (TPN) in order to attach a time domain boundary elements method for seakeeping prediction (single and multi-bodies) to a mooring finite element method (FEM) software, in order to solve the coupled dynamic of a floating body in time domain, which could be latter extended to fully non-linear analysis.

Bibliography

Ang, W.-T. (2007). *A beginner's course in Boundary Elements Methods*. Universal Publishers.

Barber, N. F. and Ursell, F. (1948). The generation and propagation of ocean waves and swell: I - wave periods and velocities. *Transaction of the Royals Society of London*, pages 527–560.

Batchelor, G. K. (2009). *An Introduction to Fluid Dynamics*. Cambridge Mathematical Library.

Benjamin, T. B. and Feir, J. E. (1967). The desintegration of wavetrains in deep water. part 1. *Journal of Fluid Mechanics*.

Bertram, V. (1996). Rankine source methods for seakeeping problems. *Transaction of STG (Schifsbauz Technusche Gesellschaft)*.

Black, J. L., Mei, C. C., and Bray, M. C. G. (1971). Radiation and scattering of water waves by rigid bodies. *Journal of Fluid Mechanics*, 46:151–164.

Cao, Y., Beck, R., and Schultz, W. (1994). Nonlinear motions of floating bodies in incident waves. *9th Workshop on Water Waves and Floating Bodies*.

Cao, Y., Beck, R. F., and Schultz, W. W. (1993). An absorbing beach for numerical simulations of nonlinear waves in wave tank.

Clement, A. (1996). Coupling of two absorbing boundary conditions for 2d time-domain simulations of free surface gravity waves. *Journal of Computational Physics*, 126:139–151.

Contento, G. (2000). Numerical wave tank computations of nonlinear motions of two-dimensional arbitrary shaped free floating bodies. *Ocean Engineering*, 27:531–556.

Cummins, W. E. (1962). The impulse response function and ship motions. Technical Report 1661, David Taylor Model Basin.

Dawson, C. W. (1977). A practical computer method for solving ship-wave problems. In *Procedure of the Second International Conference on Numerical Ship Hydrodynamics*, pages 30–38.

Dean, R. G. and Dalrymple, R. A. (2000). *Water Wave Mechanics for Engineers and Scientists*, volume 2 of *Advanced Series on Ocean Engineering*. World Scientific.

Dean, R. G., Ursell, F., and Yu, Y. S. (1959). Forced small-amplitude water waves: comparison of theory and experiment. *Journal of Fluid Mechanics*, pages 33–52.

Engquist, B. and Majda, A. (1977). Absorbing boundary conditions for numerical simulation of waves. *Applied Mathematical Sciences*, 74(5):1765–1766.

Faltinsen, O. M. (1990). *Sea Loads on Ships and Offshore Structures*. Cambridge University Press.

Fox, R. W. and Donald, A. T. (1973). *Introdução à Mecânica dos Fluidos*. John Wiley Sons.

Gao, Z. and Zou, Z. (2008). A nurbs-based high-order panel method for three-dimensional radiation and diffraction problems with forward speed. *Ocean Engineering*, 35:1271–1282.

Greco, M. (2001). *A two-dimensional Study of Green-Water Loading*. PhD thesis, NTNU - Norwegian University of Science and Technology.

Havelock, T. H. (1963). Forced surface-waves on water. In *The Collected Papers of Sir Thomas Havelock on Hydrodynamics*. C. Wigley.

Hermans, A. J. (2011). *Water Waves and Ship Hydrodynamics*. Springerlink, second edition.

Hess, J. L. and Smith, A. M. O. (1964). Calculation of nonlifting potential flow about arbitrary three-dimensional bodies. *Journal of Ship Research*, pages 22–44.

Huang, Y. (1997). *Nonlinear Ship Motions by a Rankine Panel Method*. PhD thesis, Massachussets Institute of Technology.

Israeli, M. and Orszag, S. A. (1981). Approximation of radiation boundary conditions. *Journal of Computational Physics*.

John, F. (1949). On the motion of floating bodies i. *Pure Applied Mathematics*, pages 13–57.

John, F. (1950). On the motion of floating bodies ii. *Pure and Applied Mathematics*, pages 45–101.

Kacham, B. (2004). Inviscid and viscous 2d unsteady flow solvers applied to fpso hull roll motions. Technical report, The University of Texas.

Kim, M. H. and Koo, W. C. (2005). *Numerical Models in Fluid-Strucutre Interaction*, chapter 2D Fully nonlinear wave tanks, pages 43–81. WIT Press.

Kim, Y. (2003). Artificial damping in water wave problems ii: Application to wave absorption. *International Journal of Offshore and Polar Engineering*, 13(2).

Kim, Y., Kring, D. C., and Sclavounos, P. D. (1997). Linear and nonlinear interactions of surface waves with bodies by a three-dimensional rankine panel method. *Applied Ocean Research*, 19:235–249.

Koo, W. (2003). *Fully Nonlinear Wave-Body Interactions by a 2D Potential Numerical Wave Tank*. PhD thesis, Texas AM University.

Koo, W. and Kim, M.-H. (2004). Freely floating-body simulation by a 2d fully nonlinear numerical wave tank. *Ocean Engineering*, 31:2011–2046.

Kring, D. C. (1994). *Time Domain Ship Motions by a Three-Dimensional Rankine Panel Method*. PhD thesis, Massachussets Institute of Technology.

Kumar, S. and Narayan, J. P. (2008). Absorbing boundary conditions in a forth-order accurate sh-wave staggered grid finite difference algorithm. *Acta Geophysica*, 56(4):1090–1108.

Kuznetsov, N., Maz'ya, V., and Vainberg, B. (2004). *Linear Water Waves - A Mathematical Approach*. Cambridge University Press.

Lamb, H. (1945). *Hydrodynamics*. Dover Publishing Inc.

Lee, C.-H. and Newman, J. N. (2005). *Numerical Models in Fluid-Structure Interaction*, chapter Computation of wave effects using the panel method, pages 211–251. WIT Press.

Lin, W. M. (1984). *Nonlinear motion of free surface near a moving body*. PhD thesis, Massachussets Institute of Technology - MIT.

Maniar, H. D. (1995). *A thrre dimensional higher order panel method based on B-splines*. PhD thesis, MIT - Massachusset Institute of Technology.

Maruo, H. (1960). The drift of a body floating on waves. *Journal of Ship Research*, pages 1–10.

Mei, C. C., Stiassnie, M., and Yue, D. K.-P. (2005). *Theory and Applications of Ocean Surface Waves. Part 1: Linear aspects.* World Scientific Publishing Co.

Milne-Thomson, L. M. (1968). *Theoretical Hydrodynamics.* Dover Publications Inc.

Moiseiwitsch, B. L. (2005). *Integral Equations.* Dover Publications Inc.

Nakos, D. E., Kring, D. C., and Sclavounos, P. D. (1993). Rankine panel methods for transient free surface flows. *6th International Conference on Numerical Ship Hydrodynamics.*

Nayfeh, A. H. (1973). *Perturbation Methods.* John Wiley Sons Inc,.

Newman, J. N. (1977). *Marine Engineering.* The MIT Press.

Pesce, C. P. (1988). *Estudo do Comportamento de Corpos Flutuantes em Ondas sob um Enfoque Variacional (in Portuguese).* PhD thesis, Universidade de São Paulo.

Pinkster, J. A. (1980). *Low frequency Second Order Wave Exciting Forces on Floating Structures.* PhD thesis, Delft University of Technology.

Prins, H. (1995). *Time-Domain Calculations of Drift Forces and Moments.* PhD thesis.

Qiu, W. (2001). *A panel-free method for time-domain analysis of floating bodies in waves.* PhD thesis, Dalhousie University.

Qiu, W., Peng, H., and Chuang, J. M. (2006). Computation of wave-body interactions using the panel-free method and exact geometry. *Jounal of Offshore Mechanics and Arctic Engineering.*

Queiroz Filho, A. d. N. and Tannuri, E. A. (2009). Dp offloading operation: A numerical evaluation of wave shielding effect. *Manoeuvring and Control of Marine Craft.*

Rahman, M. (2007). *Integral Equations and their Applications.* WIT Press.

Shao, Y.-L. (2010). *Numerical Potential-Flow Studies on Weakly-Nonlinear Wave-Body Interactions with/without Small Forward Speeds.* PhD thesis, NTNU - Norwegian University of Science and Technology.

Sommerfeld, A. (1949). *Partial Differential Equations in Physics.* Academic Press.

Stassen, Y., Le Boulluec, M., and Molin, B. (1998). High order boundary element model for 2d wave tank simulation. *International Offshore Polar Engineering Conference 3*, pages 348–355.

Stoker, J. J. (1957). *Water Waves - The Mathematical Theory with Applications*. Interscience Publisher.

Stokes, G. (1847). *On the theory of oscillatory waves.* Mathematical and Physical Papers - Reprinted from the Original Journals and Transactions.

Tanizawa, K. (1995). A nonlinear simulation method of 3-d body motions in waves. *Journal of the Society of Naval Architects of Japan.*

Tanizawa, K. (2000). The state of the art on numerical wave tank. In *Proceeding of 4th Osaka Coloquium on Seakeeping Performance of Ships*, pages 99–114.

Tanizawa, K., Minami, M., and Naito, S. (1999). Estimation of wave drift force by a numerical wave tank. *9th International Offshore and Polar Engineering Conference.*

Tanizawa, K., Minami, M., and Sawada, H. (2000). Estimation of wave drift force by a numerical wave tank, 2nd report. *10th International Offshore and Polar Engineering Conference.*

Tanizawa, K. and Naito, S. (1997). A study of parametric roll motions by a fully nonlinear numerical wave tank. *7th International Offshore and Polar Engineering.*

Tanizawa, K. and Naito, S. (1998). An application of fully nonlinear numerical wave tank to the study on chaotic roll motions. *8th International Offshore and Polar Engineering Conference.*

Tannuri, E. A., Bravin, T. T., and Simos, A. N. (2004). Dynamic simulation of offloading operation considering wave interaction between vessels. *23rd International Conference on Offshore Mechanics and Arctic Engineering*, pages 245–250.

Tricomi, F. G. (1985). *Integral Equations*. Dover Publications Inc.

van Daalen, E. F. G. (1993). *Numerical and Theoretical Studies of Water Waves and Floating Bodies.* PhD thesis, University of Twente.

Vugts, J. H. (1968). The hydrodynamic coefficients for swaying, heaving and rolling cylinders in a free surface. *International Shipbuilding Progress*, pages 251–275.

Yang, J. (2004). *Time Domain Nonlinear Theories of Ship Motions*. PhD thesis, University of Hawaii.

Yee-Tak Ng, J. (1993). *Time-domain second-order wace interactions with floating offshore structures*. PhD thesis, The University of British Columbia.

Zhen, L., Bin, T., De-zhi, N., and Ying, G. (2010). Wave-current interactions with three dimensional floating bodies. *Journal of Hydrodynamics*, pages 229–240.

Zheng, Y. H., You, Y. G., and Shen, Y. M. (2004). On the radiation and diffraction of water waves by a rectangular buoy. *Ocean Engineering*, 31:1063–1082.

Zhu, X. (1997). *A Higher-Order Panel Method for Third-Harmonic Diffraction Problems*. PhD thesis, MIT - Massachussets Institute of Technology.

Part I

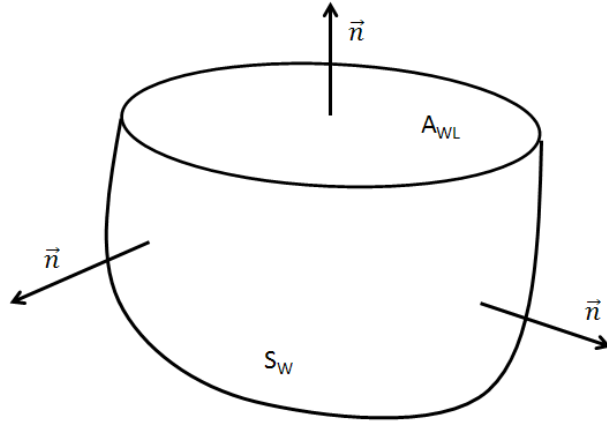# Numerical calculation of volume and water plane area

Figure 6.1: Gauss theorem orientation

The volume and water plane area are needed for free floating simulations and so a numerical automatic method for their calculation are required in order to makes the numerical method generic. The volume calculation by the definition (6.1) can be changed for (6.2) using Gauss theorem and considering an arbitrary vector field with unitary divergent. The volume is then a simple calculation using the boundaries, which are exactly the entrances for a panel method. Some simple fields are $\vec{F}_1 = x\vec{i}$, $\vec{F}_2 = y\vec{j}$ or $\vec{F}_3 = z\vec{k}$ and any can be used for the calculations.

$$V = \int_V dV \tag{6.1}$$

$$\int_V \nabla \cdot \vec{F} dV = \oiint_{\partial V} \vec{F} \cdot \vec{n} d\partial V \tag{6.2}$$

For the bidimensional case the volume (actually the volume per length) is evaluated by the expression (6.3), considering the field $x\vec{i}$, where n_{xj} is the x component of the normal vector (which is constant for the low order approximation), x_{cj} is the x coordinate of the centroid and l_j is the panel length. An analogous expression would be found for the fields $y\vec{j}$ or $z\vec{k}$.

$$V = \oiint_{\partial V} \vec{F} \cdot \vec{n} d\partial V \approx - \sum_{j \in Body} \int_{P_j} x n_{xj} dl_j = - \sum_{j \in Body} n_{xj} \int_{P_j} x dl_j = - \sum_{j \in Body} n_{xj} x_{cj} l_j \tag{6.3}$$

The water plane area can be evaluated using Stokes theorem (6.4) and the identity (6.5) is verified. The next step is to find any vector field, which the curl has z component equals to

unity, so the calculations on (6.6) can be performed.

$$\int_S (\nabla \times \vec{F}) \cdot \vec{n} dS = \oint_{\partial S} \vec{F} \cdot d\vec{s} \qquad (6.4)$$

$$\int_{S_{Waterplane}} (\nabla \times \vec{F}) \cdot \vec{k} dS = \int_{S_{Wetted}} (\nabla \times \vec{F}) \cdot \vec{n} dS \qquad (6.5)$$

$$\nabla \times \vec{F} = \alpha \vec{i} + \beta \vec{j} + 1\vec{k} \Rightarrow \int_{S_{Waterplane}} (\nabla \times \vec{F}) \cdot \vec{k} dS = \int_{S_{Waterplane}} dS = A_{WL} \qquad (6.6)$$

An example of vector field that satisfies this condition is $\vec{F} = x\vec{j}$, which reduces the water plane area calculation to the simple calculation (6.7). For the bidimensional case the results is analogous.

$$A_{WL} = \int_{S_{Wetted}} (\nabla \times \vec{F}) \cdot \vec{n} dS = \int_{S_{Wetted}} n_z dS \approx \sum_{j \in Body} \int_{P_j} n_z dS = \sum_{j \in Body} n_{zj} \int_{P_j} dS =$$

$$\sum_{j \in Body} n_{zj} A_j \qquad (6.7)$$